LBL-10616

Lawrence Berkeley Laboratory

UNIVERSITY OF CALIFORNIA

Accelerator & Fusion Research Division

NEGATIVE ION PRODUCTION BY BACKSCATTERING FROM ALKALI-METAL SURFACES BOMBARDED BY IONS OF HYDROGEN AND DEUTERIUM

Peter Juergen Schneider
(Ph.D. thesis)

MASTER

March 1980

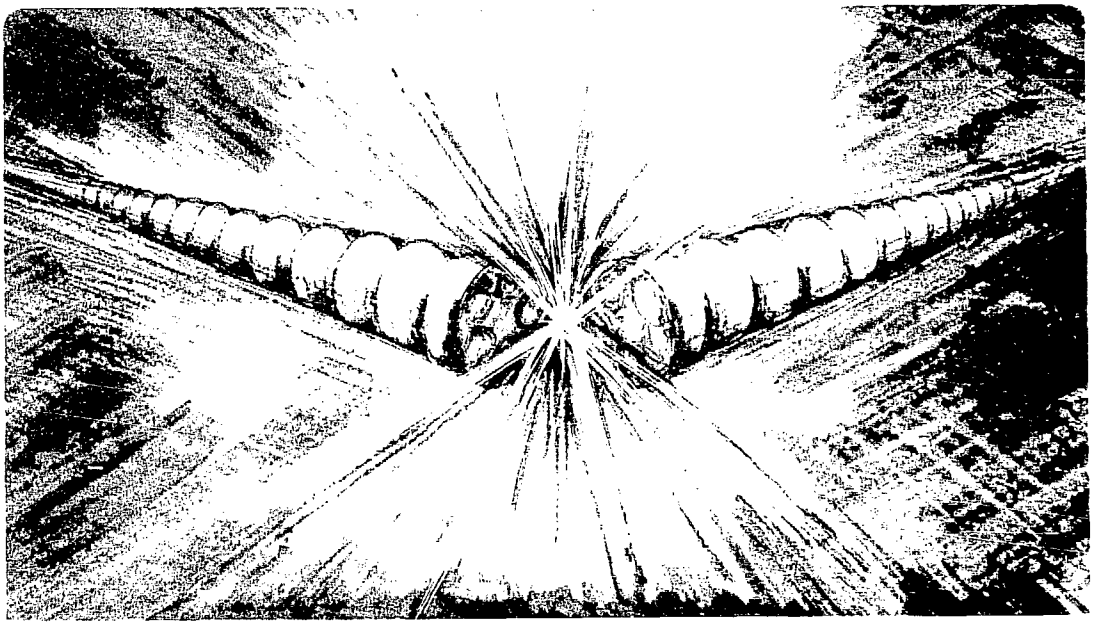

Prepared for the U.S. Department of Energy under Contract W-7405-ENG-48

DISTRIBUTION OF THIS DOCUMENT IS UNLIMITED

NEGATIVE ION PRODUCTION BY BACKSCATTERING FROM ALKALI-METAL SURFACES BOMBARDED BY IONS OF HYDROGEN AND DEUTERIUM

Peter Juergen Schneider

(Ph.D. Thesis)

Lawrence Berkeley Laboratory
University of California
Berkeley, California 94720

March 1980

ABSTRACT

A high current density source of D^- is desirable for making high energy neutral beams for injection into fusion plasmas. One promising approach involves H^- and D^- production on surfaces bombarded by ions and neutrals with energies of a few hundred electron Volts. In an effort to gain insight useful for the further development of such a source, the present experiment was undertaken to investigate the mechanism of surface production of H^- and D^-. Measurements have been made of the total backscattered D^- and H^- yields from thick, clean targets of Cs, Rb, K, Na and Li, bombarded with H_2^+, H_3^+, D_2^+ and D_3^+ with incident energies from 0.15-to-4.0 keV/nucleus. All of the measurements were made at background pressures less than 10^{-9} Torr and the alkali-metal targets were evaporated onto a cold substrate (T=77K) in situ to assure thick, uncontaminated targets. For each target, the H^- and D^- yields exhibited a maximum (as high as 8 percent per incident proton or deuteron) at incident energies between 0.3 and 1.4 keV/nucleus. For hydrogen (deuterium) incident at any

DISCLAIMER

This book was prepared as an account of work sponsored by an agency of the United States Government. Neither the United States Government nor any agency thereof, nor any of their employees, makes any warranty, express or implied, or assumes any legal liability or responsibility for the accuracy, completeness, or usefulness of any information, apparatus, product, or process disclosed, or represents that its use would not infringe privately owned rights. Reference herein to any specific commercial product, process, or service by trade name, trademark, manufacturer, or otherwise, does not necessarily constitute or imply its endorsement, recommendation, or favoring by the United States Government or any agency thereof. The views and opinions of authors expressed herein do not necessarily state or reflect those of the United States Government or any agency thereof.

DISTRIBUTION OF THIS DOCUMENT IS UNLIMITED

energy, the H^- (D^-) yield decreases in going from Cs to Li in the order given above. Also, a definite isotope effect was observed for every target used, withthe H^- yield peaking at a lower incident energy than the D^- yield and in most cases, the maximum H^- yield was higher than the maximum D^- yield.

Measurements of the H^-yield from various transition metal targets with thin coverages of alkali-metals have also been made as a function of the surface work function. The work function exhibited a minimum value as a function of the thickness of the alkali-metal coverage, and the H^- yield exhibited a corresponding maximum. For all of the alkali-metals used, the maximum value of the H^- yield was higher than for the thick targets.

The negative ion yields are discussed in terms of the probabilities of reflection of the incident particles, of formation of the negative ion at the surface and of the survival of the negative ion leaving the surface. For each thick alkali-metal target, the negative ion yield measurements have been used in a least squares fit to determine two parameters in a theoretically derived expression for the negative ion yield. The parameters obtained from a thick Na target have been used to calculate the yield from a Cu target with thin coverage of Na (such that the surface work function is equal to thick Na). The calculated and measured values agree very well.

DEDICATION

To my parents

Ingeborg and Karl

ACKNOWLEDGMENTS

I am indebted to Dr. Robert V. Pyle for his continuous interest and active supervision during the course of this work. I am also indebted to Dr. Klaus Berkner and Dr. William G. Graham for guidance and encouragement through the course of this work, and to Dr. John Hiskes for his efforts in the analysis of the experimental results. Also, John W. Stearns for his assistance in all aspects of the experiment and Charles M. Garrett for maintaining the electronics associated with the experiment. My thanks also go to the members of the mechanical shops of Harlan Hughes and Louis Biagi, who built the mechanical components of the experiment. Finally, I would like to thank Augustine Aitkens and Marnie McElhiney for typing this manuscript.

TABLE OF CONTENTS

		PAGE
Acknowledgment		ii
I.	Introduction	1
II.	Present theories of H^- production from surfaces	11
III.	Experimental approach and apparatus	22
	A. Approach	22
	B. Apparatus	26
	1. Accelerator	26
	2. Magnet and Beamline	28
	3. Experimental chamber	28
IV.	Experimental Measurements	39
	A. Operating parameters	39
	B. Thick targets	48
	C. Thin targets	52
V.	Results and Discussion	55
	A. Thick targets	55
	B. Thin targets	79
	C. Data fitting	90
VI.	Application of Results to Controlled Fusion	100

VIII. Summary and Conclusions 105

Appendices

A. Impurity Analysis 108

B. Work Function Measurements 113

C. Particle Orbit Calculations 118

D. Error Analysis 122

E. Sputtered Negative Ions in the NISEC 124

F. Derivation of the NISEC Fitting Function 127

References 130

CHAPTER I

INTRODUCTION

High energy beams of neutral deuterium atoms are currently being used to heat and fuel thermonuclear fusion plasmas. The neutral particles pass through the magnetic field used to contain the plasma and are ionized by low energy particles already trapped within the field. Presently, beams of deuterons with energies as high as 120 keV are being developed for fusion machines such as TFTR[1] and projections of requirements for full scale fusion power plants call for beam energies as high as 1.2 Mev[2]

The present method of producing high energy neutral beams is: (1) deuterium gas is ionized by electron bombardment to give D^+, D_2^+, D_3^+ (2) these ions are electrostatically accelerated and (3) neutralized by charge exchange in a D_2 gas neutralizer. The efficiency with which high energy charged particles are converted to neutrals is strongly dependent upon the particle energy, as can be seen from Figure 1.[3,4] For positively charged deuterons with energies much greater than 100 keV, the neutralization efficiency becomes low enough to make the present method of high energy neutral beam production unacceptable in terms of the amount of energy which must be recirculated within the neutral beam system.

As can also be seen from Figure 1, the neutralization efficiency for D^- remains fairly high throughout the energy range shown. To take advantage of this high efficiency in a neutral beam system, we could use the same method outlined above by replacing step (1) with: D^- is produced in a high current density source. Unfortunately, a high-

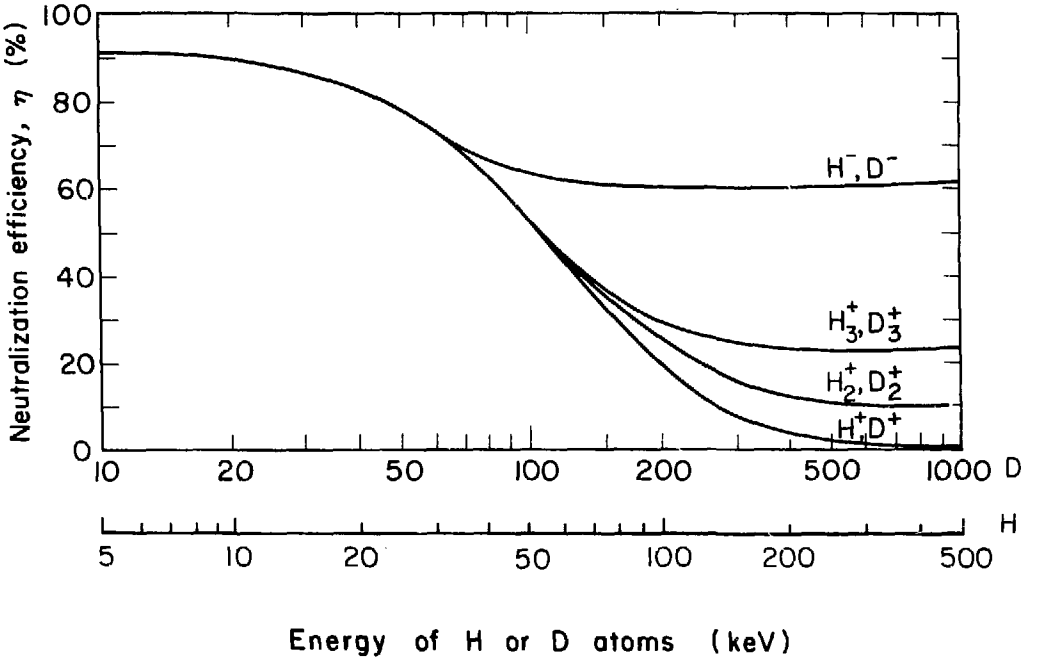

XBL751 -2059A

Figure 1. Maximum neutralization efficiency in D_2 (H_2) vs beam energy for each of the beams: D^+ (H^+), D_2^+ (H_2^+), D_3^+ (H_3^+) and D^- (H^-).

current, high-current-density D^- source does not exist, but there are two approaches to making D^- currently being investigated, either of which may lead to the development of such a source: (1) double charge exchange of positive ions in metal vapors, and (2) direct extraction from a discharge where negative ions are produced by volume or surface processes.

One way to make D^- is by double electron capture by D^+ passing through a suitable vapor or gaseous target. The highest yield reported so far has been a D^- charge fraction of 35 percent for 300 eV D^+ passing through cesium metal vapor.[5] The conversion efficiencies in alkali-metal vapors are high enough to make a D^- source based on double electron capture feasible, and research on such sources is currently underway. However, there are several potential drawbacks associated with using alkali-metal vapors in a neutral beam system:

1. A low-energy, high current-density beam of D^+ must be produced and transported to the charge exchange cell. Transport of such a beam is difficult because space charge effects cause the beam to diverge, giving rise to large beam losses.
2. The alkali metal in the vapor cell cannot be perfectly confined so it will tend to spread throughout the system. It may condense upon insulators and give rise to voltage breakdown problems.
3. The alkali metal may diffuse into the fusion plasma and cool the plasma through bremsstrahlung. Also, it may prevent penetration of the neutral beams into the central part of the plasma by ionizing the neutrals in the fringe field.

A second idea for making a D^- source is by direct extraction--the D^- is produced in a source with a plasma discharge and extracted directly at high energy. Such a source might have better beam optics than charge exchange because the D^- ions are extracted at high energy and the effects of space charge may be greatly reduced. Also, such a source might be more compact and allow better isolation of the neutral beam source from the fusion plasma.

The first direct extraction source to produce significant H^- currents was developed by Ehlers.[6] It was a Penning discharge geometry, with H^- extracted across the magnetic field and gave currents up to 6 mA from a 12.7 mm x 1.5 mm slot (30 mA/cm^2). Although the current was too small, the source had the desirable feature of steady state operation. The Magnetron (see Fig. 2), a direct extraction source based upon surface production, has been developed by Dimov et al.[7,8] The Magnetron is one of a class of sources with a planotron geometry which are high current (> 100 A) pulsed discharges in crossed electric and magnetic fields. When the Magnetron is run on H_2 gas only, it gives currents up to 17 mA (0.22 A/cm^2) and when Cs was added to the discharge currents as high as 0.88A (3.7 A/cm^2) have been reported. Enhancement of the negative ion currents from a planotron has also been observed when other alkali-metals were added to the discharges[9] (see Table 1). The increased current is hypothesized[7-11] to result from alkali-metal coverage of the molybdenum surfaces on the source, which enhances the H^- production at these surfaces (see Chapter II). Dimov et al. have also constructed a modified Magnetron source which operates in a Penning mode.[10] This source has a quieter

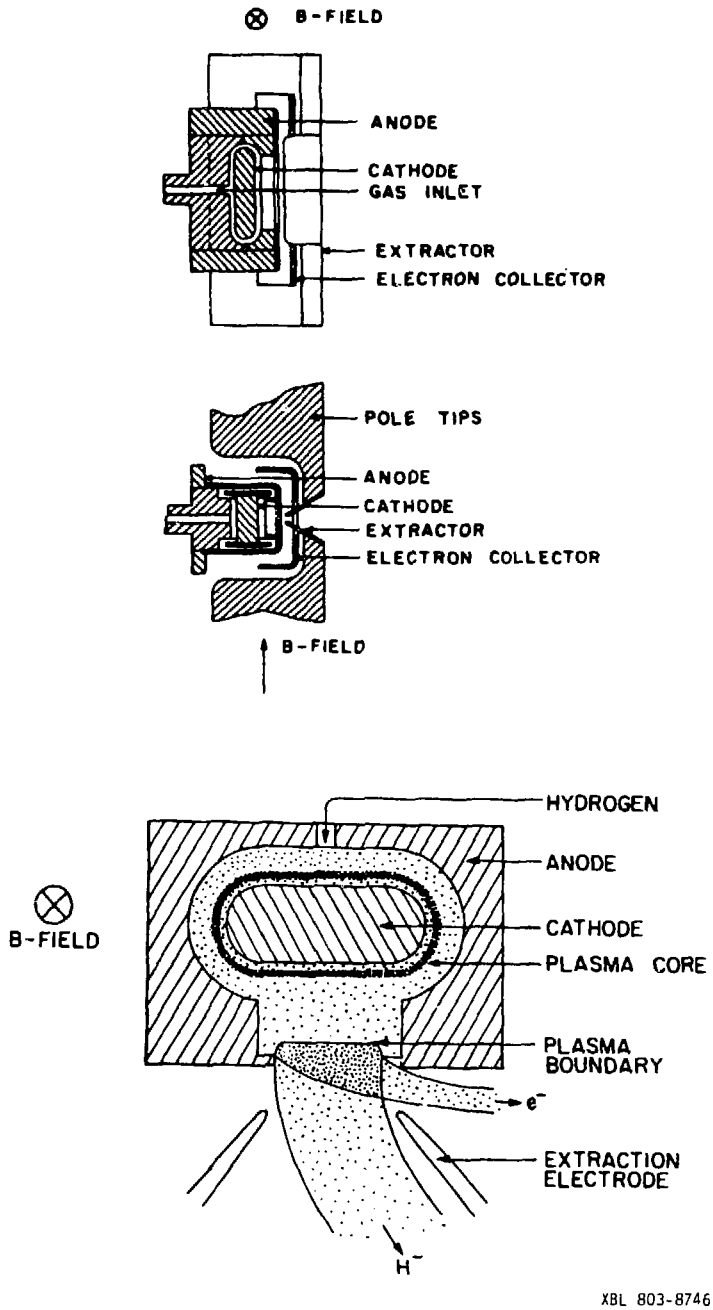

Figure 2. Illustration of the Magnetron negative ion source.

TABLE 1. Magnetron currents and operating parameters for different alkali-metals in the discharge.[9]

	Arc current (A)	Arc voltage	Extraction voltage (kV)	H^- current (mA)	$H^- + e$ current (mA)	Optimum current density (A/cm^2)	Current density at same condition (A/cm^2)	Percentage compared with Cs
Na	290	240	18.5	5.6	60	0.74	0.74	33%
K	350	240	23.3	12	100	1.6	1.32	59%
Cs	400	160	23.2	22	60	2.9	2.25	100%

operating mode than the planetrons and a higher gas efficiency, but does not produce as high current densities.

Although the current densities of the planotrons and Penning sources are within the range required for neutral beam sources, there are several undesirable features that are currently receiving attention, mainly limitation of the pulse length due to rapid cathode heating and poor gas efficiency. Prelec and Sluyters[11] are working with both Magnetron and Penning sources and are trying to improve the pulse length and gas efficiency, as well as integrate these sources into a neutral beamline.

Adapting the Magnetron for a neutral beam system may be difficult. However, it may be possibie to exploit the mechanism by which the Magnetron produces such large negative ion current densities, in a geometry more suitable as a negative ion source. The two presently proposed mechanisms for negative ion production in the Magnetron are surface production and volume productiom. For volume production, the negative ions are produced in the plasma discharge, possibly through the interaction of highly excited states of molecular hydrogen.[12] The volume production mechanism is under investigation by Bacal et al.[13], but it is too early to tell if useful current densities can be obtained. For surface production, the ions are produced by particles bombarding the surfaces in the source.

Belchenko et al.[14] have measured the energy distribution of H^- extracted from a Magnetron source to determine the H^- production mechanism. They found the H^- energy distribution exhibited two peaks: one corresponding to the extraction potential and the second corresponding to the extraction potential plus the discharge potential.

They also found that the ratio of these peak heights depended upon the gas pressure in the discharge. These results led to their conclusion that the primary source of H^- was surface production at the cathode, which resulted in the high energy H^- peak, and the low energy peak was due to charge exchange between high energy H^- and thermal H^0 in the column of the plasma discharge.

Dudnikov et al.[15] have estimated the secondary electron emission coefficient of the cathode surface of a Magnetron and have measured the positive ion current density through a slit in the cathode, as well as the negative ion current density at the emission slit. By operating the Magnetron at various discharge potentials they obtained values of K^-, (the ratio of H^- current density out to positive current density at the cathode), for various surface coverages of Cs on the cathode. At optimum surface conditions, K^- was estimated to be between 0.6 and 0.8. This measurement does not take into account H^- produced by neutrals bombarding the cathode, so it must be an upper limit on the efficiency of surface production of H^-.

There are no measurements of reflected H^- yields from surfaces such as those in the Magnetron (i.e. Cs on a W or Mo substrate), and there is a general lack of H^- yield measurements from low work function surfaces. Therefore, I have measured the total backscattered H^- and D^- yields from various alkali-metal surfaces. The experiment was divided into two parts: (1) clean, thick, alkali-metal targets (Cs, Rb, K, Na, and Li) and (2) thin coverage of alkali-metal on various substrates (including Cs on W and Cs on Mo) were used as the targets. For the thick targets, the incident energy of the hydrogen and deuterium

ions ranged from 0.15- to 4.0 keV/nucleus and for the thin targets the range was from 0.4- to 0.9 keV/nucleus. D_2^+, D_3^+, H_2^+ and H_3^+ were used as incident ions for the thick target measurements. The H_3^+ and D_3^+ ions were used to obtain the lowest incident velocities, since there was a lower limit to the energy of a beam which could be transported through the apparatus. The H_2^+ and D_2^+ were used to check for possible effects arising from different numbers of nuclei per incident molecular ion (i.e. one positive charge among two nuclei or one positive charge among three nuclei). The H^- and D^- yields were normalized to the number of nuclei per incident molecular ion to give H^- per incident proton, and D^- per incident deuteron because at these incident energies, we can consider the incident ions as single protons and deuterons, since the molecular ions are broken up at the target surface.[16,17]

By varying the energy of the incident ions, the work function and the mass of the target, I have attempted to determine which parameters are important to the conversion of incident particles to backscattered negative ions and how these parameters may be varied to optimize the negative ion yield. As a further step in understanding the mechanism of surface production, the H^- and D^- yield curves from thick alkali-metal targets have been fitted with a theoretical expression (discussed in detail in Chapter II) using two variable parameters for each target, which were determined by a least squares fit to the data. The closeness of the fits is very encouraging.

Recently, several related experiments have been reported: Massmann et al.[18] have measured the H^- yield from a ThO_2 target bombarded

CHAPTER II

PRESENT THEORIES OF H^- PRODUCTION FROM SURFACES

Belchenko et al.[8,14,22] and Hiskes et al.[16,21,23,24] have proposed models based upon surface production as the principal mechanism for H^- production in the Magentron and similar sources. Belchenko et al. propose that any hydrogen atom adsorbed to the cathode surface has a high probability of residing as a negative ion and can be desorbed from the surface as a negative ion by an incident energetic particle from the discharge. Furthermore, addition of cesium to the discharge produces cesium coverage of the source surfaces; this lowers the surface work function, enhances the probability of escape without destruction (survival) of the negative ion from the surface and increases the H^- yield. Hiskes et al. have hypothesized that H^- ions are formed in the collision of energetic (1 to 100 eV) hydrogen atoms with adsorbed cesium atoms. As a hydrogen atom approaches a cesium atom, the interaction potential is the sum of the image potential and the difference between the CsH and CsH^- molecular potentials. This interaction potential allows the transfer of an electron from the surface to the hydrogen atom, which may escape from the surface as H^-.

For proposed mechanisms of H^- production from surfaces, it is agreed that three processes are involved: the reflection or desorption of hydrogen from the surface, the formation of the negative ion at the surface, and the survival of the negative ion as it leaves the surface.

Although several treatments for calculating the H^- formation and survival probabilities have been presented,[23-30] they all share the same basic approach, which is outlined below:

When a hydrogen atom is near a surface, a potential interaction (image potential, molecular potential or both) between the atom and the surface changes the electron affinity of the atom relative to the Fermi level of the solid (see Figure 3). The shift of the electron affinity is a function of the separation and can be approximated by:[26]

$$E.A.(x) = E.A._f + \frac{e^2}{4x}$$

where, $E.A.(x)$ is the electron affinity of the atom at x

$E.A._f$ is the electron affinity of the free particle

e is the unit of electronic charge

x is the distance between the atom and the surface

At some distance from the surface, $x_0 = \frac{e^2}{4(\phi_w - E.A._f)}$, where ϕ_w is the surface work function, the electron affinity of H^- is at the same energy level as the Fermi level of the surface. For hydrogen on cesium, x_0 is about $10a_0$ (a_0 is the Bohr radius).[26] For $x < x_0$, the electron affinity lies below the Fermi level and an electron can transfer from the surface to the atom to make an H^- ion. For $x > x_0$, the electron affinity lies above the Fermi level and an electron from the H^- ion can transfer back to the surface.

To obtain expressions for the probabilities of H^- formation and survival, the following terms will be used.

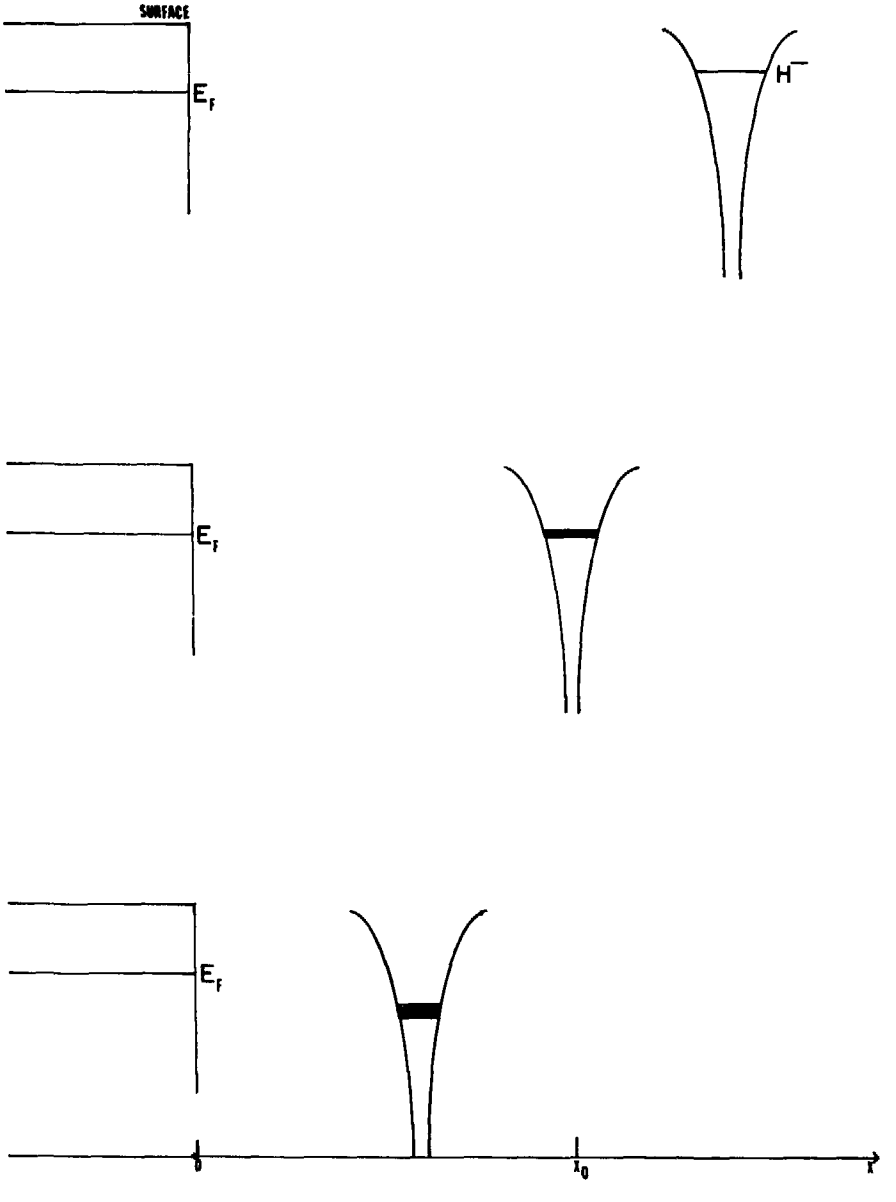

XBL 803-8608

Figure 3. Illustration of the lowering and broadening of the H^- bound level in the vicinity of a surface.

N_t = total number of hydrogen particles leaving the surface.

$N_o(x)$ = number of H^o at a distance, x, from the surface

$N_-(x)$ = number of H^- at x

$P(x)$ = rate at which H^o are converted the H^-

$Q(x)$ = rate at which H^- are converted into H^o

$v_\perp$ = the speed of the particle in the direction perpendicular to the surface.

<u>For H^- Production</u>

$$\frac{dN_-(x)}{dt} = P(x)N_o(x) \tag{1}$$

since $dt = \frac{dx}{v_\perp}$ and $N_o = N_t - N_-$ (neglecting positives),

$$\frac{dN_-(x)}{N_t - N_-(x)} = P(x)\frac{dx}{v_\perp} \tag{2}$$

integrating over x, from x = 0 to $x = x_o$ with $N_-(0) = 0$

$$\ln N_t - \ln (N_t - N_-)) = \frac{1}{v_\perp}\int_o^{x_o} P(x)dx \tag{3}$$

which gives

$$1 - \frac{N_-(x)}{N_t} = e^{-1/v_\perp \int_o^{x_o} P(x)dt} \tag{4}$$

and, since the probability of formation is: $P_- = \frac{N_-(x_o)}{N_t}$,

$$P_- = 1 - e^{-1/v_\perp \int_o^{x_o} P(x)dx} \tag{5}$$

<u>For H^- Survival</u>

$$\frac{dN_-(x)}{dt} = - Q(x)\ N_-(x) \tag{6}$$

and following the same procedure as above, we get the survival probability

$$f = \frac{N_-(\infty)}{N_-(x_o)}$$

$$f = e^{-1/v_\perp \int_{x_o}^{\infty} Q(x)dx} \tag{7}$$

Therefore, the probability that a particle leaving the surface will escape as an H^- is given by:

$$P_-f = (1 - e^{-1/v_\perp \int_o^{x_o} P(x)dx})\ (e^{-1/v_\perp \int_{x_o}^{\infty} Q(x)dx}) \tag{8}$$

To discuss H^- yields in terms of the incident flux to the surface, we must take into consideration that the reflected particles leave the surface with a distribution of velocities. Therefore to obtain the H^- yield, or Negative Ion Secondary Emission Coefficient, (NISEC), the above expression, (8), must be integrated over this velocity distribution:

$$H^- \text{ yield} = \frac{1}{N_i} \int_{\bar{v}} n(\bar{v})(1-e^{-1/v_\perp \int_0^{x_0} P(x)dx})(e^{-1/v_\perp \int_0^{x_0} Q(x)dx})d\bar{v} \quad (9)$$

where $n(\bar{v})$ is the velocity distribution of the reflected particles and N_i is the number of incident particles, such that $\frac{1}{N_i}\int_{\bar{v}} n(\bar{v})d\bar{v}$ is the reflected fraction of the incident flux, R_N.

Kishnevskiy[26] has derived a form for the neutralization rate of H^-, $Q(x)$, and solved for the survival probability for hydrogen leaving various low work function surfaces. His results are reproduced in Figure 4 and, as can be seen, there is a strong energy dependence of f on work function only for very low exit velocities, $v_\perp$. In fact, Kishnevskiy[26] notes that almost all particles leaving a low work function surface with energies of the order of tens of electron Volts should be emitted as negative ions.

Hiskes and Karo[23,24] have considered H^- formation from two kinds of targets: (1) targets composed of a single atomic species and (2) transition metal targets with a partial monolayer converage of cesium. A schematic drawing of the interaction potential energy used for

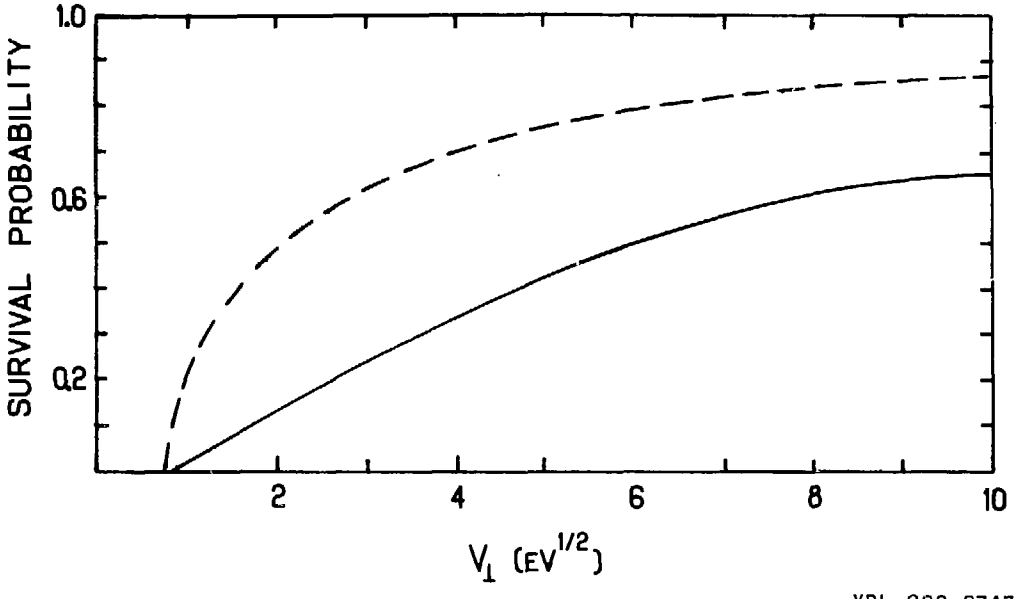

XBL 803-8747

Figure 4. Results of the calculation of Kishinevskii[26] for the survival probability of H^- leaving a surface. The results are shown as a function of exit velocity at fixed work functions of 1.3 eV --, and 1.7 eV —.

hydrogen bombarding a single species surface is shown in Figure 5a. This potential function has been used to calculate the survival probability for H^- leaving thick cesium and potassium targets. The results show that the survivial probability has a strong energy dependence up to at least 100 eV. The potential in Figure 5a is similar to the image force potential of Kishinevskiy, so as expected, the calculations of Hiskes and Karo[23,24] agree fairly well, except at the lowest incident energies, with those of Kishinevskiy[26] (see Figure 6).

A schematic drawing of the interaction potential energy for hydrogen bombarding a surface with a partial monolayer of Cs coverage is shown in Figure 5b. The difference between the two potential energy diagrams in Figure 5 is the potential barrier at the surface (at $-20\ a_0$ in the Figure). This barrier is produced by the partial monolayer of cesium on the substrate, which creates an electric dipole layer at the surface. As a result of this barrier, the probability that an electron will tunnel back to the surface from an H^- ion is greatly reduced. The survival probability corresponding to this potential function is also shown in Figure 6, and as can be seen, it is essentially unity for energies as low as 1 eV. Therefore, for a partial monolayer coverage of cesium, the dominant factors determining the H^- yield are the probabilities of reflection and formation.

Hiskes and Karo[23,24] describe the probability of formation of H^- as an electron tunneling through a potential barrier and use a WKB formula to obtain an analytic form of this probability. This result, combined with the survival probability and the calculations of Oen and

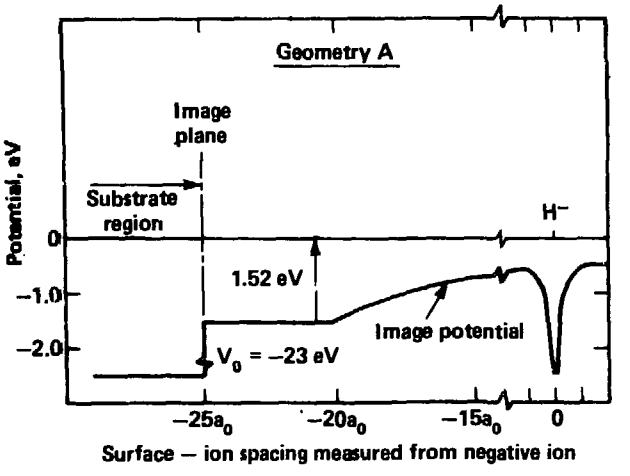

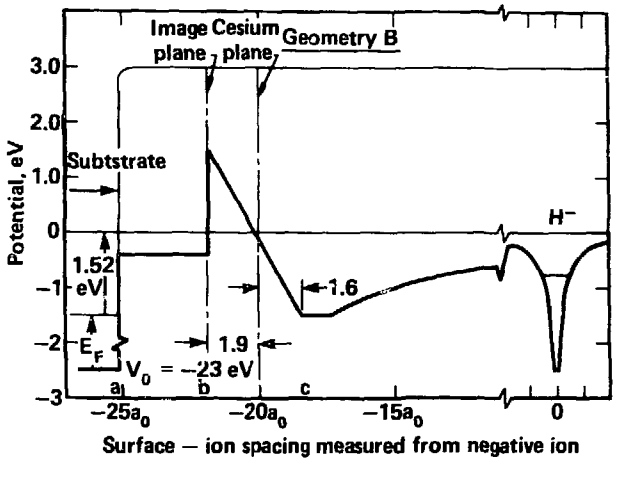

XBL 803-8748

Figure 5. Illustration of the interaction potential used by Hiskes and Karo[23] to calculate the survival probability for H^- leaving a surface, (a) with a thick coverage of alkali metal and (b) with a partial monolayer of Cs on W.

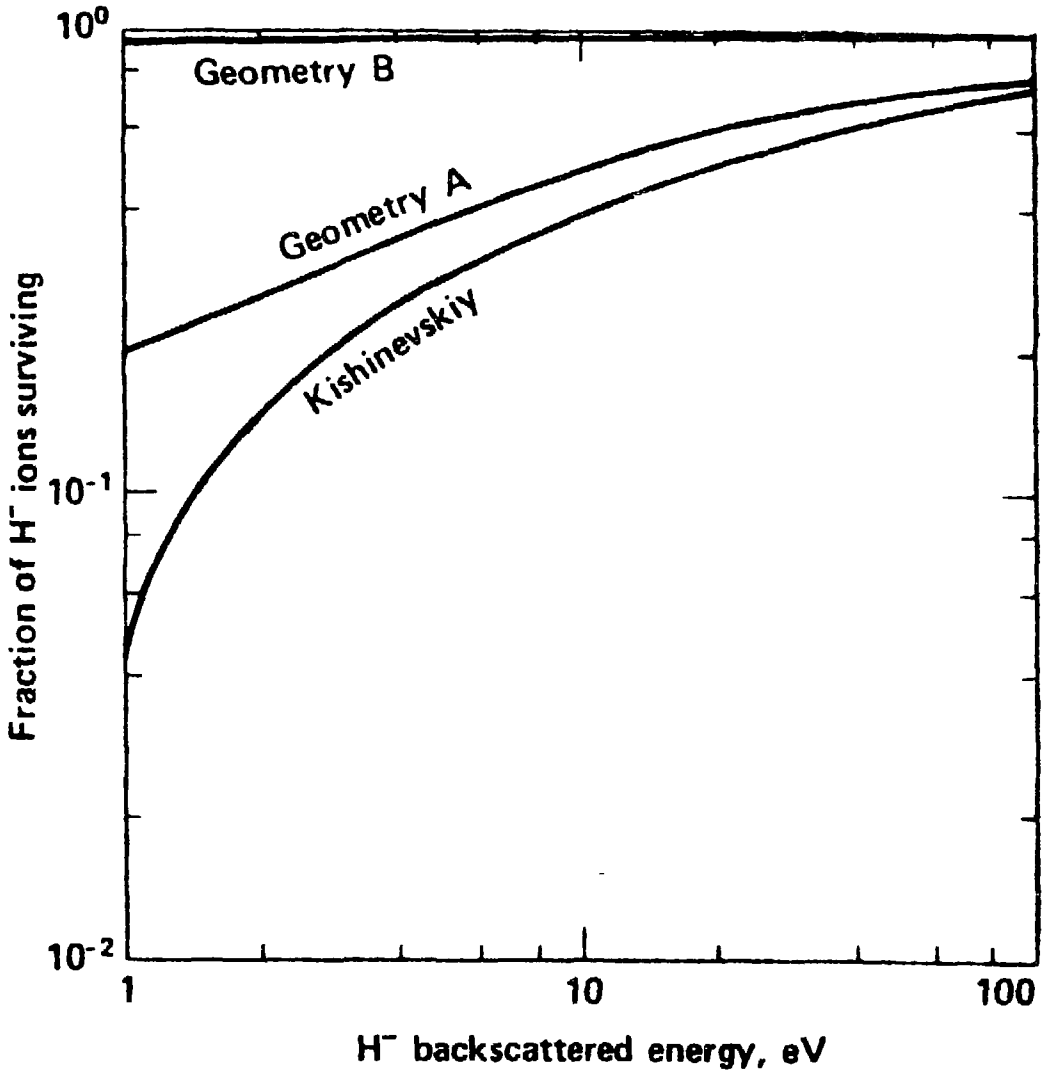

XBL 803-8645

Figure 6. Comparison of the results of calculations by Kishinevsky[26] and Hiskes and Karo[23] for H^- survival probability as a function of exit energy.

C. Data Fitting

Hiskes and Schneider[47] have developed a technique to quantitatively determine the dependence of the NISEC upon R_N, f and P_-: The Marlowe[31] code was used to obtain the angular and energy distributions of protons and deuterons reflected from each of the alkali-metal targets. The angular distribution closely approximated a cosine distribution so that n(v)dv could be separated into two parts and the angular dependence integrated out of equation (9) of Chapter II (see Appendix F), giving:

$$\text{NISEC} = \frac{1}{N_i}\int_v \Bigg[e^{-\beta/v}[1 - \beta/v - e^{\alpha/v}(1 - \tfrac{\alpha+\beta}{v})]$$

$$- \frac{\beta^2}{v}[\gamma + n(\beta/v) + \sum_{n=1}^{\infty} \frac{(-1)^n \beta^n}{nn!v^n}]$$

$$+ (\tfrac{\alpha+\beta}{v})^2 [\gamma + \ln \tfrac{\alpha+\beta}{v} + \sum_{n=1}^{\infty} \frac{(-1)^n(\alpha+\beta)^n}{nn!v}]\Bigg] n(v)dv$$

where

$$\alpha = \int_0^{x_0} P(x)dx$$

$$\beta = \int_0^{\infty} Q(x)dx$$

γ = 0.57722.... = Euler's constant.

CHAPTER III

EXPERIMENTAL APPROACH AND APPARATUS

A. Approach

A beam of D_2^+ and D_3^+ (H_2^+ and H_3^+) ions was extracted from a hot filament discharge, accelerated to the desired energy and momentum analyzed with a 30° bending magnet before entering the experimental chamber (Figure 7). The apparatus within the chamber (Figure 8) was designed around two parallel rectangular plates, perpendicular to the beamline; an aperture in the first plate (the collector) allowed the beam to pass through to the second plate (the target), from which $D^-(H^-)$, $D^0(H^0)$, $D^+(H^0)$, $D^+(H^+)$ and electrons as well as sputtered particles (Fig. 9) were emitted. The collector was was used to monitor the negative ion current, therefore all other charged particles had to be prevented from reaching it: An electric field between the target and collector plates prevented positive secondary ions from reaching the collector and a transverse magnetic field suppressed secondary electrons. Also, an upbeam collimator shielded the collector from the primary beam. This collimator was the end-plate of a Faraday cup (the collimator-Faraday cup) which was used to determine the total current incident on the target: The total incident current was determined by the difference in current readings from the collimator-Faraday cup when the beam was deflected into the cup and when it was steered through the cup by a pair of upbeam deflection plates. The Negative Ion Secondary Emission Coefficient (NISEC) was determined by taking the ratio of the collector current to the total incident current and dividing by the number of nuclei per incident molecular ion.

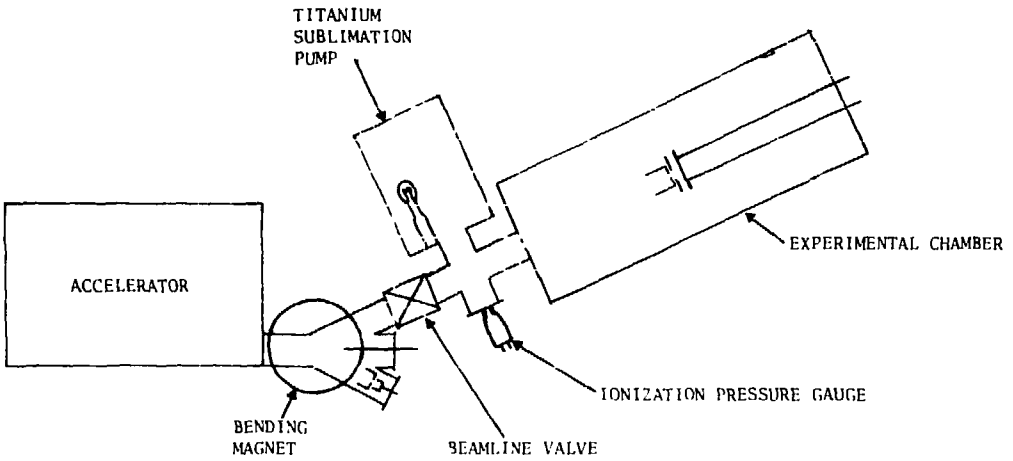

XBL 803-8622

Figure 7. Block diagram of the major parts of the apparatus.

TABLE 2. Tabulation of the values used in the least squares fit of the NISEC data.

Target	Beam	E_{inc} (eV)	A_1^*	A_2	A_3	A_4	A_5	A_6	A_7	A_8	A_9	A_{10}	$NISEC_e^\dagger$
Cs	H	200	1.2	3.6	6.0	13.3	24.5	36.6	62.0	67.8	109.8	114.2	73
		300	2.6	7.7	12.8	20.2	28.0	34.0	43.3	61.4	103.4	107.3	76
		500	3.2	9.5	15.9	21.7	29.8	34.6	52.9	59.4	86.4	77.7	72
		700	3.3	9.9	16.5	20.1	25.7	34.2	43.8	58.7	99.2	73.6	69
		1000	3.0	8.9	14.8	17.1	26.0	37.5	48.4	60.5	77.3	55.2	61
	D	150	1.8	5.4	9.0	16.2	19.7	27.9	39.0	70.9	126.2	145.9	60
		300	3.0	9.0	15.0	20.4	25.6	37.2	48.9	75.7	108.1	104.0	75
		500	2.4	7.2	12.0	21.0	26.9	41.3	46.9	80.6	96.4	77.4	79
		700	3.6	10.8	18.0	20.4	24.2	31.0	37.2	65.7	90.5	76.7	78
		1000	1.6	4.8	8.0	23.1	29.5	34.8	50.9	79.5	87.8	76.0	74
		1500	2.0	6.0	10.0	14.6	28.1	40.5	49.6	55.4	90.6	71.1	66
Rb	H	300	3.0	9.0	15.0	15.1	24.3	37.5	40.2	64.9	72.3	79.7	55
		500	2.9	8.7	14.5	17.3	25.0	40.0	46.1	51.5	79.7	47.3	57
		700	2.4	7.2	12.0	18.0	28.2	36.7	43.9	51.8	77.5	40.4	57
		1000	1.8	5.4	9.0	18.5	25.7	35.4	41.0	46.8	60.8	51.5	55
	D	200	1.3	3.9	6.5	20.4	27.3	34.8	41.5	65.2	97.4	78.6	40
		300	1.8	5.4	9.0	17.4	29.2	31.3	50.1	66.9	80.2	65.7	48
		500	1.3	3.9	6.5	13.9	24.2	36.9	37.5	64.9	74.9	56.0	56
		700	1.3	3.9	6.5	13.9	21.8	37.3	44.9	65.8	61.2	44.5	57
		1000	2.4	7.2	12.0	15.0	21.8	28.0	48.2	60.5	80.5	45.5	55
		2000	1.8	5.4	9.0	11.4	17.3	30.6	40.2	40.9	66.5	30.8	46
K	H	300	1.9	5.7	9.5	19.3	23.7	28.7	38.2	45.5	61.3	31.2	38
		500	1.9	5.7	9.5	16.3	25.9	27.5	34.1	46.6	37.3	30.2	40
		700	2.1	6.3	10.5	14.7	18.9	26.0	31.1	31.5	39.8	22.1	38
		1000	2.3	6.9	11.5	10.7	20.8	28.8	28.6	28.6	27.0	20.1	23
		3000	1.4	4.2	7.0	13.4	16.1	19.9	17.9	17.9	13.5	4.7	18
	D	300	2.3	6.9	11.5	13.1	24.4	33.2	29.3	42.9	45.2	17.2	27
		500	1.5	4.5	7.5	14.3	19.8	23.0	33.4	45.8	55.9	16.8	32.5
		1000	1.2	3.6	6.0	13.2	19.9	24.6	38.9	46.7	37.3	12.7	34
		2000	1.8	5.4	9.0	15.0	17.4	25.7	29.7	28.4	24.3	6.3	26.5

(continued . . .)

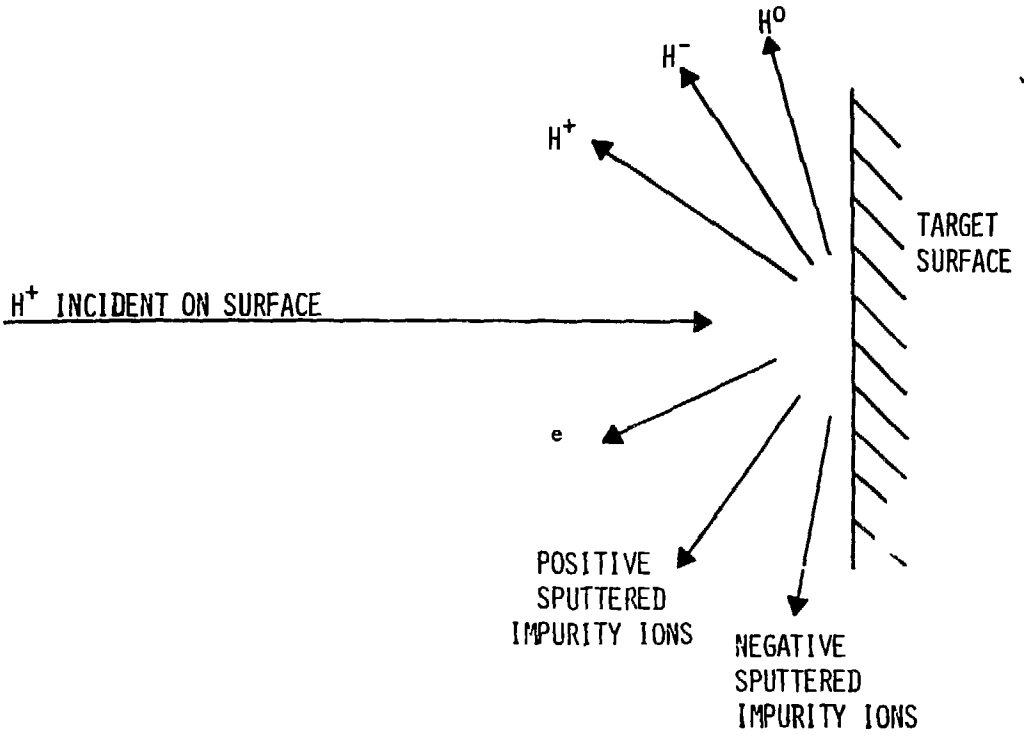

XBL 803-8617

Figure 9. Illustration of beam impact on the target surface.

The clean alkali-metal targets were deposited onto various substrates in the experimental chamber, which was maintained at a pressure less than 10^{-9} Torr. The target surfaces conditions were monitored with two techniques: mass analysis of the positive and negative ions leaving the surface and surface work function measurements.

B. Apparatus

A line drawing of the major parts of the apparatus is given in Figure 7.

1. Accelerator

The electrostatic accelerator had a hot-filament-discharge ion source (Fig. 10), which was biased to the electrical potential equivalent to the desired beam energy. The ions were produced in a discharge maintained between the anode and a 0.5 mm tungsten filament, which was heated to emit electrons by passing a current of up to 25 A through it. A potential difference of up to 120 Volts was applied between the anode and the filament to maintain the discharge and the appropriate gas (i.e. H_2 for hydrogen ion beams) was bled into the discharge through a needle valve. The pressure in the area of the discharge was about 1×10^{-3} Torr.

The ions leaving the discharge passed through a pumping impedance and were extracted and focused by an electrostatic lens. The accelerated ions then passed between horizontal and vertical deflection plates before passing through the 30° momentum analysis magnet. The background pressure in this area and on to the beamline entrance was maintained at 1×10^{-5} Torr by an oil diffusion pump with a liquid-nitrogen-cooled baffle.

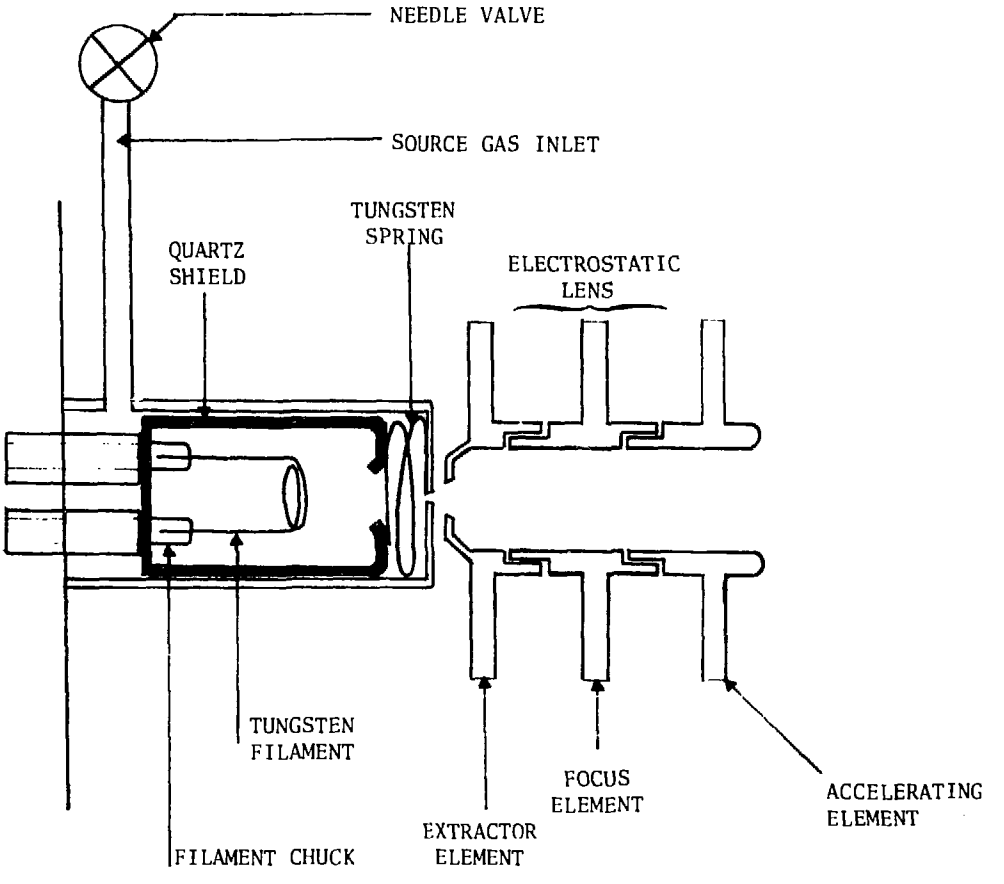

XBL 803-8621

Figure 10. Accelerator source and electrostatic lens.

2. Magnet and Beamline

The momentum analysis magnet was used to select the ion species which would continue on to the experimental chamber. The magnet had three exit ports: 30° East, neutral and 30° West. The 30° East port led to two concentric Faraday cups which were used to examine the beam from the accelerator. The neutral port held a Hall probe for monitoring the magnetic field strength and the 30° West port opened into the beamline.

At the entrance of the beamline, a pumping impedance consisting of a tube 4 cm long and 1.2 cm in diameter was used to help maintain a vacuum differential between the beamline and accelerator. A manual isolation valve was located directly after the pumping impedance and allowed the accelerator to be brought up to air pressure while the experimental chamber remained under vacuum. The beamlime was 30 cm long and was terminated by another pumping impedance, consisting of a 0.15 cm diameter aperture, at the entrance of the experimental chamber.

The beamline was pumped by a titanium sublimation pump, mounted in a right angle cross in the beamline. The beamline pressure, as read on an ionization gage, was 5×10^{-8} Torr with the beam off, and about 1×10^{-6} Torr with the beam on.

3. Experimental chamber

The experimental chamber consisted of a cylindrical shell, 70 cm long and 20 cm in diameter, with its axis oriented along the beamline. This chamber constituted the ultra-high-vacuum region of the apparatus; normal operating pressure is about 8×10^{-10} Torr, with a base pres-

sure of 1×10^{-10} Torr. Three pumps were used to attain this vacuum: First, the chamber was pumped by a Kinney roughing pump, through a liquid nitrogen trap, to a pressure of 1×10^{-3} Torr. A vac-ion pump was then turned on and the roughing pump was valved off. Pumping the chamber with the vac-ion pump in conjunction with baking (using a quartz lamp inside the chamber) to a temperature of 280°C brought the base pressure down to 3×10^{-9} Torr.

A liquid-helium cryopump[32] was used to further reduce the pressure The cryopump consists of a liquid helium reservoir surrounded by a liquid nitrogen shield baffle. Adding liquid nitrogen to the cryopump reduced the pressure of 1×10^{-9} Torr and then adding liquid helium reduced the pressure to 1×10^{-10} Torr.

The cryopump and the vac-ion pump were used simultaneously throughout this experiment, even though the base pressure of the vac-ion pump is higher than 1×10^{-10} Torr. When a gate valve was used to enable isolation of the vac-ion pump, it was found that the outgassing of the "O" rings in the valve prevented the chamber base pressure from going below 1×10^{-9} Torr.

The position of the pumps on the experimental chamber, as well as the locations of the apparatus within the chamber are shown in Figure 11. In the following section, each part of the apparatus within the chamber will be presented in the order in which the incoming beam encounters it.

At the entrance of the experimental chamber, an aperture of 0.15 cm diameter (the entrance collimator in Figure 8) served a dual purpose:

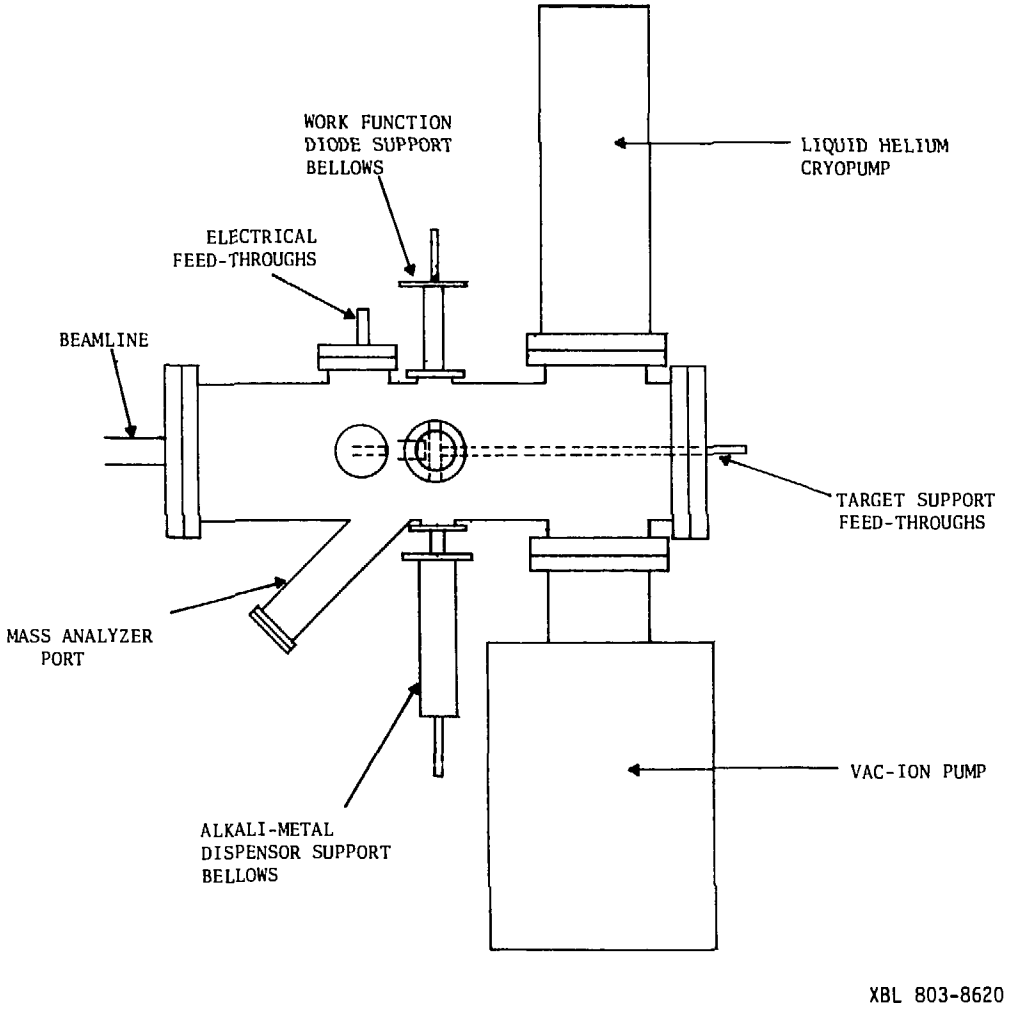

Figure 11. Line drawing of the experimental chamber.

Besides being a pumping impedance between the beamline and the chamber, it also serves as the first of two collimators which define the beam diameter.

Twenty centimeters beyond the entrance collimator, the beam passed between a pair of horizontal deflection plates, which were 5 cm wide, 9 cm long and separated by 1.5 cm. Besides being used in the measurement of the total current incident on the target, these plates were necessary to compensate for the steering effects, on the beam, of the stray magnetic field from the electromagnet.

The beam entered the collimator-Faraday cup 5 cm beyond the deflection plates. This cup, which was 2.5 cm in diameter, 4 cm long and had a 0.15 cm diameter exit aperture, was used to measure the total current incident on the target, as well as shield the collector from the incident beam. The collimator-Faraday cup was mounted in a machinable-glass ceramic insulator along with the collector (Figure 12). A grounded metal shield surrounded the insulator to prevent it from collecting stray charged particles, and the entire unit was supported by two sets of four adjustable screws to allow alignment along the beamline. The insulator was used to maintain the separation between the collimator-Faraday cup and the collecter at 0.08 cm.

The collector consisted of two parts: a cup, 2.85 cm in diameter, 0.6 cm deep, with a 0.25 cm wide diameter aperture on axis, and a rectangular plate, 7.3 cm high, 5 cm wide, with a 1.0 cm diameter aperture in the center and an irregular aperture (Figure 12) located 0.85 cm below the center. The center aperture allowed the incident beam to reach the target and the lower aperture allowed ions leaving the

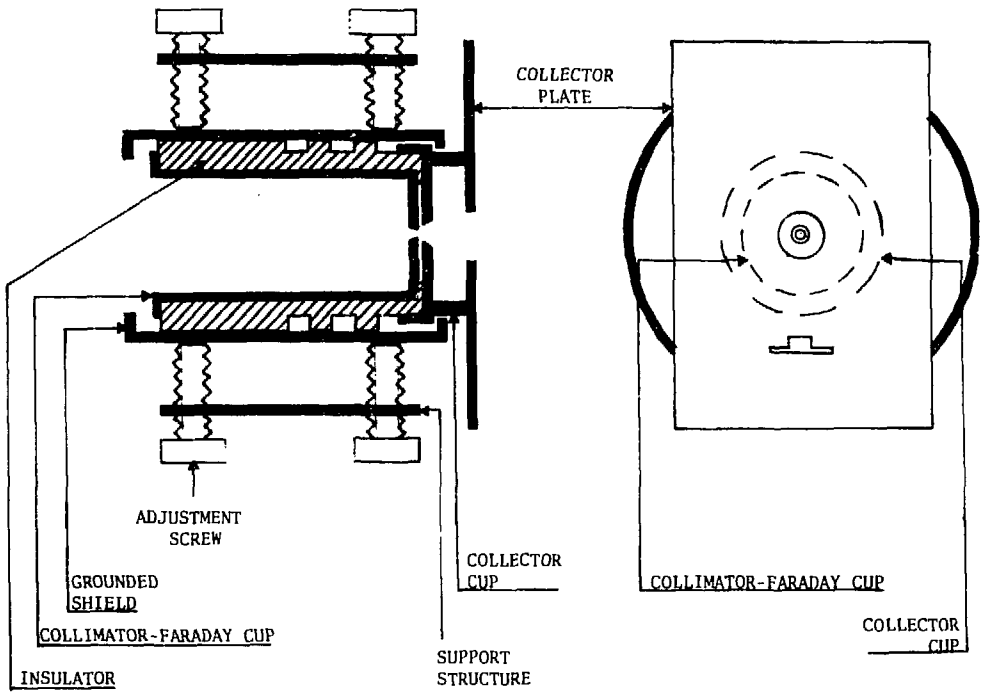

Figure 12. Collector and collimator-Faraday cup with support structure.

target surface to be analyzed by the mass analyzer. The plate was held onto the cup by a metal spring welded to the back of the plate, and could be slipped on and off without disturbing the alignment of the cup and the collimator-Faraday cup. The currents from the collimator-Faraday cup and the collector were monitored on Keithley model 410 picoammeters, as shown in the block diagram of the electronics, Figure 13.

The target was 1.3 cm beyond the collector plate and was also 7.3 cm high and 5 cm wide to ensure a uniform electric field between the two plates: The target could be biased to -6000 Volts to suppress positive ions leaving the target surface. Two target structures were used: One structure could be cooled with liquid nitrogen to 77K and was used for measurements from thick alkali-metal targets, and the other allowed the target to be heated to 1400K by radiation from a filament behind it, and was used for measurements from thin alkali metal targets. The heated (cooled) target was supported by two rods (tubes), 40 cm long and 0.6 cm in diameter. The rods (tubes) were mounted on insulated feed-throughs at the rear flange of the experimental chamber. With this geometry, the insulated feed-throughs are far enough from the crossed electric and magnetic fields to avoid charge-up problems from drifting secondary electrons.

The transverse magnetic field used to suppress electrons from the target, the collector and the collimator-Faraday cup was produced by an electromagnet with a 6.5 cm gap and 5 cm diameter poles. The magnetic field strength at the center of the gap could be varied from 0 to 1000 gauss, and the polarity of the field could be reversed by interchanging the electrical connections to the magnet.

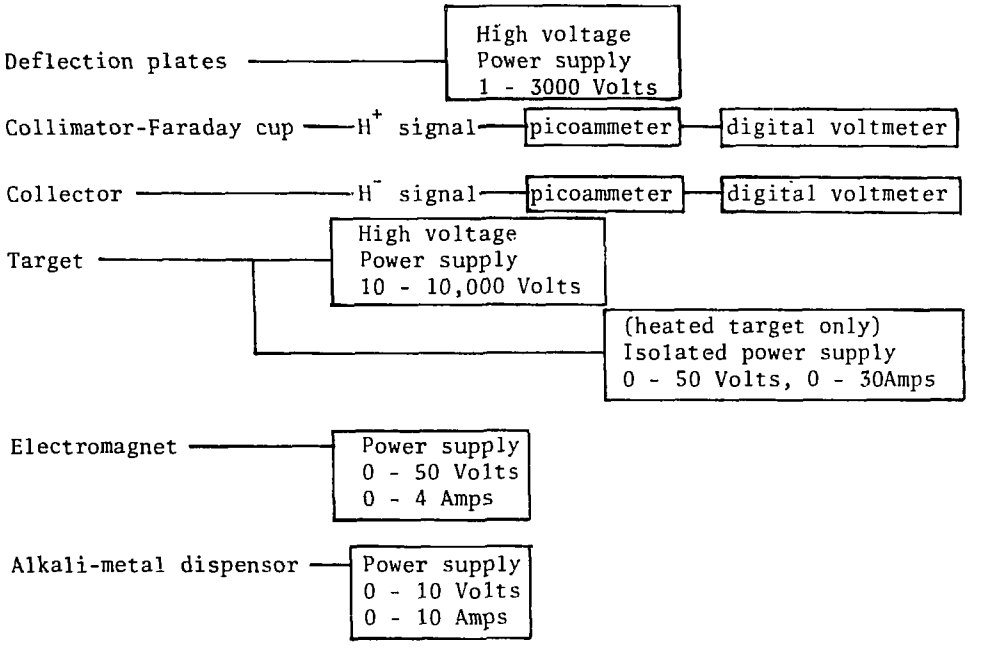

XBL 803-8618

Figure 13. Block diagram of the electronics used for measuring the NISEC.

The clean alkali-metal targets were deposited on a substrate within the experimental chamber. Two S.A.E.S.[33] alkali-metal dispensors, with 1.4 cm active length, were mounted parallel to each other on a bellows with 7.5 cm of travel. The dispensors were 0.6 cm apart and could be positioned between the target and collector plates, 0.6 cm away from the target surface, to coat the target area. The thickness of the alkali-metal layer was determined by the current through the dispenser (6 to 8 Amperes), the evaporation time and the temperature of the target.

The work function of the target was monitored by the electron beam retarding potential method[33-35] (see Appendix B). A tungsten filament, from a flashlight bulb, was mounted in a stainless steel tube, 0.6 cm in diameter and 1.0 cm long. The tube had a mask at the exit with a 0.25 cm diameter aperture to limit the surface area sampled by the filament. The tube was mounted on a bellows, with 7.5 cm of travel, and could be moved between the target and collector plates to sample the beam impact area of the target. The filament was heated by passing a current of 200 mA through it, and the current collected by the target was recorded as a ramp voltage (0 to 10 Volts) was applied between the filament and the target. As the surface work function changed, the current-voltage curve shifted along the voltage axis, with the shift in voltage corresponding to the change in the work function. A block diagram of the electronics for monitoring the work function is given in Figure 14.

Qualitative analysis of the ions present on the target surface was done with an electrostatic quadrupole mass analyzer.[37] Both positive and negative ions leaving the target surface at an angle of 45° to the

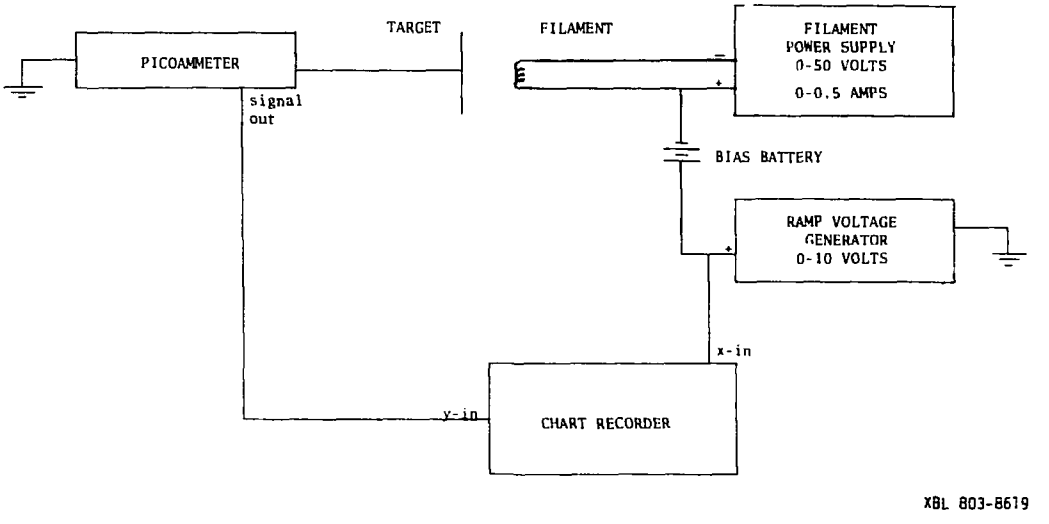

Figure 14. Block diagram of the electronics for monitoring the work function.

normal pass through the irregular aperture in the collector plate and on into the entrance of the mass analyzer. The entrance aperture was 0.6 cm in diameter and 20 cm from the target surface. Within the analyzer, the ions pass between four cylindrical rods which are biased to produce a combination of steady state and oscillating electric fields. Only ions of the selected mass can pass along the rods to the exit aperture. Once through the exit aperture, an electric field accelerates either the positive or the negative ions into an electron multiplier (Channeltron). The pulses from the electron multiplier are counted as the ratio of the amplitudes of the steady state and oscillating electric fields is varied to produce a mass spectrum of the ions from the target. A block diagram for processing the mass analyzer ouptut is shown in Figure 15, and a further discussion is given in Appendix A.

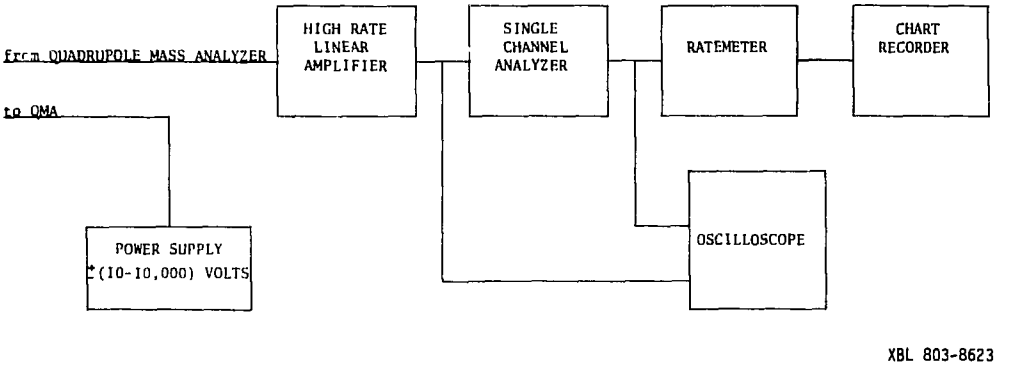

Figure 15. Block diagram of the electronics for processing the mass analyzer output.

CHAPTER IV

EXPERIMENTAL MEASUREMENTS

The measurements undertaken in this experiment can be divided into two parts: NISEC measurements from thick metal targets (when the target is evaporated onto a substrate such that the metal layer is thick enough to completely mask the substrate from the incident beam), and measurements from thin metal targets (partial monolayer to many monolayer coverage of the substrate). Each set of measurements will be treated below. Before any measurements could be made, several experiments were performed to establish the dimensions and operating parameters of the apparatus used.

A. Operating Parameters

To assure that all of the negative ions produced at the target were collected, a series of electrically isolated masks was used to vary the collector width from 0.8 cm to 4.5 cm. The height of the collector was 7.3 cm for all the masks except the one corresponding to a width of 4.5 cm; with this mask the collector height was reduced to 6.3 cm. The ratio of the signal from the collector to the sum of the signals from the collector and the mask was measured for the various collector widths. The results shown in Figure 16 are for 2.5- and 6.0 keV/nucleus D_3^+ incident on untreated molybdenum target, and as can be seen, all the negative ions are collected for widths greater than 3.3 cm. Also, since there was no change in the measured ratio when the collector height was reduced to 6.3 cm, the collector dimensions of 5 cm by 7.3 cm were sufficient to collect all the negative ions.

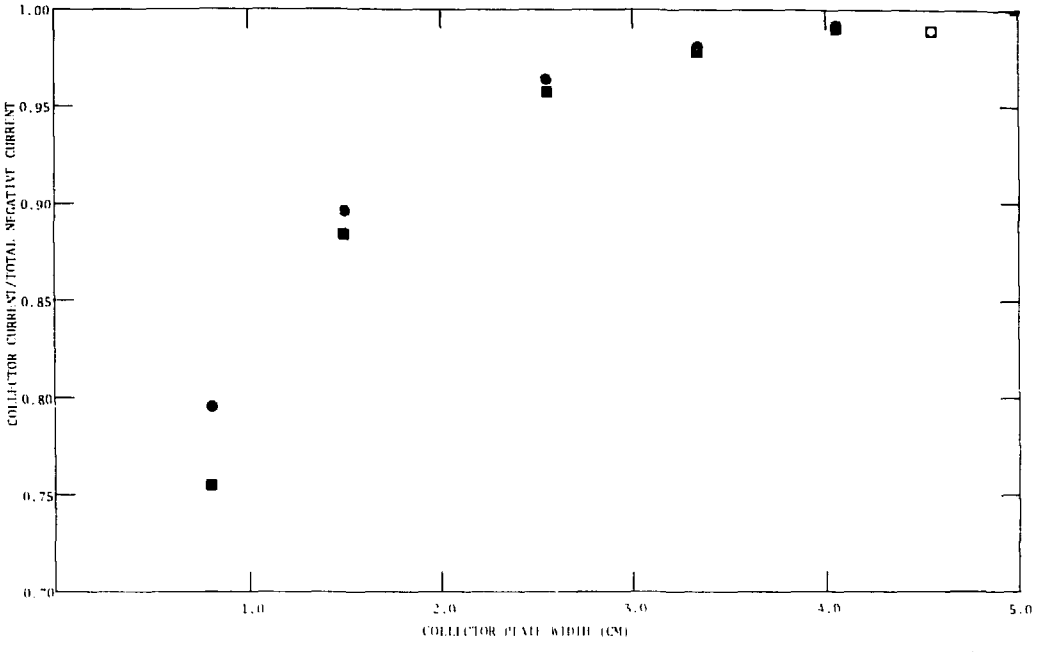

XBL 803-8615

Figure 16. Results of varying the effective width of the collector plate. The fraction of collected signal on the collector plate is plotted against the collector width for 2.5 keV/nucleus D_3^+ on untreated molybdenun-- ●, and for 6 keV/nucleus D_3^+ on untreated molybdenum-- ■.

The 0.25 cm diameter aperture which allowed the incident beam to pass through the collector to the target could also allow negative ions from the target to pass through without being collected. To investigate this effect, NISEC measurements were made using three aperture diameters: 0.25 cm, 0.50 cm and 0.70 cm. A rubidium target was used for these measurements and the incident energy was varied from 0.4- to 5.0 keV/nucleus (Figure 17). The results for each aperture were normalized to those of the 0.25 cm diameter aperture and plotted against the square of the aperture diameter (which is proportional to the area through which the negative ions can escape), as shown in Figure 18. Extrapolating the data to zero aperture diameter gives the fraction of the negative ions which are lost, and for 0.25 cm this is less than 3 percent.

Positive ions produced by backscattered particles (atoms and negative ions) striking the collector could not be suppressed. The current due to these ions leaving the collector adds to the current from the collected negative ions and is a possible source of error. To investigate the magnitude of this effect, the NISEC was measured for a sodium target, with a stainless steel collector. Then the target was heated to evaporate the sodium onto the collector. The dispensor was used to re-coat the target with sodium and the NISEC measurement was repeated. Changing the collector surface from stainless steel to sodium changes the collector work function from 4 eV to 2.3 eV and greatly changes the charge distribution of the backscattered particles leaving the collector (very few positive ions leave the sodium surface). No difference was seen in the NISEC measurements using the two collector surfaces.

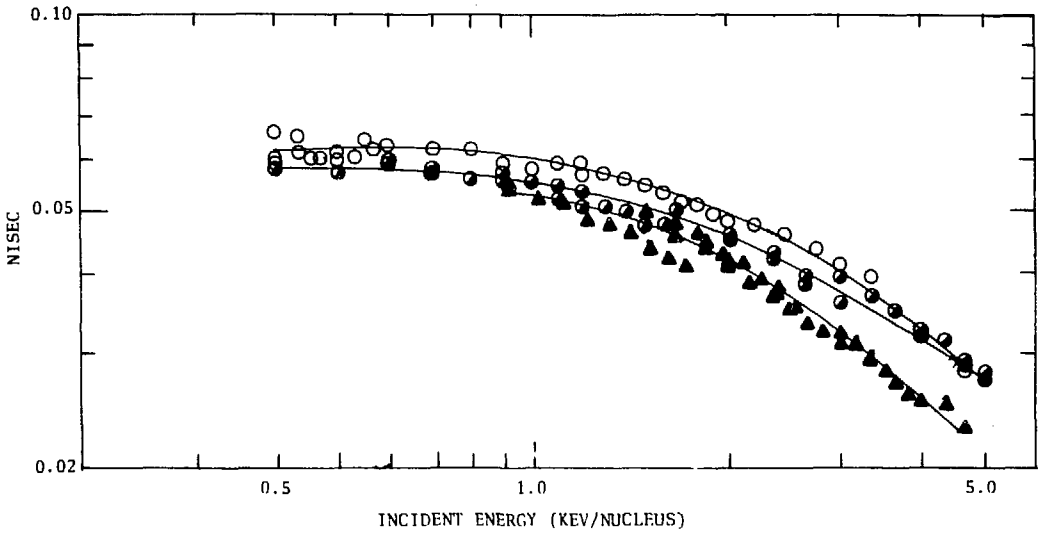

XBL 803-8614

Figure 17. The negative ion secondary emission coefficient (NISEC) for a rubidium target bombarded by D_2^+ and D_3^+ with incident energies from 0.5-to-5.0 keV/nucleus for three collector plate aperture diameters: 0.25 cm-- ○ , 0.50 cm-- ◐ , 0.70 cm-- ▲ .

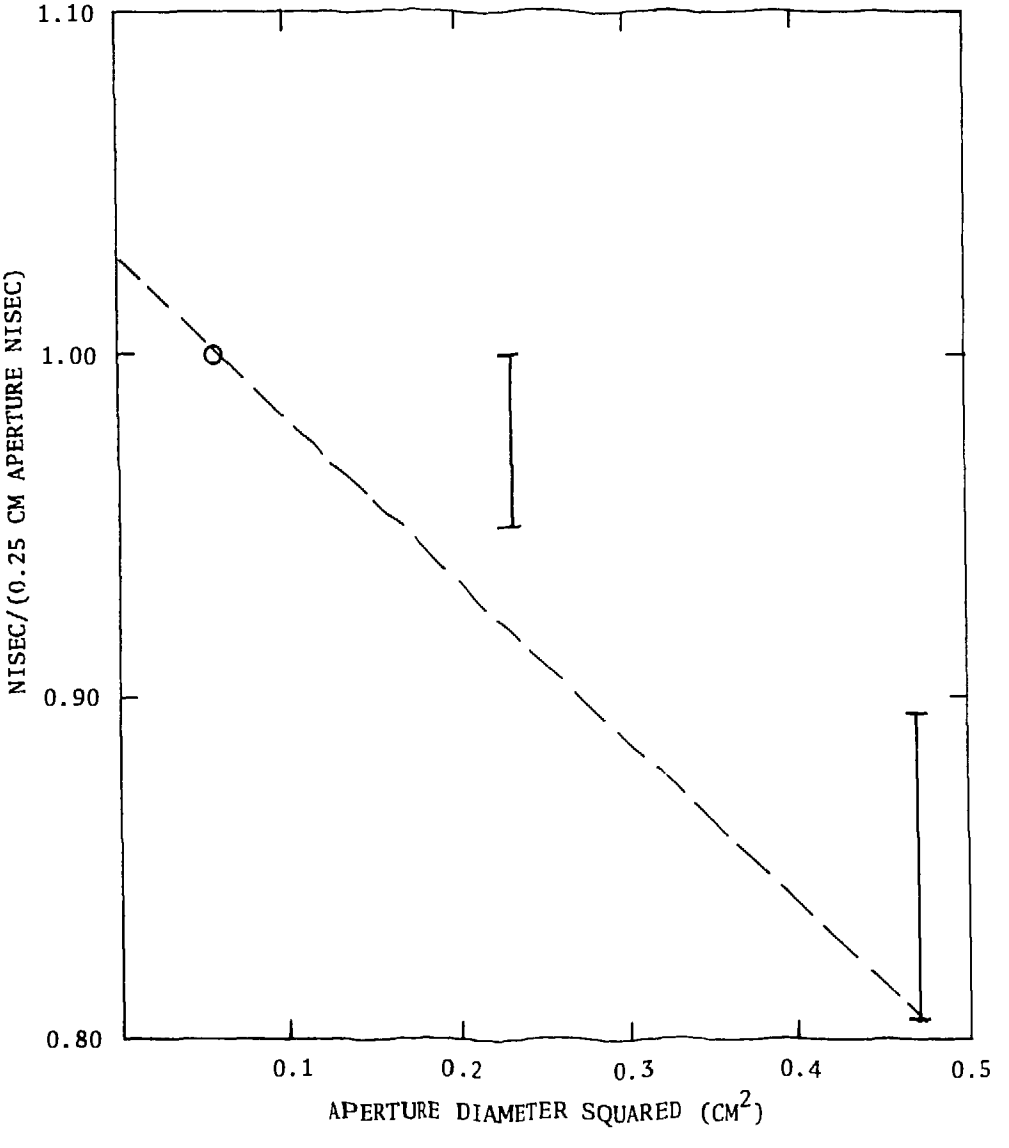

XBL 803-8613

Figure 18. The NISEC data shown in Figure 17 has been normalized to the values for the 0.25-cm-diameter aperture and extrapolated to zero aperture diameter.

Meishner and Verbeck[38] and Eckstein et al.[39] have measured the ratio of protons to neutrals emerging from various metal targets as a function of exit energy and angle. Their results indicate that for an exit energy of 1 keV, less than 5 percent of the emerging particles are positive ions, with the positive ion fraction dropping off rapidly at lower energies. These results, along with my own measurements using the two collector surfaces, led to the conclusion that the effect of positive ions leaving the collector was less than the differences in reproducibility of the experimental measurements (5 percent).

The electric field used to suppress positive ions from the target was produced by applying a negative voltage to the target. The magnitude of the applied voltage was determined by the beam species and energy. As an example, a 5.0-keV beam of D_3^+ required a target bias of at least -2.5 keV. The target bias adds to the incident energy giving a total incident energy of 7.5 keV; assuming that the energy is divided equally between the three deuterons as the incident ion breaks up at the surface, the maximum energy that a reflected D^+ ion can have is 2.5 keV, which is not sufficient for it to reach the collector plate. In this experiment, no measurements were made using D^+ or H^+ as incident particles because the maximum reflected energy would always be greater than the retarding voltage, so that the high-energy backscattered positive ions could not be prevented from reaching the collector.

A transverse magnetic field was used to suppress secondary electrons from the target, the collector and the collimator-Faraday cup. The suppression of secondary electrons is illustrated in Figure 19, where the "apparent" NISEC is plotted vs the magnitude of the magnetic field for D_3^+ incident energies of: 1 keV/nucleus, 2.5 keV/nucleus and 4 keV/ nucleus. At low magnetic fields the signals are dominated by secondary electrons, but as the field is increased, the electrons are suppressed--first for the lowest incident energy and then for successively higher energies. For the lowest incident energy in Figure 19 (1 keV/nucleus D_3^+, E_{gap} = 0.91 kV/cm) 140 gauss is sufficient for complete electron suppression, whereas for the highest incident energy, (4 keV/nucleus, E_{gap} = 3.6 kV/cm) 360 gauss is necessary. Calculations for trajectories of H^- ions emitted from the target show that all negative ions (even those emitted with zero energy) reach the collector for all electric and magnetic fields used in this experiment (see Appendix C).

Because the gap (6.5 cm) between the electromagnet poles is greater than the pole diameter (5.0 cm), the magnetic field produced by the magnet is non-uniform. To determine if this non-union field affected the NISEC measurements, the collector, the target and the collimator-Faraday cup were moved to center the target-collector gap at the edge of the magnet poles. NISEC measurements were made using 1.0- and 2.5 keV/nucleus D_3^+ on untreated molybdenum with this geometry, and were compared to measurements made with the collector-target gap centered in the magnet poles. No difference in the NISEC was observed, but as can be seen from Figure 20, a much higher magnetic field strength (as

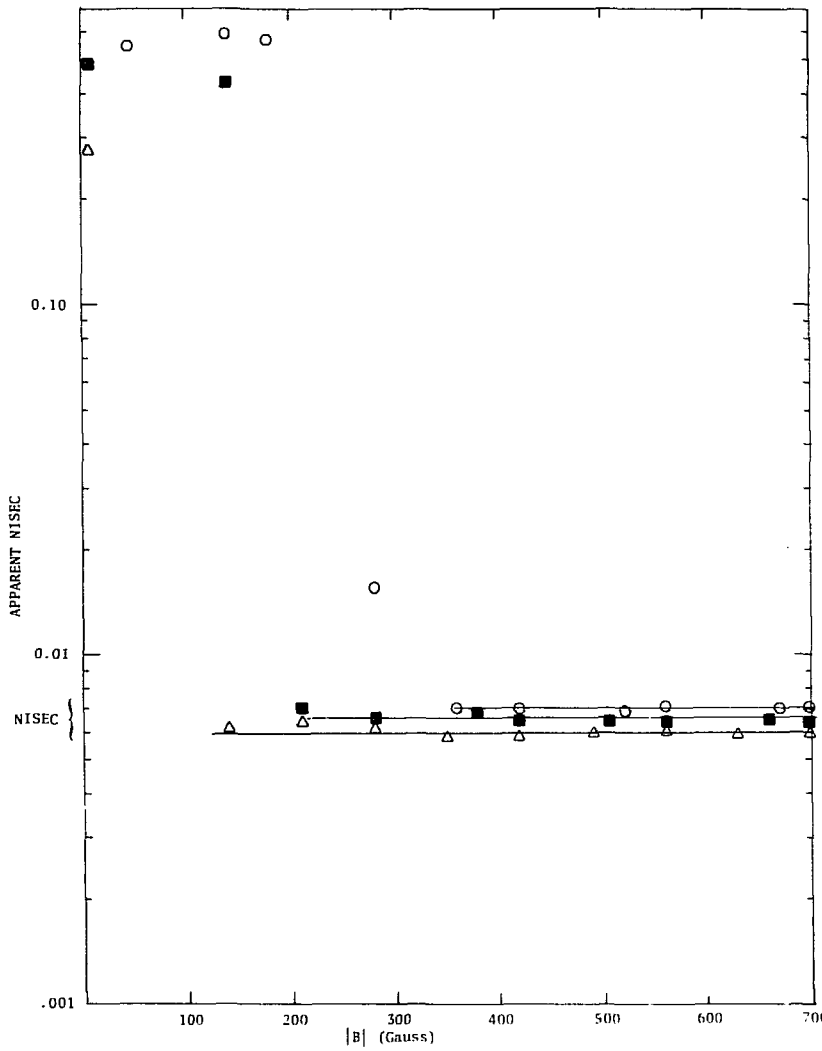

XBL 803-8612

Figure 19. The apparent NISEC vs the magnitude of the magnetic field used to suppress secondary electrons for D_3^+ incident on an untreated molybdenum target. Incident energy = 1 keV/nucleus, $|\bar{E}_{gap}|$ = 0.9 kV/cm-- △ , incident energy = 2.5 keV/nucleus, $|\bar{E}_{gap}|$ = 2.3 kV/cm-- ■ , incident energy = 4 keV/nucleus, $|\bar{E}_{gap}|$= 3.6 kV/cm-- O .

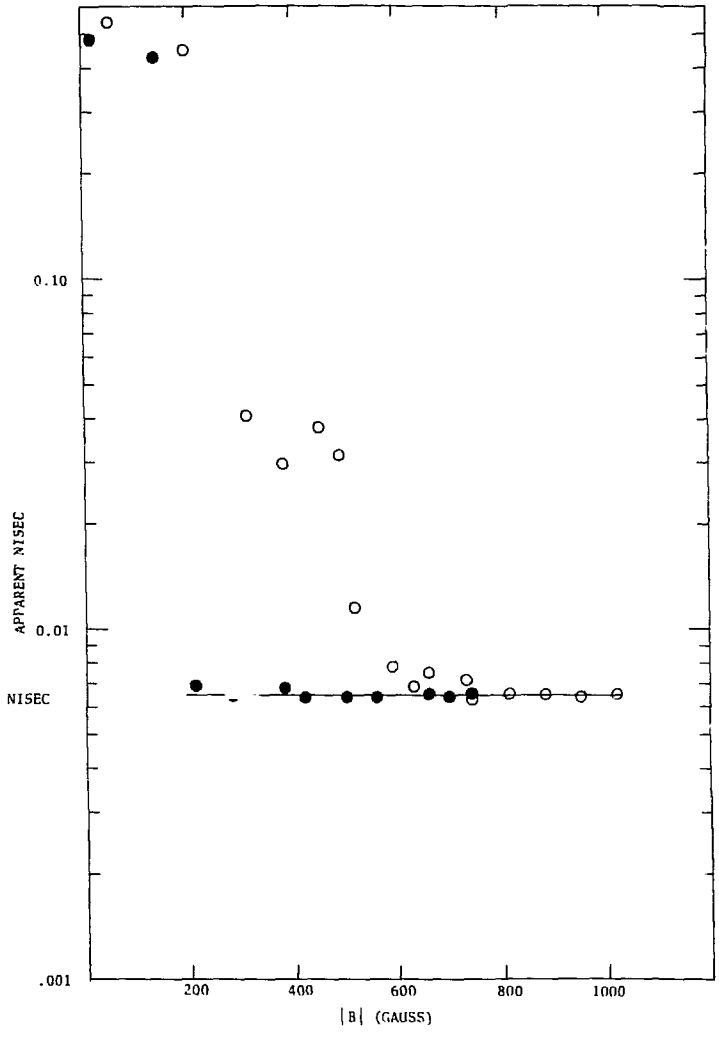

XBL 803-8611

Figure 20. Apparent NISEC vs the magnitude of the magnetic field for suppression of electrons for 2.5 keV/nucleus D_3^+ on untreated molybdenum, and two positions of the apparatus in the magnetic field: collector-target gap centered in the field— ●, and collector-target gap moved 1.6 cm toward the edge of the field— O.

measured at the Hall probe at the face of one of the poles) was required to suppress the electrons when the collector-target gap was moved to the edge of the magnet poles. This concluded the investigation to determine the dimensions and operating parameters of the apparatus. The next step was to measure the NISEC for thick alkali-metal targets.

B. Thick Targets

NISEC measurements were made using thick alkali-metal targets before thin targets because the procedure for establishing thick targets is much simpler. A thick target is established whenever the alkali-metal layer is so thick that the measured NISEC is due to particles interacting with the alkali-metal layer, and not with the substrate. A thick target is established by measuring the NISEC between successive evaporations of the alkali-metal until the NISEC no longer changes as more alkali-metal is deposited (see figure 21). However, if only one substrate is used, the NISEC may also remain constant as more alkali-metal is evaporated from the dispensor because an equilibrium thickness has been reached, i.e., the rate of evaporation of the alkali-metal from the target surface is high enough that competition between the incident flux and evaporation prevents the alkali-metal layer from becomming thicker. If a second substrate is used and the above procedure repeated, a thick target will give the same values for the NISEC for both substrates, whereas an equilibrium target give different values for the NISEC because of the different reflectivities of the two substrates Therefore, Cu and Ta substrates were used for the thick alkali-metal target measurements. Cu and Ta were used because of the large difference in nuclear charge (29 for Cu vs 73 for Ta) and in mass (63.5

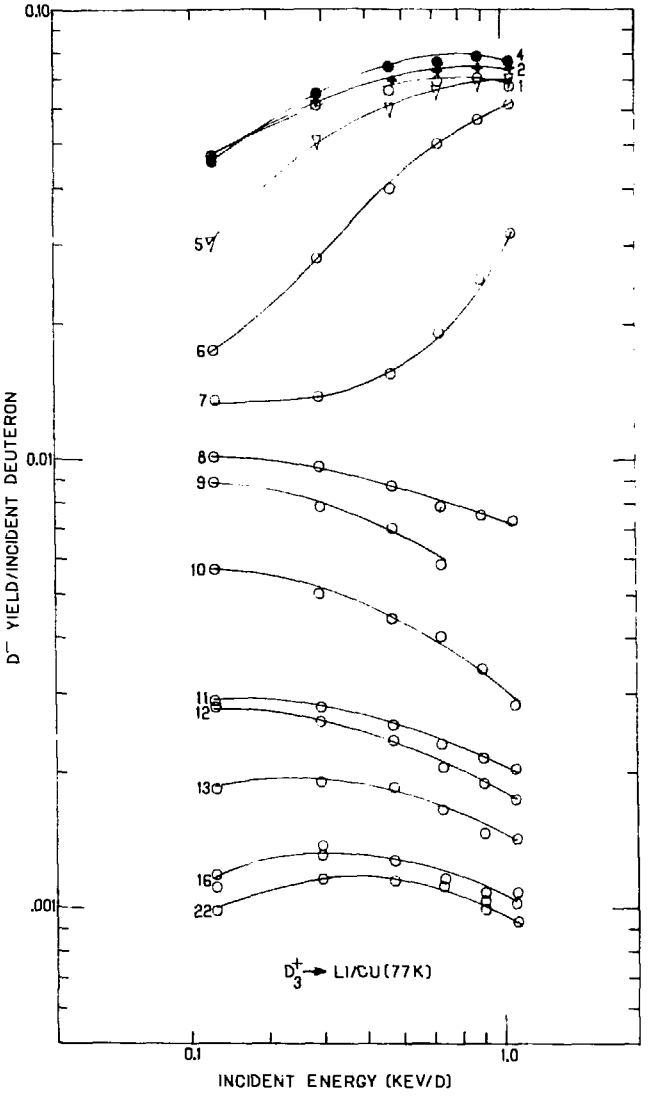

XBL 7910-12619

Figure 21. NISEC vs incident energy for D_3^+ incident on Li deposited upon a Cu substrate cooled by liquid nitrogen. The numbers by each curve correspond to the Li evaporation number and indicate increasing thickness of the Li deposit.

for Cu vs 180.9 for Ta), which should give rise to significant differences in the reflected fraction of the incident beam.[31] The procedure for measuring the NISEC from a thick sodium target is presented below as an example of the technique for obtaining the NISEC measurements for thick alkali-metal targets.

The liquid nitrogen cooled target was used for all thick target NISEC measurements. This target provided a copper substrate, which was cleaned by abrasion and washed with water. Two S.A.E.S. sodium dispensors were spot-welded together at one end and onto support rods at the other end, and were installed in the experimental chamber. The end flange, on which the target structure was mounted, was bolted into place to seal against a copper gasket. The chamber was then evacuated according to the procedure outlined in Chapter III.

The sodium dispensors were outgassed in the retracted position, by passing 6.5 Amps through them for 4 minutes and then 7.5 Amps for 1 minute. During outgassing, the pressure in the chamber reached 1×10^{-7} Torr, but quickly dropped back to less than 1×10^{-9} Torr.

At this time the target cooling was turned on and allowed to run for 5 minutes. An 8.0 keV beam of Ar^+ was tuned onto the target and the quadrupole mass analyzer was used to scan the positive and negative ions leaving the target surface.

After the mass scan, the accelerator gas was changed to deuterium and a 0.9 keV beam of D_3^+ was tuned onto the target (the beam current was about 1×10^{-9} Amps). The NISEC was measured for the bare copper substrate with target biases of -0.4, -1.4, -2.4, -3.5, and -4.4 kV. The sodium dispensors were moved into position and sodium was

evaporated at a current of 7.5 Amps for 45 seconds. The NISEC measurements were repeated, and then more sodium was evaporated. This procedure was repeated until the NISEC values remained constant as more sodium was deposited (six evaporations). The beam energy was then varied to measure the NISEC for incident energies of 0.2 to 4.0 kev/nucleus, and for D_2^+ as well as D_3^+. Once the NISEC measurements with deuterium were completed, the accelerator gas was changed back to argon, and a 4.0 keV beam of Ar^+ was tuned onto the target (the current was about 3×10^{-8} Amps). The target was biased as -4 kV to give a NISEC corresponding to 8 keV Ar^+ incident. The argon measurement was used to determine the contribution of sputtered (as opposed to backscattered) negative ions to the NISEC, and running the accelerator on argon between running on deuterium and hydrogen prevented cross-contamination of these isotopes. After the NISEC measurement with argon, an 8.0 keV beam was used to repeat the positive and negative ion mass scans.

At this time, the cryopump was heated overnight to drive off the liquid nitrogen and liquid helium. The experimental chamber was then filled with dry nitrogen gas and opened. A tantalum plate was attached to the copper target with two screws and the used sodium dispensors were replaced with new ones. The chamber was closed and the above process was repeated to establish a thick sodium target and obtain NISEC measurements. Ar^+ was used again for NISEC measurements, and then the accelerator gas was changed to hydrogen. To complete the NISEC measurements for a sodium target, H_2^+ and H_3^+ were used over the same incident energy range as deuterium.

After completion of the sodium measurements, potassium, rubidium, cesium and lithium were also used as targets, before measurements from thin targets were undertaken.

C. Thin Targets

The first measurements of the NISEC for thin alkali-metal coverage were made using a heatable copper target. The copper target was chosen because within the limits of the heating system, (temperatures less than 1400K), the copper could be heated to a high enough temperature to evaporate the target material and thus give a repeatable surface for a reference work function measurement. The procedure for measuring the NISEC for sodium deposited on the copper substrate is presented below as an example of the technique used.

An oxygen-free copper target and the sodium dispensore were installed and the chamber was pumped down to a base pressure of 1×10^{-10} Torr, as previously described. The copper target was heated to about 1250K for one hour. By looking at the collector plate through an observation port, I could see it change color from steel gray to copper as the copper was evaporated from the front of the target and deposited on the collector. After one hour, the heating was turned off and the target was allowed to cool overnight.

The current-voltage (I-V) curve of the work function diode was recorded using the copper surface as the collector (see Appendix B). Then, a 1.0 keV beam of H_3^+ was tuned onto the target surface and then detuned to an intensity of 2×10^{-10} Amps to minimize the sputtering of the target surface due to the beam. NISEC measurements

were made for target biases of : -0.3, -0.6, -09., 1.2, -1.5 and -1.8 kV. The I-V curve was measured and then sodium was evaporated with a dispensor current of 8.0 Amps for 25 seconds. Another I-V curve was recorded and the NISEC was measured for each of the above biases. After the NISEC measurements, another I-V curve was recorded to measure any change in the work function resulting from these measurements. More sodium was evaporated, and this procedure was repeated after each evaporation for a total of fourteen evaporations. Upon completion of this set of NISEC measurements, the target was again heated to 1250K to drive off the Na and evaporate more copper. After the target cooled over-night, the above procedure was reported. The maximum NISEC values decreased with successive sets of measurements and when the copper target was taken out and examined, there was obvious growth of the crystal grains in the copper. Most of the grains were larger than the beam diameter, so that it's possible that during the course of heating, the area of the copper target seen by the beam changed from amorphous to single crystal or polycrystaline, with a corresponding decrease in reflectively,[21] which would explain the decrease in the NISEC values.

Since reproducible NISEC measurements could not be obtained with the heated target, and since a cooled target would allow deposition of thick alkali metal coverages, useful for referencing the work function measurements, all of the NISEC measurements for thin alkali-metal coverage were made using the liquid-nitrogen-cooled target. Rectangular plates with the same dimensions as the collector were bolted onto a cooled copper disk to serve as the substrate for alkali-metal deposition. The plates were cleaned by abrasion and washed with water before entering

the vacuum chamber. The procedure for the NISEC measurements was the same as outlined above, but the work function measurements could no longer be normalized to the bare substrate since this could not be cleaned in situ. Therefore, the NISEC measurements were carried out until the values for thick alkali-metal coverage were obtained and at this point the work function was assigned the value of the thick alkali metal.

Measurements were made for Cs on Ni, Cu, Mo and W and for Li on Cu and W and for Na on Cu.

CHAPTER V

RESULTS AND DISCUSSION

A. Thick Targets

Figures 22 through 31 show the measured values of the NISEC for Cs, Rb, K, Na and Li targets bombarded by hydrogen and deuterium ions, as a function of the incident energy of the ions. The estimated uncertainties (±10 percent) indicated in the figures are discussed in Appendix D.

The identity of the collected negative ions could not be determined directly: the quadrupole mass analyzer showed serval mass peaks corresponding to negative ions other than H^- or D^- leaving the target surfaces (see Appendix A). In Appendix E, arguments are given which lead to the conclusion that the measured NISEC is actually due to reflected particles and that the sputtered negative ions including H^- and D^-, contribute at most a few percent of the NISEC.

There are several features worth noting in Figures 22 through 31:

(1) All targets show a maximum in the NISEC vs incident energy, for both H and D incident.

(2) The higher the maximum value of the NISEC, the lower the incident energy at which it occurs.

(3) The value of the NISEC decreases in the order: Cs, Rb, K, Na and Li at any given incident energy.

(4) The ordering of the alkali metals given in (3) is according to increasing work function and decreasing target mass and atomic number.

Figure 22. NISEC vs incident energy per proton for H_2^+ -- ● and H_3^+ -- O , bombarding a cesium target. X -- results of NISEC least squares fit described in Chapter V, part C. The NISEC's were obtained using Eq. (3) of Chapter V, with $\alpha = 0.387$ and $\beta = 0.479$.

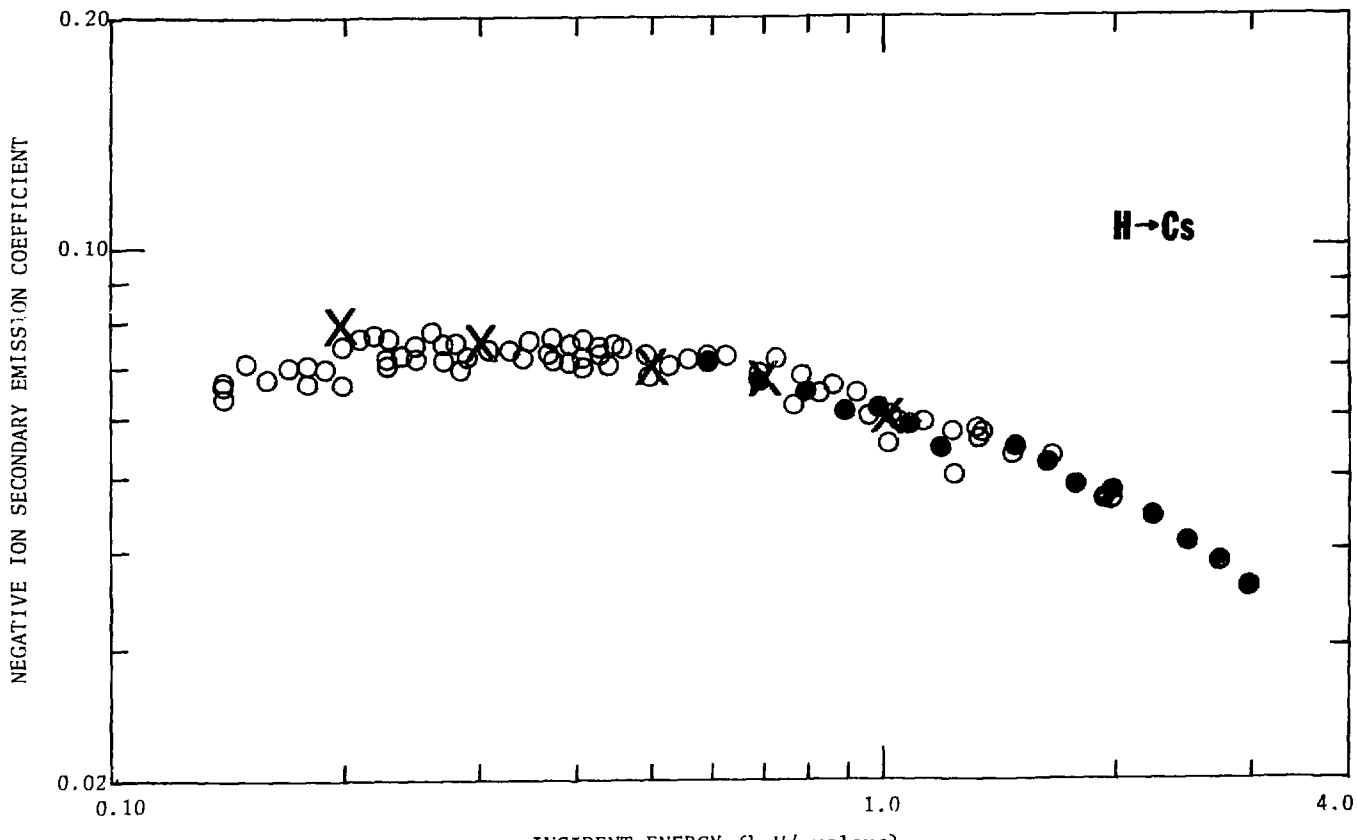

XBL 794-9350

Figure 22.

Figure 23. NISEC vs incident energy per deuteron, for D_2^+ -- ● and D_3^+ -- O , bombarding a cesium target. X -- results of NISEC least squares fit, with α = 0.387 and β = 0.479.

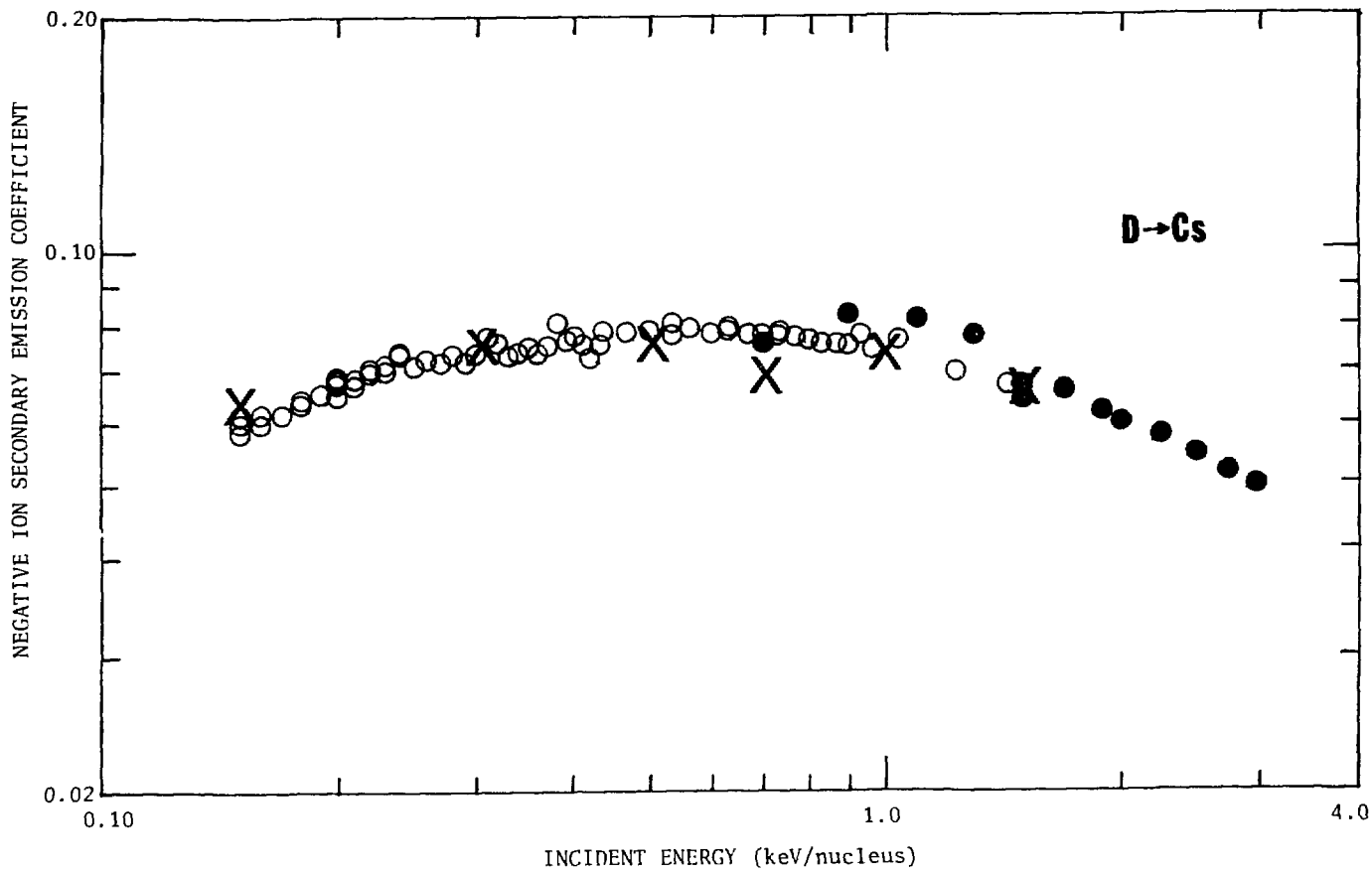

XBL 794-9349

Figure 23.

Figure 24. NISEC vs incident energy per proton, for H_2^+ -- ● and H_3^+ -- O bombarding a rubidium target. X -- results of NISEC least squares fit, with $\alpha = 0.434$ and $\beta = 0.578$.

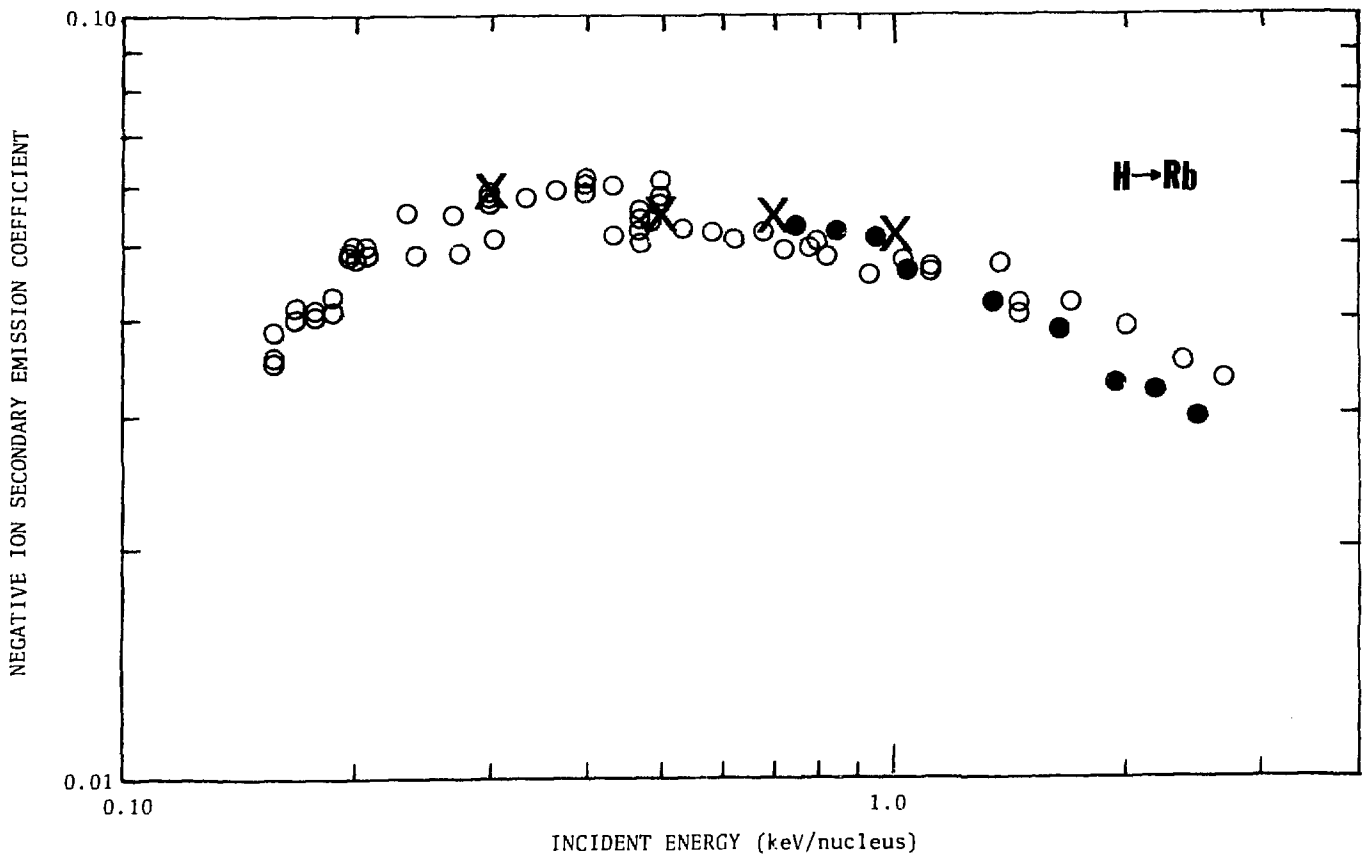

XBL 795-9717

Figure 24.

Figure 25. NISEC vs incident energy per deuteron, for D_2^+ -- ● and D_3^+ -- O bombarding a rubidium target. X -- results of NISEC least squares fit, with $\alpha = 0.434$ and $\beta = 0.578$.

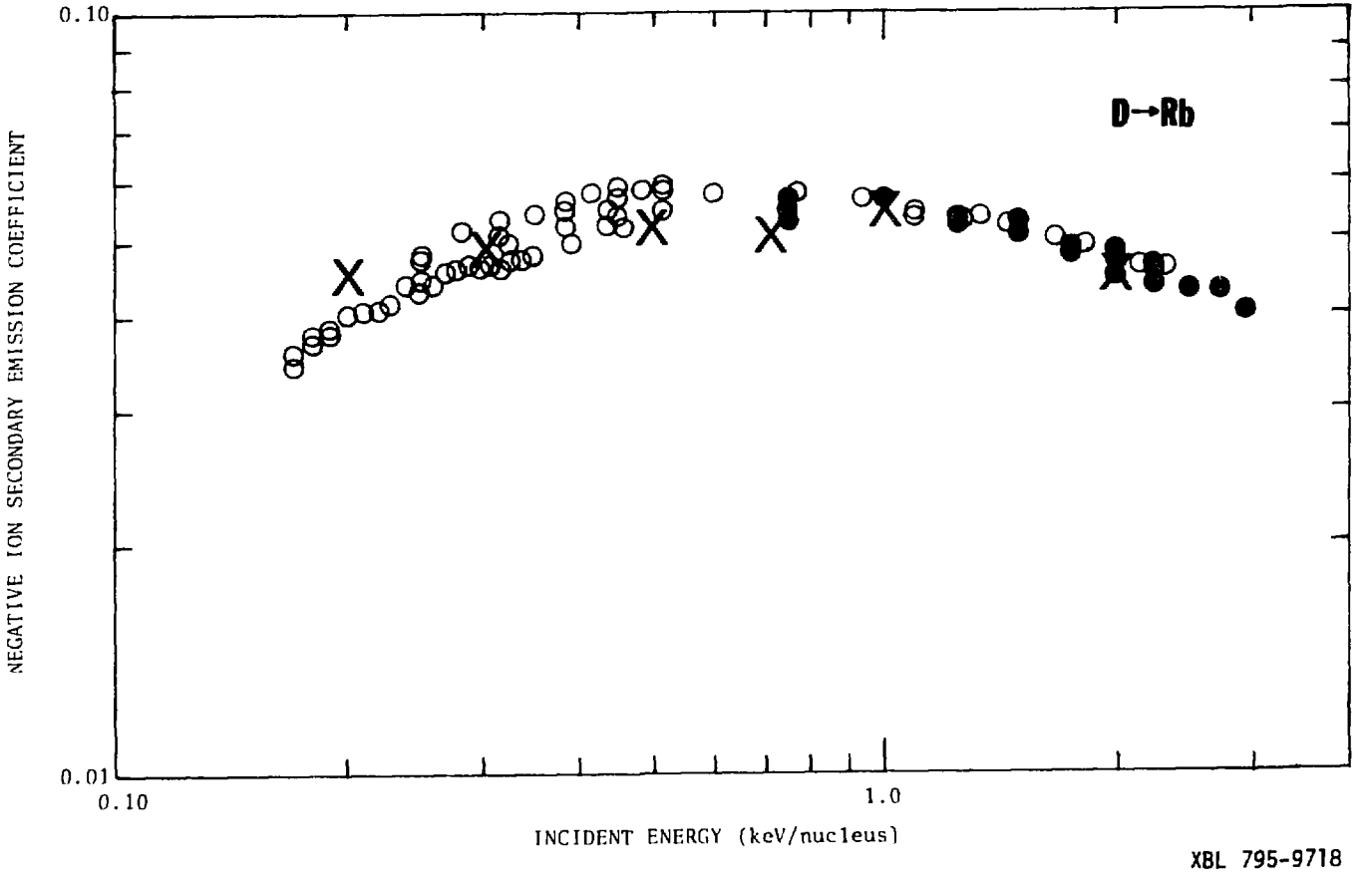
0.10
0.01
0.10
1.0
NEGATIVE ION SECONDARY EMISSION COEFFICIENT
INCIDENT ENERGY (keV/nucleus)
D→Rb
XBL 795-9718

Figure 25.

Figure 26. NISEC vs incident energy per proton, for H_2^+ -- ● and H_3^+ -- o bombarding a potassium target. X -- results of NISEC least squares fit with $\alpha = 0.50$ and $\beta = 0.65$.

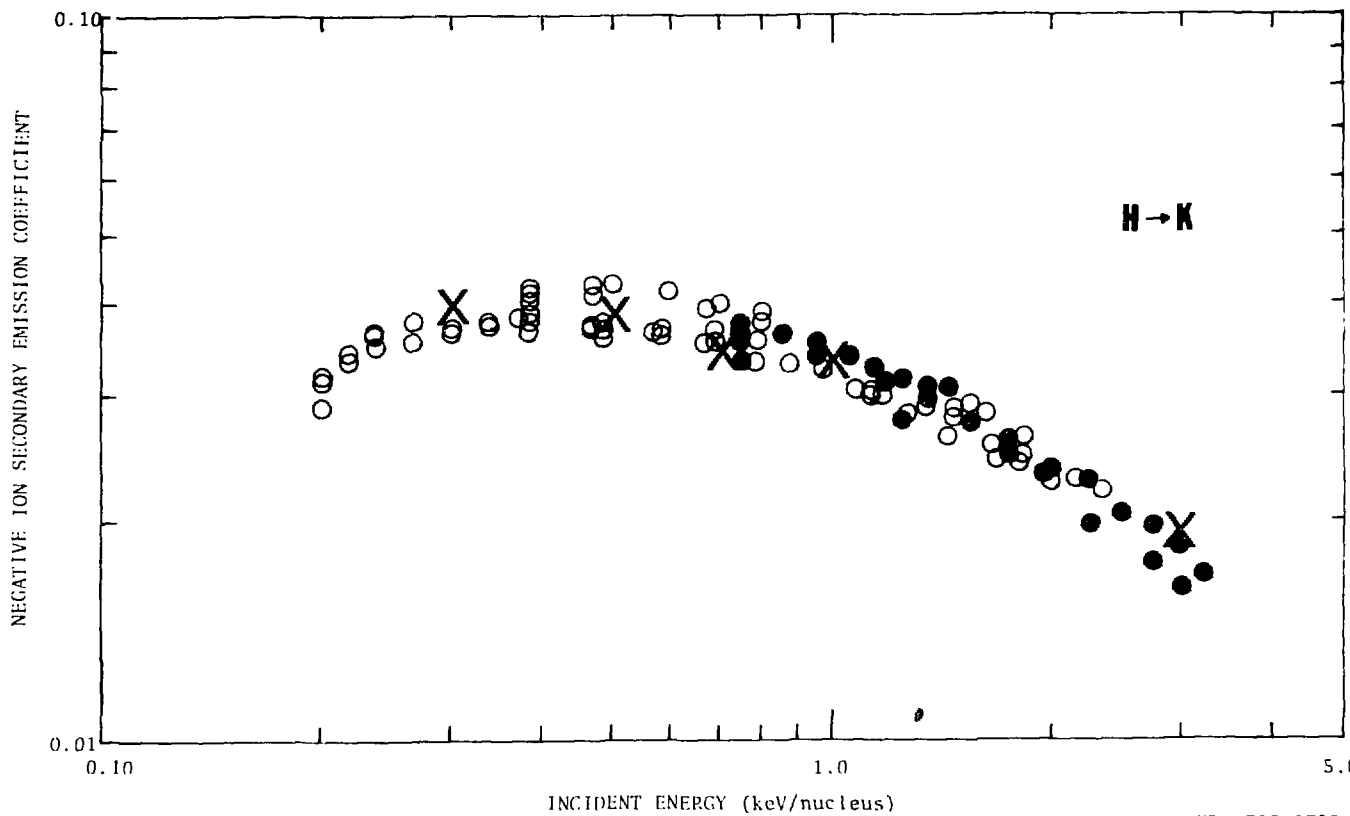

XBL 795-9715

Figure 26.

Figure 27. NISEC vs incident energy per deuteron for D_2^+ -- ● and D_3^+ -- o bombarding a potassium target. X -- results of NISEC least squares fit, with $\alpha = 0.50$ and $\beta = 0.65$.

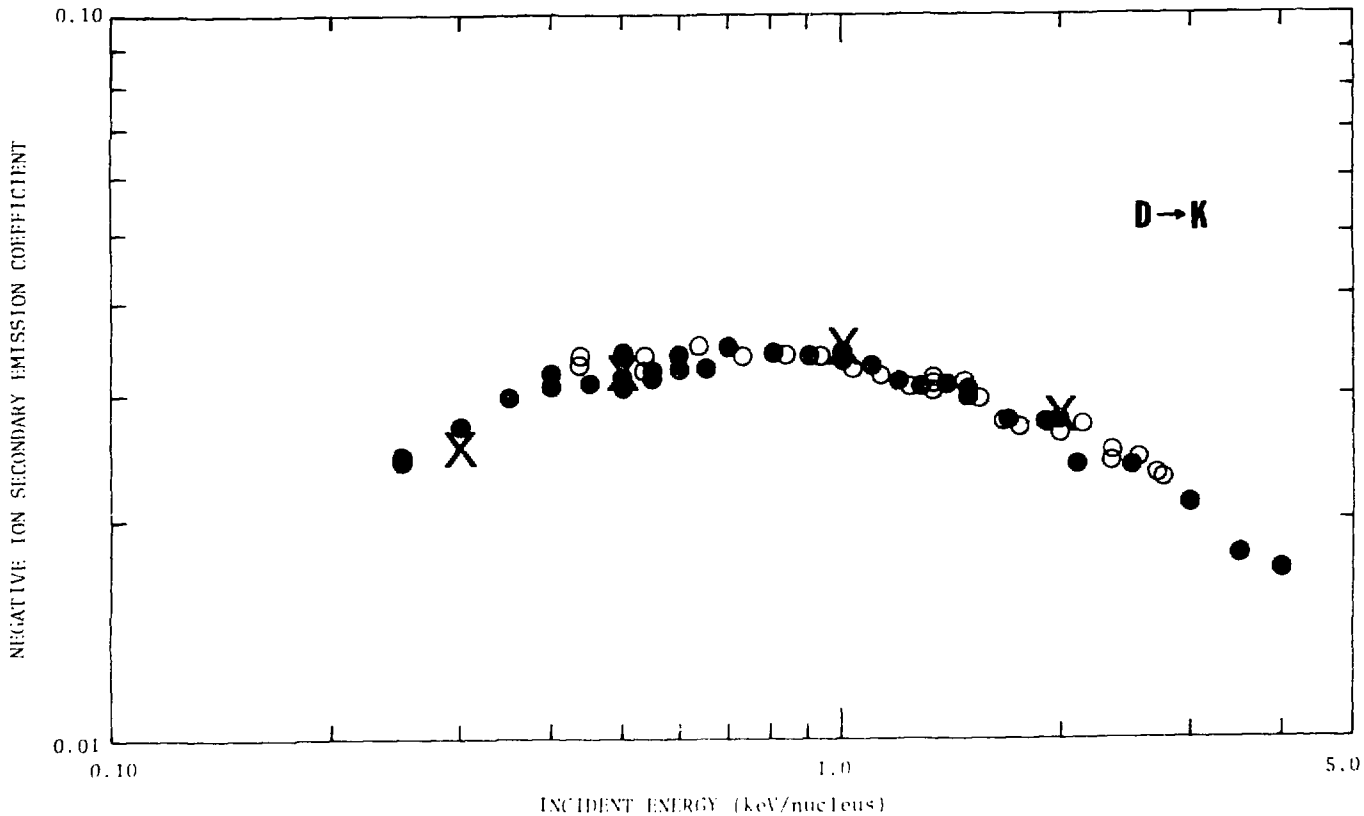

XBL 795-9716

Figure 27.

Figure 28. NISEC vs incident energy per proton for H_2^+ -- ● and H_3^+ -- ○ bombarding a sodium target. X -- results of NISEC least squares fit, with $\alpha = 0.940$ and $\beta = 0.944$.

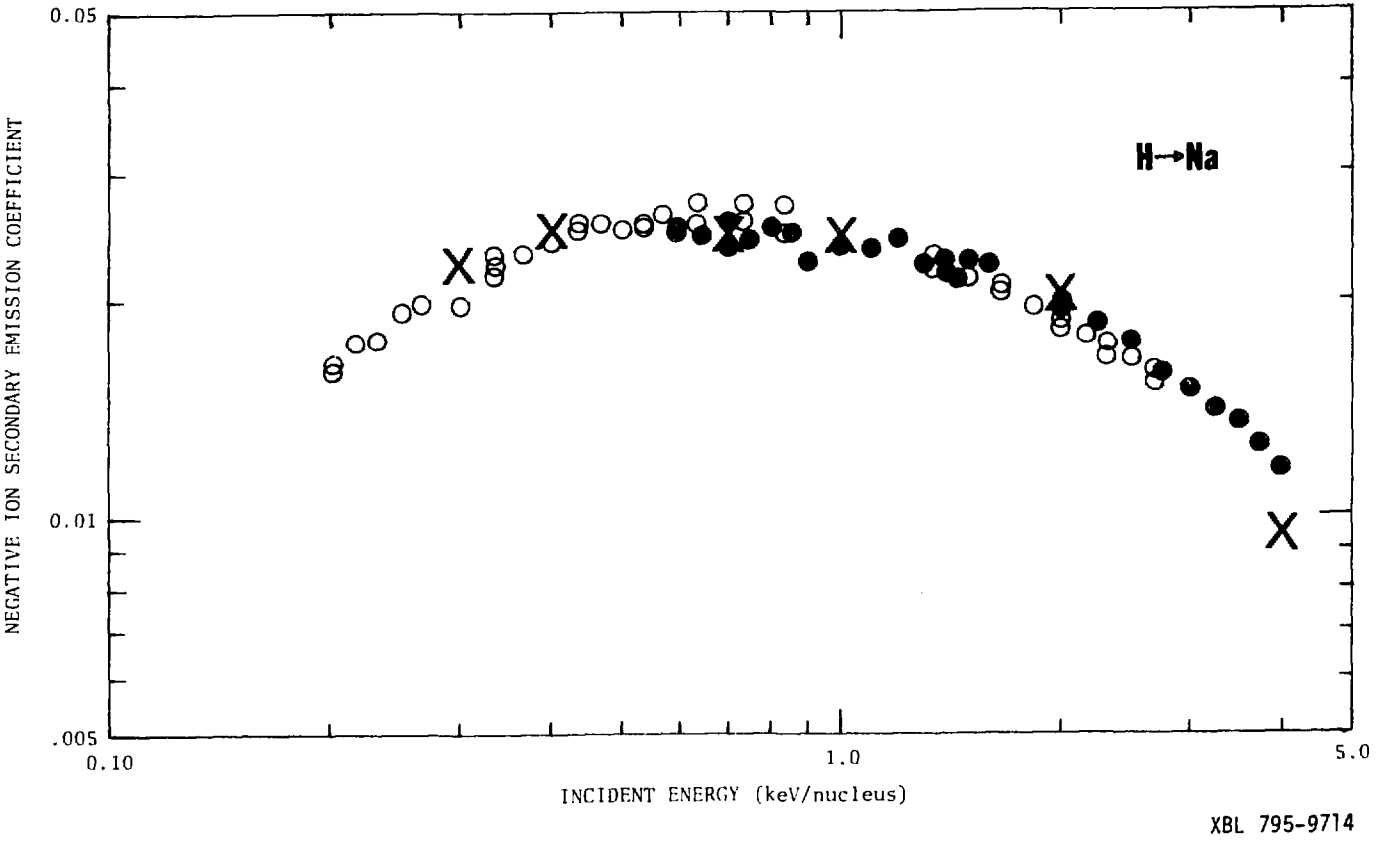
0.05
0.01
.005
0.10
1.0
5.0
NEGATIVE ION SECONDARY EMISSION COEFFICIENT
INCIDENT ENERGY (keV/nucleus)
H→Na
XBL 795-9714

Figure 28.

Figure 29. NISEC vs incident energy per deuteron for D_2^+ -- ● and D_3^+ -- O bombarding a sodium target. X -- results of NISEC least squares fit, with α = 0.940 and β = 0.944.

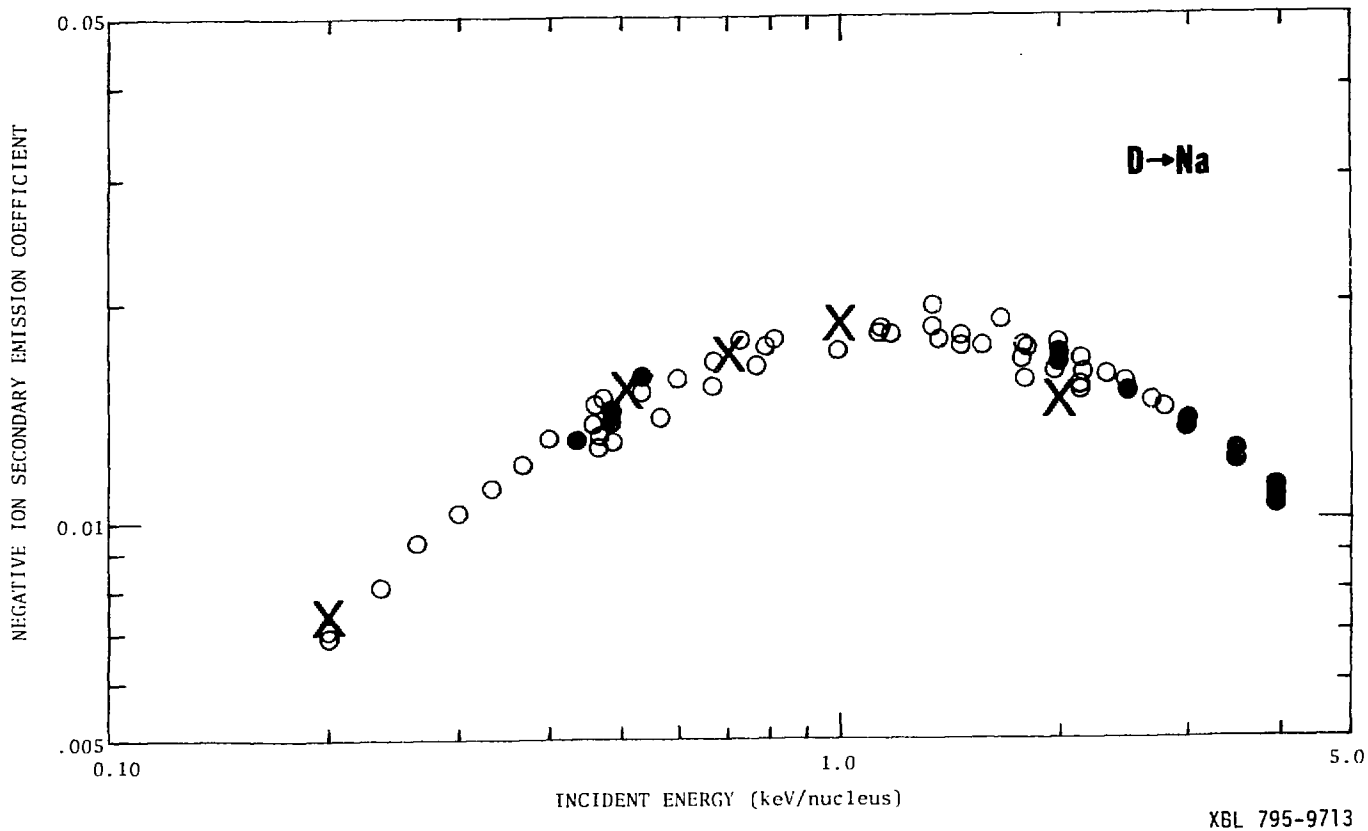
0.05
0.01
.005
0.10
1.0
5.0
NEGATIVE ION SECONDARY EMISSION COEFFICIENT
INCIDENT ENERGY (keV/nucleus)
D→Na
XBL 795-9713

Figure 29.

Figure 30. NISEC vs incident energy per proton for H_2^+ -- ● and H_3^+ -- O bombarding a lithium target. X -- results of NISEC least squares fit, with $\alpha = 0.332$ and $\beta = 0.966$.

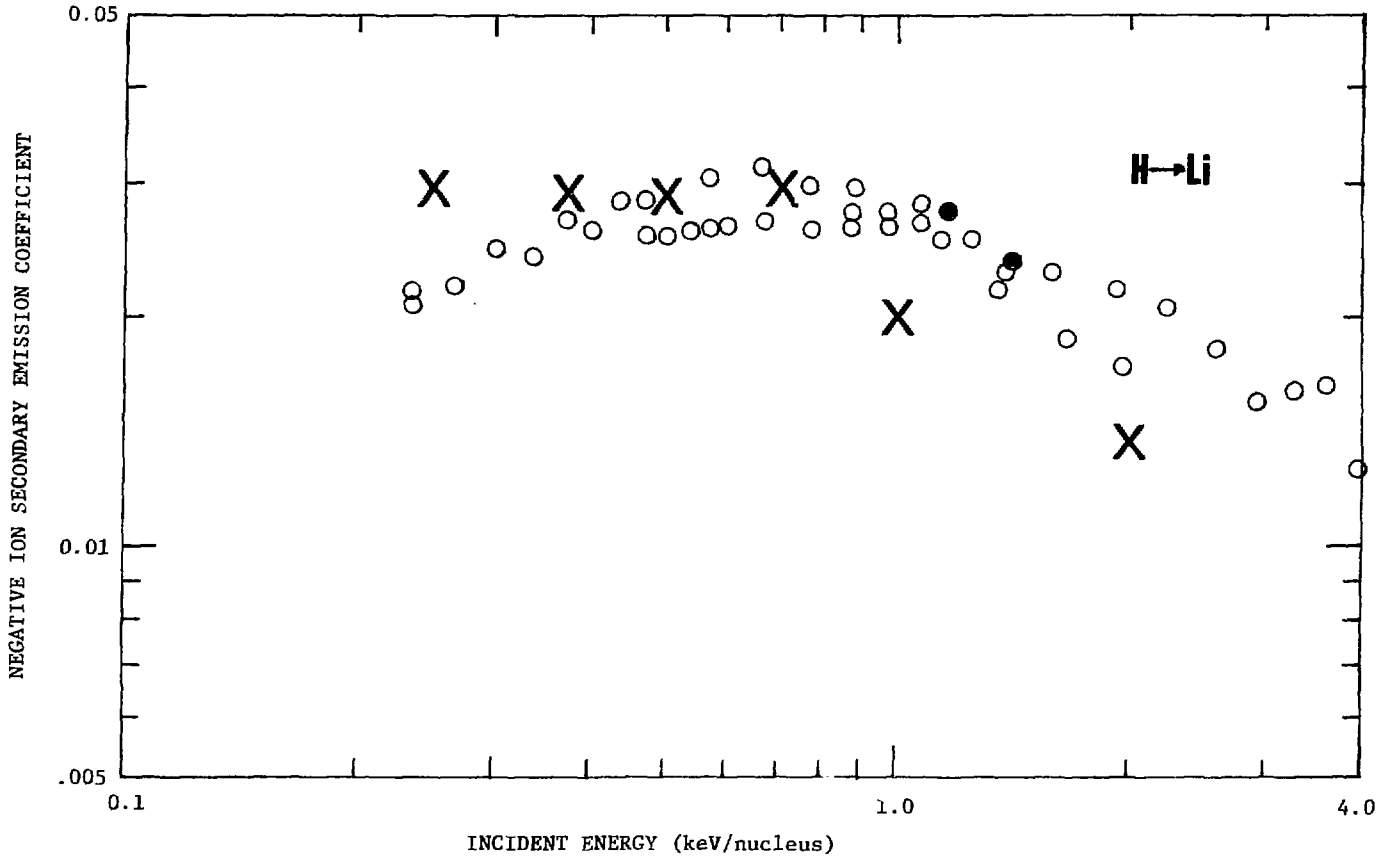

XBL 795-9711

Figure 30.

Figure 31. NISEC vs incident energy per deuteron for D_2^+ -- ● and D_3^+ -- O bombarding a lithium target. X -- results of NISEC least squares fit with $\alpha = 0.322$ and $\beta = 0.966$.

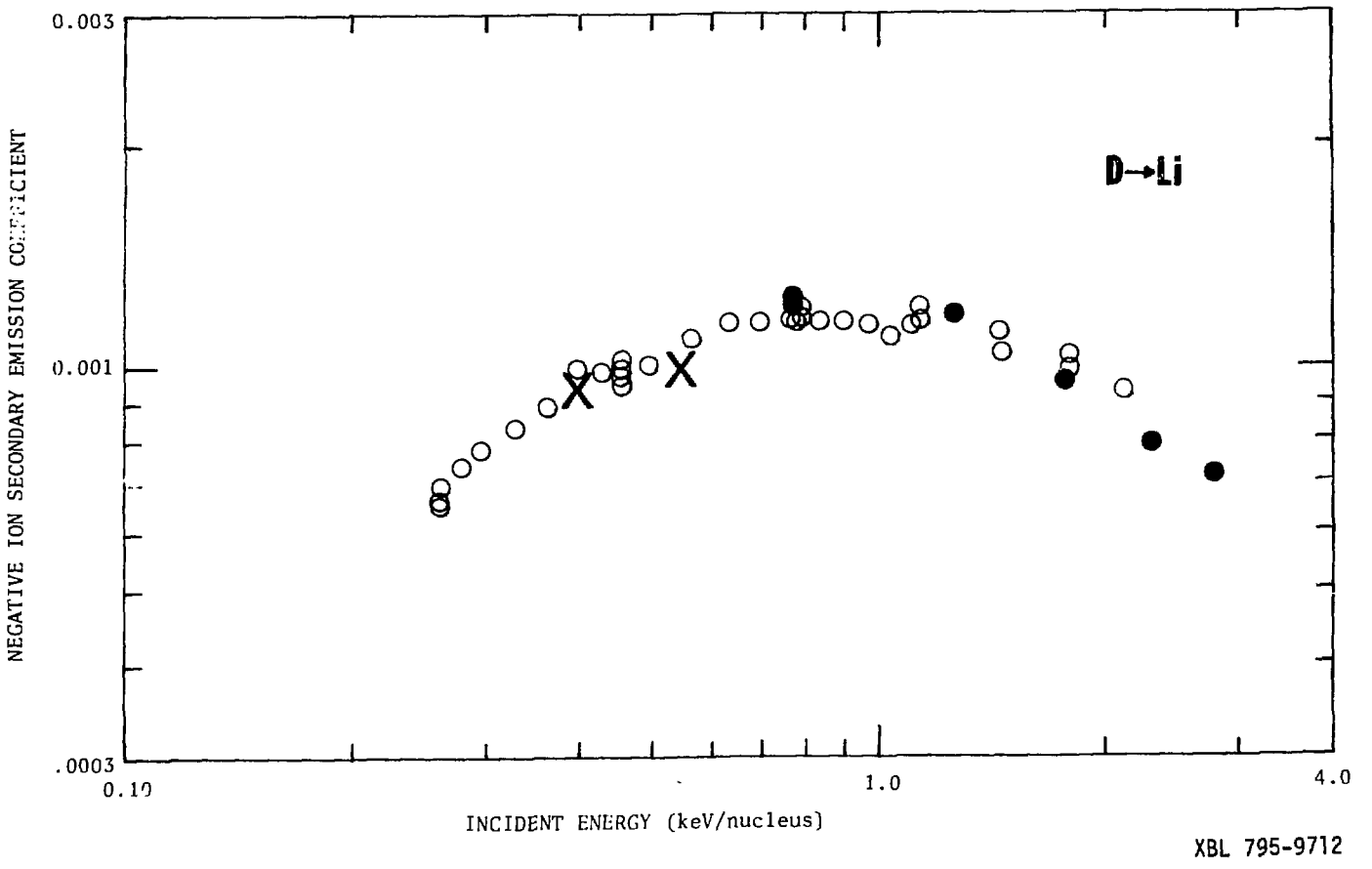
0.003
0.001
.0003
0.10
1.0
4.0
NEGATIVE ION SECONDARY EMISSION COEFFICIENT
INCIDENT ENERGY (keV/nucleus)
D→Li
XBL 795-9712

Figure 31.

(5) The NISEC for a given target is the same for different molecular ions of the same isotope (i.e, D_2^+ and D_3^+ or H_2^+ and H_3^+), but not for the different isotopes (i.e, H vs D).

(6) The isotope effect of the NISEC becomes more pronounced in going from one target to another in the same order given in (3).

(7) The NISEC for both H and D on Li is significantly lower than for the other four targets.

For discussion of points (1) through (7), we shall attempt a qualitative understanding of H^- formation at surfaces: Let us consider the processes described in Chapter II. For a given exit velocity, the NISEC is the product of a formation probability, (P_-), and a survival probability (f), and the number of particles emerging at that velocity, (n(v)), normalized to the number of incident nucleii, (N_i). The NISEC is given by equation (9) of Chapter II:

$$\text{NISEC} = \frac{1}{N_i} \int_{\bar{v}} n(\bar{v})\left(1 - e^{-\frac{1}{v_\perp}\int_0^{x_0} P(x)dx}\right)\left(e^{-\frac{1}{v_\perp}\int_{x_0}^{\infty} Q(x)dx}\right)d\bar{v}$$

For the sake of discussion, we assume that the terms are separable:

$$\text{NISEC} = R_N f P_- \tag{1}$$

where,

R_N is the total particle reflection coefficient

P_- is the (velocity averaged) probability of H^- formation

f is the (velocity averaged) probability of H^- survival

To discuss the NISEC measurements in terms of equation (1), we need to know the dependences of R_N, f and P_- on the incident energy. Using the Marlowe[31] code, Hiskes[21] has shown that for H incident upon the alkali metals on the energy range of these measurements, R_N is monotonically decreasing function of the incident energy. A similar result is true for D incident (see table 2).

From its functional form, it is clear that P_- is a monotonically decreasing function of the perpendicular exit velocity of the particle, which in turn decreases with decreasing incident velocity. Similarily, f is a monotonically increasing function of the incident velocity. Therefore, the fact that all of the NISEC curves have a maximum (1) at incident energies of a few hundred electron Volts indicates that the NISEC is strongly influenced by the survival probability at incident energies below a few hundred electron Volts. This is true because the survival probability is the only one of the three factors, in equation (1) which decreases with decreasing energy. Similarly, at high incident energies the probabilities of formation and reflection dominate the NISEC.

Features (2) and (3) above can be explained by considering the significance of (4): As the target mass and atomic number decrease, the probability or reflection decreases.[21] Also, the lower the work function, the larger the survival probability at lower incident energies, thus shifting the maximum in the NISEC to lower incident energy.

The isotope effect (5), arises from the fact that R_N, f and P_- have different energy dependences: R_N depends upon the incident energy, while f and P_- depend upon the incident velocity. In most cases, R_N is almost the same for H and D incident at the same incident energy, but the average reflected velocity will be higher for H than for D. At low incident energies, where the survival probability dominates, H will have a higher survival probability than D, and thus a higher NISEC than D. On the other hand, at high incident energies, where formation probability dominates, D will have a higher formation probability than H and thus a higher NISEC. This argument also explains the crossing over of the H and D NISEC curves.

The fact that the isotope effect becomes more pronounced as the target mass and atomic number become smaller is due to the mass difference between H and D (1 a.m.u.) becoming more significant compared to the target mass (133 a.m.u. for Cs to 7 a.m.u. for Li), thus giving rise to different velocity distributions and reflected fractions of H and D leaving the target.

Finally, the very low value of the NISEC from Li can be explained by the low probability of reflection from Li[21] as calculated by Marlowe:[31] The reflection from Li is almost an order of magnitude lower than for Na (the alkali metal with the next lowest reflectivity). Also, the velocity distribution of the reflected particles is peaked at the low energy end of the distribution, so that higher incident energies are required for the reflected particles to have the optimum exit velocity for negative ion production. However, as the incident energy is increased, the reflected fraction drops rapidly (from Table 2,

R_N=0.064 for 250 eV/proton incident energy to 0.026 for 1000 eV/proton incident energy), so that the NISEC will always be much smaller for Li than for the other alkali metals.

B. Thin Targets

Figure 32 shows the NISEC and work function measurements as a function of Na evaporation number as the Na is deposited on a Cu substrate which was cleaned by heating in the vacuum chamber. The work function measurements were normalized to the value for thick Na (2.3 eV)[40] which then gave a value of 4.2 eV for the bare Cu surface, compared with 4.5 eV from the literature.[40] From Figure 32 it is clear that the work function goes through a minimum value, which is less than the value for thick Na. Work function minima for various alkali-metal coverages of transition metal substrates have been reported in the literature,[41,42,43] so this result is not surprising. The NISEC goes through a maximum value, corresponding to the work function minimum, but even when the work function has increased again to the value for thick Na, the NISEC is still higher than that for thick Na (0.040 vs 0.024). The higher NISEC is probably due to enhanced reflection from the Cu substrate. In fact, if we compare the NISEC values corresponding to a work function of 2.3 eV on either side of the work function minimum, we see that they are the same, indicating that the increase in Na thickness in going through the work function minimim is not enough to change the backscattered distribution from the Cu substrate. Typically, only one atomic layer of alkali metal is required on a clean substrate to establish a work function corresponding to that of the alkali metal.[41,42,43]

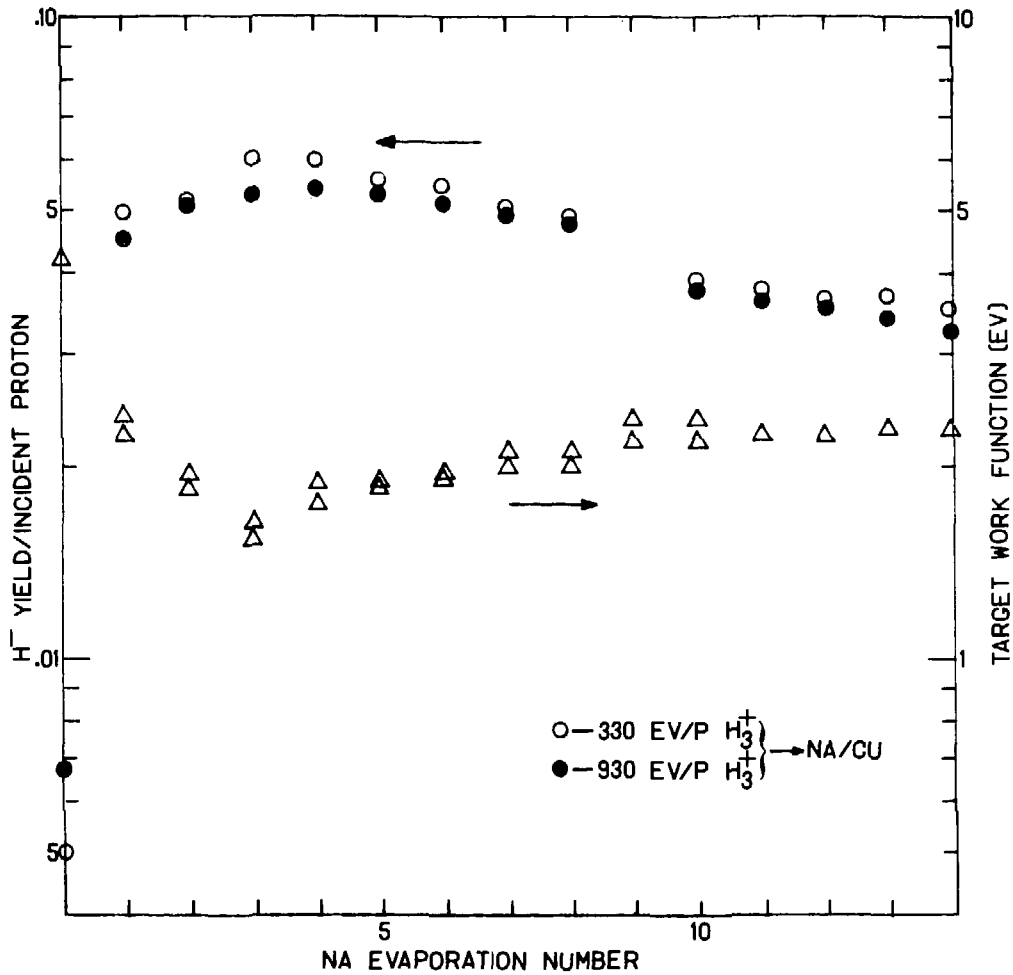

XBL 7911-12683

Figure 32. Surface work function-- △, and NISEC for 330 eV/p- ○, and 930 eV/p-- ●, H_3^+ vs evaporation number (Na thickness in arbitrary units) for Na deposited on a Cu substrate at ambient temperature (300 K).

Figures 33 and 34 show NISEC and work function measurements for Li coverage of Cu and W substrates at liquid nitrogen temperature (77K). In both cases, there is a minimum in the work function, but for Li on Cu, the maximum in the NISEC does not correspond to the work function minimum. Also, if we compare the work function corresponding to thick Li (2.5 eV), on either side of the work function minimum, we see that the NISEC to the right of the minimum is much lower than the one to the left for both substrates. These results can be explained if the Li layer is thick enough to affect the backscattered distribution and reflected fraction of the incident ions: As the Li coverage is increased, the gain in the H^- production due to decreased work function is nullified by the loss in the number of particles leaving the target due to decreased reflection from Li. From the Marlowe[31] code, the average range for protons in Li at the energies of this experiment is hundreds of atomic layers, therefore, coverage thick enough to affect the backscattered distribution and reflected fractions would have to be tens of atomic layers thick. Since it generally only takes one atomic layer to establish a thick alkali-metal work function on a clean substrate, these Li results indicate that the substrate was not clean and that possibly a complex surface of Li and impurity oxygen was produced. Complex surfaces of Cs_2O_2 can be hundreds of atomic layers thick before the minimum work function is reached and this minimum is lower than that of thin Cs on a clean substrate.[45]

The maximum value of the NISEC for Li on Cu is about 0.12 while the maximum for Li on W is only 0.08. Based upon reflectivity arguments, we would expect the Li on W target to give a higher NISEC. That this is

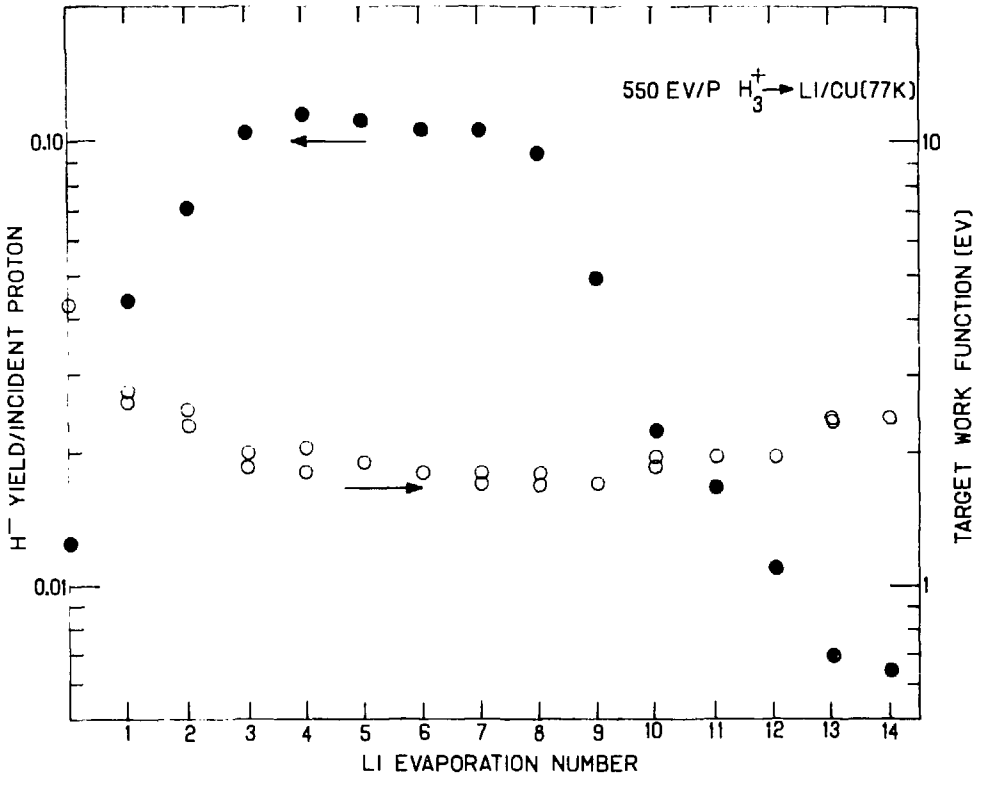

XBL 791C-12620

Figure 33. Surface work function-- ○, and NISEC for 550 eV/p-- ●, H_3^+ incident vs evaporation number for Li deposited on a Cu substrate cooled by liquid nitrogen (T~77 k).

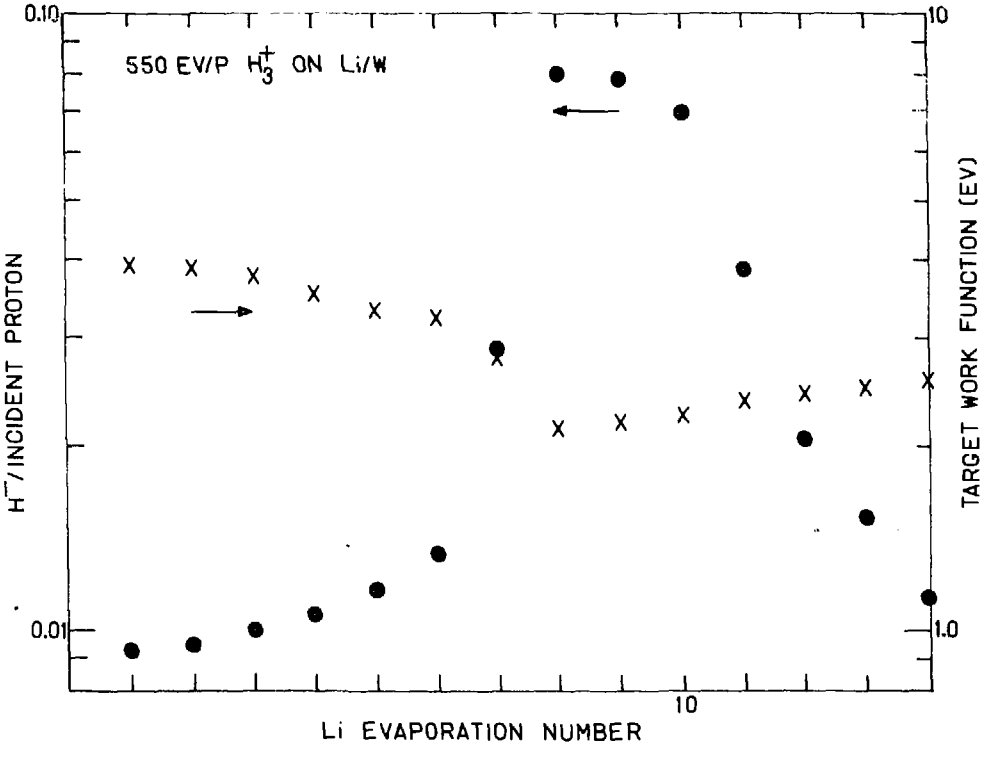

XBL 7910-12271

Figure 34. Surface work function-- X and NISEC for 550 eV/p-- ● H_3^+ incident vs evaporation number for Li deposited on a W substrate cooled by liquid nitrogen.

not the case may be due to the different work functions for Li on Cu (1.7 eV) and Li on W (2.0 eV) or there may also be an effect due to different Li thicknesses corresponding to the work function minima.

NISEC and work function measurements for Cs coverage of liquid nitrogen cooled Cu, Ni, Mo and W substrates are shown in Figures 35 through 38. As before, there is a work function minimum for all four cases. The work function measurements were normalized to a value of 1.9 eV[40] for thick Cs coverage, which was obtained when the NISEC values reached those previously obtained for thick Cs. The lowest value of the work function was obtained for Cs on Mo (1.3 eV), then Cs on Ni (1.35 eV), Cs on W (1.5 eV) and Cs on Cu (1.7 eV). The value of 1.5 eV for Cs on W agrees well with the literature [45] while the value of 1.35 for Cs on Ni is the literature value for Cs on Ni oxide.[46]

The NISEC measurements for Cs on Cu and W show a maximum corresponding to the work function minimum for both incident energies. The maximum NISEC for Cs on W is 0.10 and for Cs on Cu it is 0.09; the higher yield from W is expected based upon work function and reflectively arguments. It is interesting to note that the NISEC of 0.10 for Cs on W is less than the NISEC of 0.12 for Li on Cu; why this is so is not clear. The maximum NISEC for Cs on Ni occurs after the minimum in the work function and it appears as if the maximum NISEC for 900 eV/d incident energy occurs after the maximum for 400 eV/d incident energy. A similar result was obtained in the measurements from Cs on Mo, but in this case the effect was more pronounced: The 400 eV/d incident energy NISEC showed only a slight maximum and the 900 eV/d incident energy NISEC showed no maximum at all.

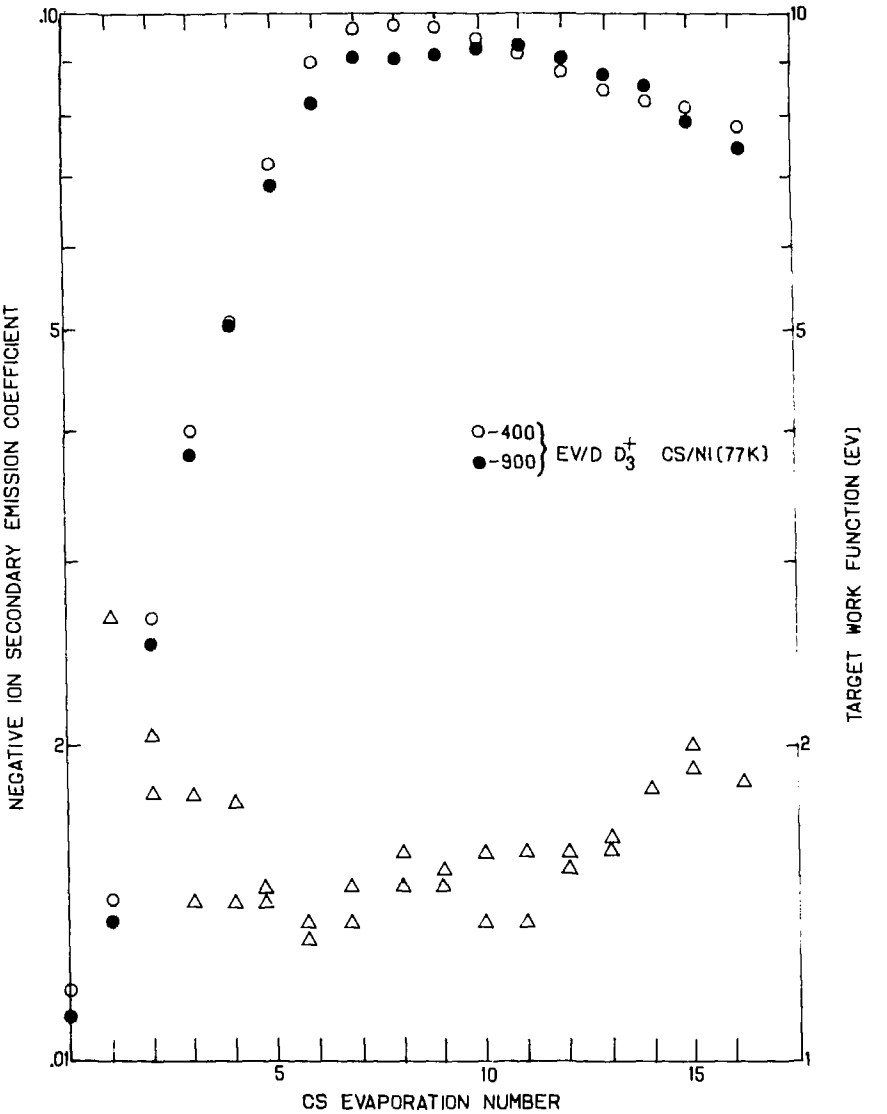

XBL 7912-13638

Figure 35. Surface work function-- △, and NISEC for 400 eV/d-- O and 900 eV/d-- ●, D_3^+ incident vs evaporation number for Cs deposited on a Ni substrate cooled by liquid nitrogen.

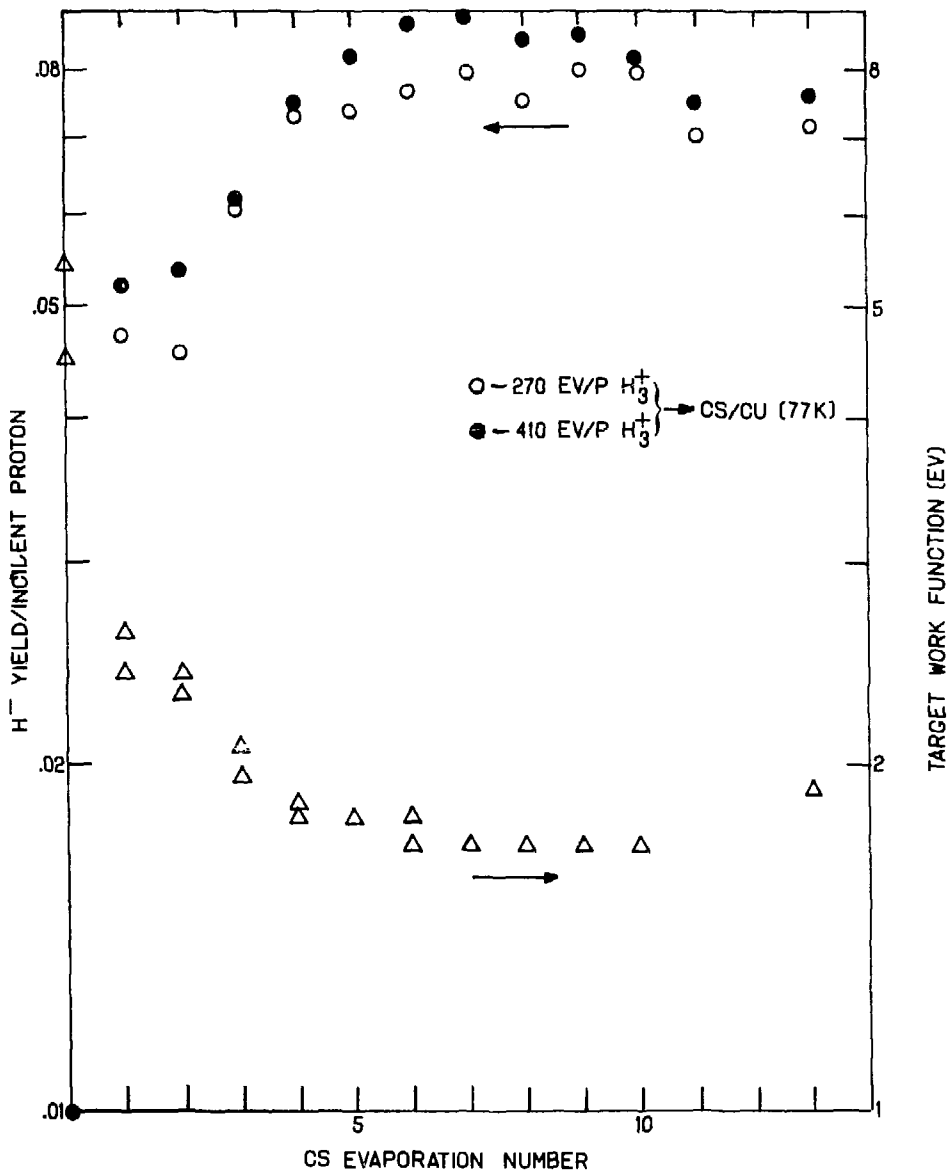

XBL 7911-12674

Figure 36. Surface work function-- △, and NISEC for 270 eV/p-- ○ and 410 eV/p-- ●, H_3^+ incident vs evaporation number for Cs deposited on a liquid-nitrogen-cooled Cu substrate.

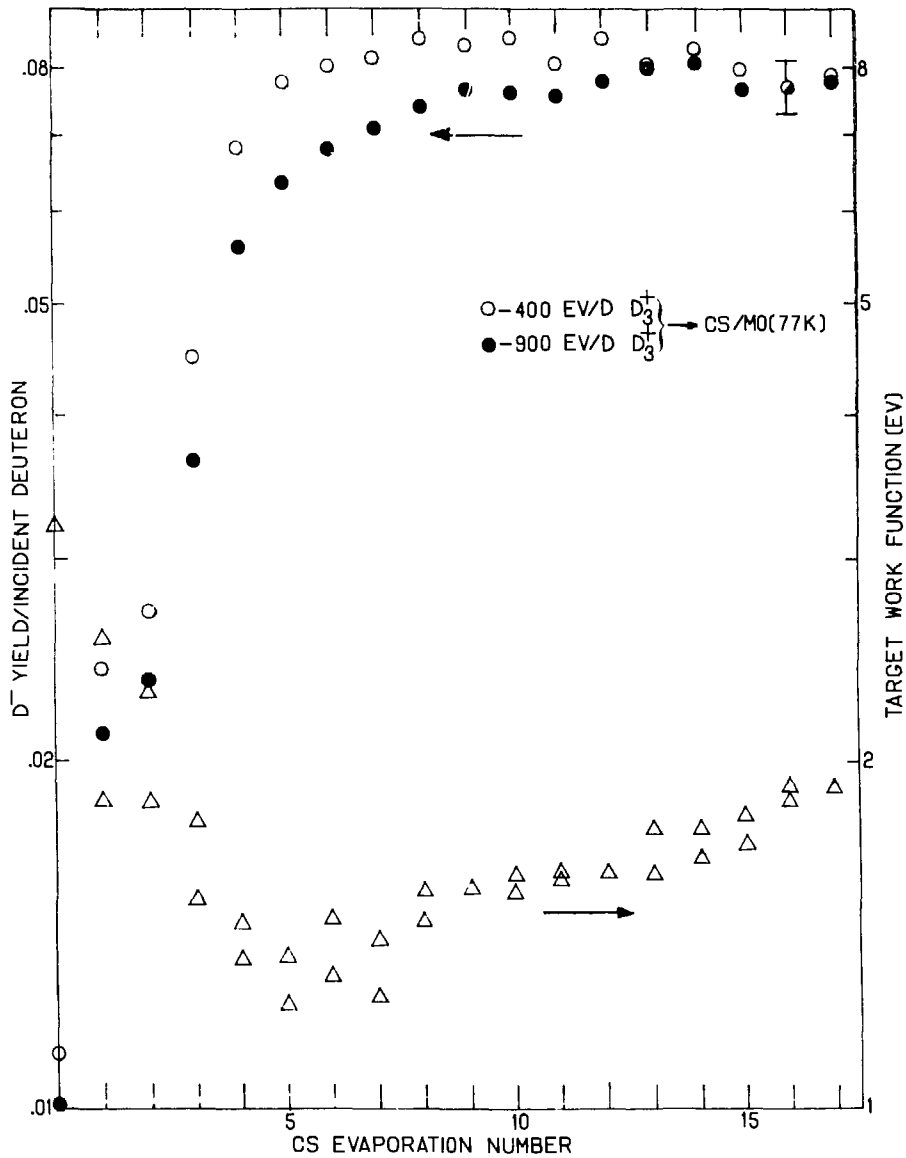

XBL 7911-12673

Figure 37. Surface work function-- Δ, and NISEC for 400 eV/d--O and 900 eV/d-- ●, D_3^+ incident vs evaporation number for Cs deposited on a liquid nitrogen-cooled Mo substrate.

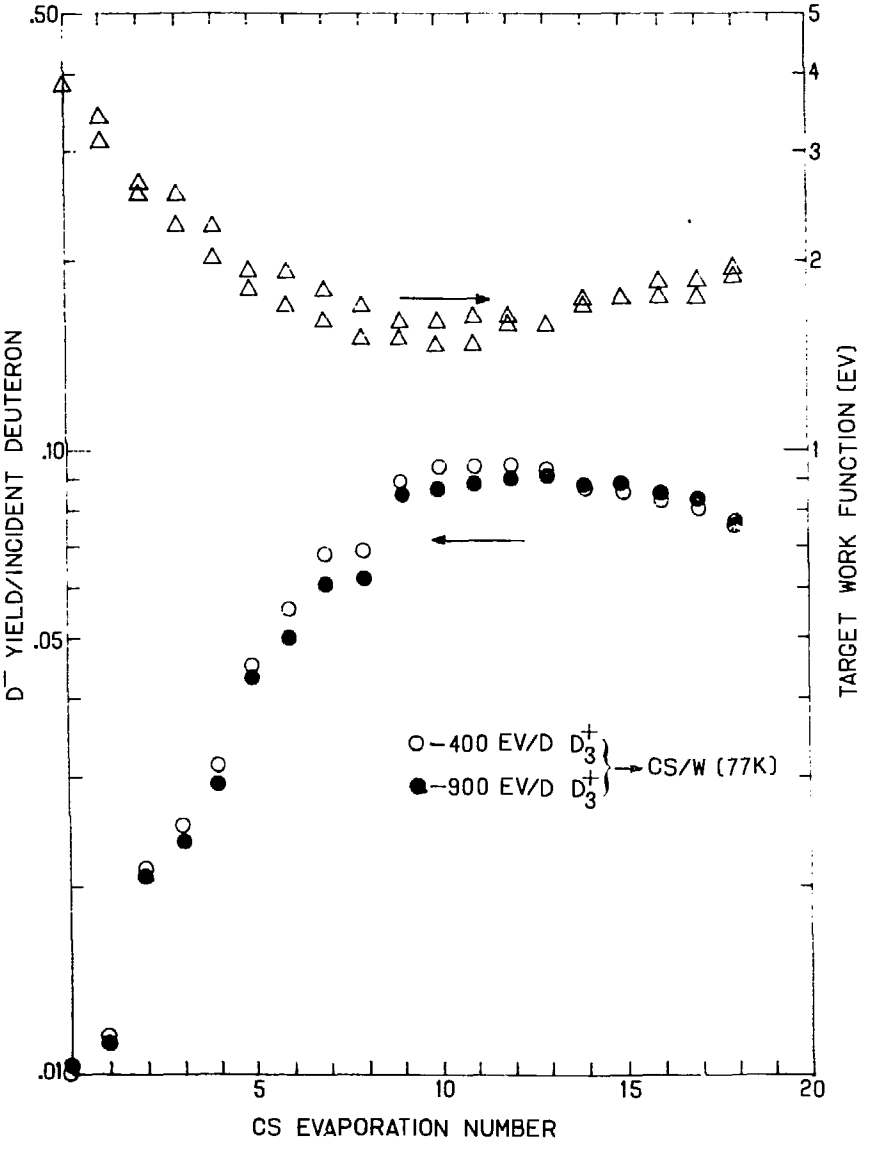

XBL 7911-12698

Figure 38. Surface work function-- △ , and NISEC for 400 eV/d-- ○ , and 900 eV/d-- ●, D_3^+ incident vs evaporation number for Cs deposited on a liquid-nitrogen-cooled W substrate.

The Cs on Mo and Ni results could be explained in the same way as the Li results: Assume that the Cs coverage at the work function minimum is thick enough to influence the backscattered distribution and reflected fraction. As the Cs coverage is increased, the losses in the NISEC due to increased work function would be compensated by the increased reflection from Cs (Marlowe[31] results show that at these energies, Cs reflects about 25 percent more particles than Mo and 40 percent more than Cu, which is comparable to Ni). If the reflection from Cs increases over the entire range that the work function increases, there would not necessarily be a maximum in the NISEC, as is the case for 900 eV/d D_3^+ incident on Cs on Mo. If the Cs thickness masks the substrate before the work function has attained the value of thick Cs, the NISEC will decrease as more Cs is deposited until the work function reaches the thick Cs value, giving rise to a NISEC maximum as is the case for the lower incident energy in Figure 35 (the range of 400 eV/d deuterons is less than the range of 900 eV/d deutrons, so a thinner layer of Cs required to mask the substrate for the lower energy particles.)

Because a method for measuring the alkali metal thickness on the target was not available and since the coverage of Li on Cu and W and the coverage of Cs on Mo and Ni could be many atomic layers thick, it is not known what thickness the coverage of Cs on Cu and W was at the work function minimum.

C. Data Fitting

Hiskes and Schneider[47] have developed a technique to quantitatively determine the dependence of the NISEC upon R_N, f and P_-: The Marlowe[31] code was used to obtain the angular and energy distributions of protons and deuterons reflected from each of the alkali-metal targets. The angular distribution closely approximated a cosine distribution so that n(v)dv could be separated into two parts and the angular dependence integrated out of equation (9) of Chapter II (see Appendix F), giving:

$$\text{NISEC} = \frac{1}{N_i}\int_v \Bigg[e^{-\beta/v}[1 - \beta/v - e^{\alpha/v}(1 - \tfrac{\alpha+\beta}{v})]$$

$$- \frac{\beta^2}{v}[\gamma + n(\beta/v) + \sum_{n=1}^{\infty} \frac{(-1)^n \beta^n}{nn!v^n}]$$

$$+ (\tfrac{\alpha+\beta}{v})^2 [\gamma + \ln \tfrac{\alpha+\beta}{v} + \sum_{n=1}^{\infty} \frac{(-1)^n(\alpha+\beta)^n}{nn!v}]\Bigg] n(v)dv$$

where

$$\alpha = \int_0^{x_0} P(x)dx$$

$$\beta = \int_0^{\infty} Q(x)dx$$

γ = 0.57722.... = Euler's constant.

The reflected energy distribution was divided into ten equal parts and converted into a velocity distribution. The resulting velocity distribution was divided into ten equal increments and the number of particles in each increment was determined. Then the integral in equation (2) was replaced by a sum over the velocity increments.

$$\mathrm{NISEC} = \sum_{j=1}^{10} \Bigg[A_j \; e^{-\beta/v_j} \Big[\beta/v_j - e^{-\alpha/v_j} \left(1 - \frac{\beta+\alpha}{v_j}\right) \Big]$$

$$- (\beta/v_j)^2 \Big[\gamma + n\,\beta/v_j + \sum_{n=1}^{\infty} \frac{(-1)^n \beta^n}{nn!\; v_j^{\,n}} \Big] \qquad (3)$$

$$+ \frac{(\alpha+\beta)^2}{v_j^{\,2}} \Big[\gamma + \frac{(\alpha+\beta)}{v_j} + \sum_{n=1}^{\infty} \frac{(-1)^n \, (\alpha+\beta)^n}{nn!\, v_j^n} \Big] \Bigg]$$

where A_j = the total number of reflected particles in the jth velocity increment, normalized to N_i

v_j = the average velocity in the jth velocity increment.

For each alkali-metal, the A_j values were calculated for various proton and deuteron incident energies, and are tabulated in Table 2. The measured NISEC values were used for the left hand side of equation (3) and a least squares fitting program was used to determine α and β. The infinite series in Equation (3) were carried out to 130 terms; fits were made using 50, 75, 100 and 130 terms and the differences in the values of α and β obtained with 75 and 130 terms was less than 1 percent. Also, some fits were made using five velocity increments as well as ten and again, the values of α and β changed by less than 2 percent each for both cases.

TABLE 2. Tabulation of the values used in the least squares fit of the NISEC data.

Target	Beam	E_{inc} (eV)	A_1^*	A_2	A_3	A_4	A_5	A_6	A_7	A_8	A_9	A_{10}	$NISEC_e^\dagger$
Cs	H	200	1.2	3.6	6.0	13.3	24.5	36.6	62.0	67.8	109.8	114.2	73
		300	2.6	7.7	12.8	20.2	28.0	34.0	43.3	61.4	103.4	107.3	76
		500	3.2	9.5	15.9	21.7	29.8	34.6	52.9	59.4	86.4	77.7	72
		700	3.3	9.9	16.5	20.1	25.7	34.2	43.8	58.7	99.2	73.6	69
		1000	3.0	8.9	14.8	17.1	26.0	37.5	48.4	60.5	77.3	55.2	61
	D	150	1.8	5.4	9.0	16.2	19.7	27.9	39.0	70.9	126.2	145.9	60
		300	3.0	9.0	15.0	20.4	25.6	37.2	48.9	75.7	108.1	104.0	75
		500	2.4	7.2	12.0	21.0	26.9	41.3	46.9	80.6	96.4	77.4	79
		700	3.6	10.8	18.0	20.4	24.2	31.0	37.2	65.7	90.5	76.7	78
		1000	1.6	4.8	8.0	23.1	29.5	34.8	50.9	79.5	87.8	76.0	74
		1500	2.0	6.0	10.0	14.6	28.1	40.5	49.6	55.4	90.6	71.1	66
Rb	H	300	3.0	9.0	15.0	15.1	24.3	37.5	40.2	64.9	72.3	79.7	55
		500	2.9	8.7	14.5	17.3	25.0	40.0	46.1	51.5	79.7	47.3	57
		700	2.4	7.2	12.0	18.0	28.2	36.7	43.9	51.8	77.5	40.4	57
		1000	1.8	5.4	9.0	18.5	25.7	35.4	41.0	46.8	60.8	51.5	55
	D	200	1.3	3.9	6.5	20.4	27.3	34.8	41.5	65.2	97.4	78.6	40
		300	1.8	5.4	9.0	17.4	29.2	31.3	50.1	66.9	80.2	65.7	48
		500	1.3	3.9	6.5	13.9	24.2	36.9	37.5	64.9	74.9	56.0	56
		700	1.3	3.9	6.5	13.9	21.8	37.3	44.9	65.8	61.2	44.5	57
		1000	2.4	7.2	12.0	15.0	21.8	28.0	48.2	60.5	80.5	45.5	55
		2000	1.8	5.4	9.0	11.4	17.3	30.6	40.2	40.9	66.5	30.8	46
K	H	300	1.9	5.7	9.5	19.3	23.7	28.7	38.2	45.5	61.3	31.2	38
		500	1.9	5.7	9.5	16.3	25.9	27.5	34.1	46.6	37.3	30.2	40
		700	2.1	6.3	10.5	14.7	18.9	26.0	31.1	31.5	39.8	22.1	38
		1000	2.3	6.9	11.5	10.7	20.8	28.8	28.6	28.6	27.0	20.1	23
		3000	1.4	4.2	7.0	13.4	16.1	19.9	17.9	17.9	13.5	4.7	18
	D	300	2.3	6.9	11.5	13.1	24.4	33.2	29.3	42.9	45.2	17.2	27
		500	1.5	4.5	7.5	14.3	19.8	23.0	33.4	45.8	55.9	16.8	32.5
		1000	1.2	3.6	6.0	13.2	19.9	24.6	38.9	46.7	37.3	12.7	34
		2000	1.8	5.4	9.0	15.0	17.4	25.7	29.7	28.4	24.3	6.3	26.5

(continued . . .)

TABLE 2 (continued)

Target	Beam	E_{inc} (eV)	A_1 *	A_2	A_3	A_4	A_5	A_6	A_7	A_8	A_9	A_{10}	$NISEC_e$ †
Na	H	300	7.8		22.4		42.1		65.6		50.6		21
		400	7.6		21.4		40.6		50.8		46.7		24
		700	9.4		26.2		39.9		52.2		27.4		26
		1000	8.1		20.4		38.0		38.4		31.3		25
		2000	7.0		19.6		26.0		35.8		14.5		19
		3000	4.1		11.3		12.2		12.9		6.5		11.5
	D	200	6.8		21.3		44.9		69.9		31.7		7
		500	6.6		20.6		36.5		51.8		29.5		14
		700	6.8		21.3		42.3		54.4		19.6		17.5
		1000	6.2		19.4		38.5		42.5		22.9		18
		2000	4.8		15.0		24.6		33.7		7.0		17
Li	H	250	0.88	2.64	4.39	6.75	10.75	13.18	10.47	12.73	2.42	0	2.45
		375	0.88	2.64	4.40	5.56	7.11	10.67	10.27	8.83	1.85	0	2.8
		500	0.98	2.92	4.87	5.19	7.26	10.62	8.85	5.84	1.21	0	2.9
		700	0.78	2.33	3.88	4.96	7.81	9.41	7.71	4.56	1.57	0	3.0
		1000	0.50	1.50	2.50	5.08	5.60	4.32	3.60	2.43	1.17	0	2.7
		2000	0.42	1.24	2.07	3.30	3.21	2.38	2.23	1.26	0.40	0	1.9
	D	400	0.60	1.80	3.00	4.50	6.40	7.74	4.43	5.30	0	0	0.95
		500	0.58	1.75	2.92	3.59	5.15	5.90	3.77	0.95	0.10	0	1.1

*The A_j values are multiplied by 1000 for convenience in manipulation, and these values are appropriate for a system of units where the velocity of a 200 eV proton is unity. The reflected fraction is given by summing the A_j's and dividing by 1000.

†The NISEC values given are the experimental measurements, and are multiplied by 1000 for convenience.

Usually, ten or more data points were used to determine α and β. Since only two parameters were determined by ten equations, they were over-determined and a good fit to the data is unlikely unless the functional form of the expressions is correct. The closeness of the fits indicate that this is the case.

The α and β obtained for each of the alkali metals are given in Table 3. (Note that these α and β are based upon a normalization of velocity such that the velocity corresponding to a 200 eV proton is unity). The NISEC values based upon these α and β are plotted in the overlays to Figures 22 through 31. It is encouraging to see that the same values of α and β fit the NISEC curves for both H and D incident on a given alkali-metal target. This result is expected because the probabilities of formation and survival should only depend upon surface properties of the target, the binding energy or the negative ion, and the exit velocity of the ion.

With values for α and β, we now have analytical expressions for the probabilities of formation and survival of H^- and D^- as a function of exit energy. We can compare expression for the survival probability obtained with this fit to the theoretical calculations of Hiskes and Karo[23]. From Figure 39, we see that the agreement is very good in terms of the shape of the curves.

The probability that a particle leaving the target at a given perpendicular exit velocity will be detected as H^- is the production probability and is given by the product of formation and survival probabilities. The production gives the upper limit of the NISEC for a given surface: If all the incident particles were reflected with the

TABLE 3. Summary of the results of the least squares fits to the NISEC data.

Target	α	β	Work function ϕ_w (eV)	E_{exit}^{*}	$(fP_-)_{max}$	$\alpha/n_e^{\dagger}$	$\alpha/n_e(\phi_w-0.75)^{\frac{1}{2}}$
Cs	0.387	0.479	1.86	85	0.215	2.09	2.24
Rb	0.435	0.578	2.08	120	0.204	1.85	2.15
K	0.500	0.649	2.24	150	0.207	1.72	2.11
Na	0.940	0.944	2.28	370	0.249	1.71	2.13
Li	0.394	1.09	2.42	325	0.113	0.394	0.52

* E_{exit} is the perpendicular exit energy of a proton, corresponding to the maximum in the production probability.

† n_e is the conduction electron density normalized such that n_e is unity for Li.

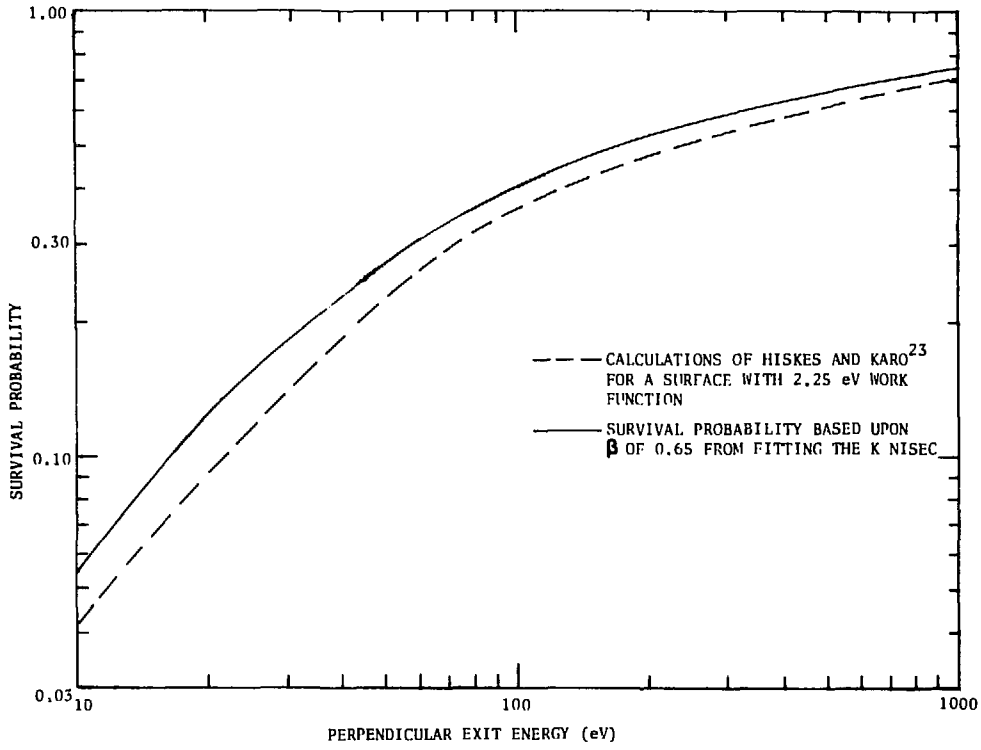

Figure 39. H^- survival probability vs perpendicular exit energy, as calculated by Hiskes and Karo[23] for a surface work function of 2.25 eV---, and as calculated using the β = 0.65 from the fit to the potassium NISEC (Work function of 2.24 eV[40]) obtained in this paper ——.

optimum exit velocity the NISEC would equal the maximum production probability. The production probability at the optimum exit velocity is tabulated in Table 3 for each of the alkali metals. It is interesting to see that Na has the highest production probability of all the alkali metals.

Na has the highest production probability because it has the highest value for α, even though it has the second highest value for β: The high β gives a low probability of survival, but is compensated by the high α which gives a high probability of formation. Based upon work function considerations, we would expect Cs, with the lowest work function, to have the largest α. Since this is not the case there must be other factors in α. In fact, it was discovered that if α was divided by the conduction electron density, n_e, (assuming one conduction electron per atom), the ordering became as expected based only on work function considerations (see Table 3). Note how close the values of α/n_e are for K and Na, whose work functions only differ by 0.05 eV.[40] When α/n_e was multiplied by the square root of the difference between the target work functions and the H^- binding energy, the resulting value was the same for four of the five alkali-metal targets, Li being the exception (see Table 3).

Since α and β depend upon surface properties of the target and not bulk properties, we should be able to predict the NISEC for H bombarding a Cu target with just enough Na (~1 monolayer) to give a surface work function of thick Na (2.3 eV): The α and β which were obtained from a thick Na target were used, along with the n(v) from the Marlowe[31] code for a Cu target. The measurements of the NISEC from a Na on Cu target

are shown along with the predicted values in Figure 40. As can be seen, the agreement is good, which is further indication of the validity of this analysis.

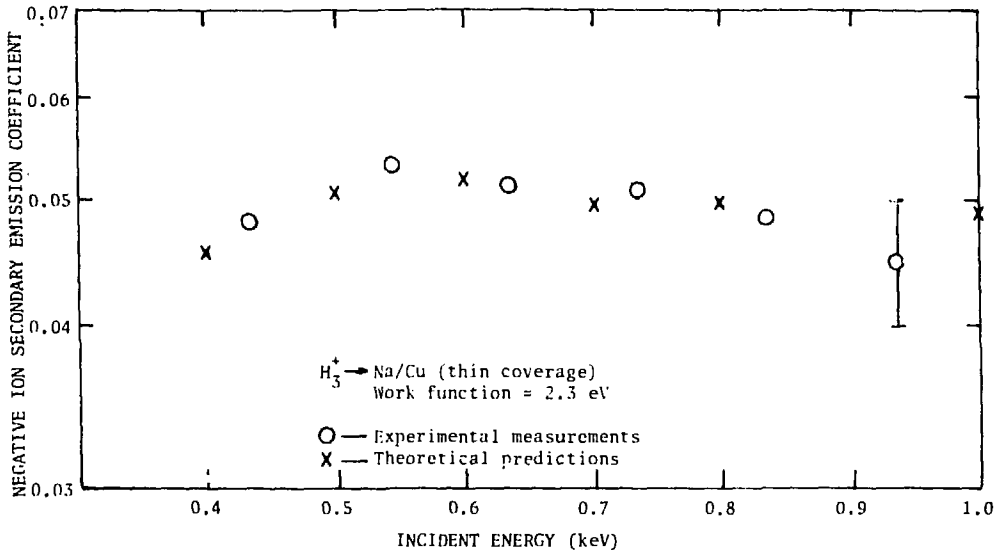

XBL 803-8610

Figure 40. NISEC vs incident energy for H_3^+ incident on a Cu target with thin Na coverage, such that the surface work function is the same as that of thick Na. The experimental measurements are given by --O, and the predictions using the α = 0.940 and β = 0.944 obtained for thick Na, along with the backscattered distribution from Cu are given by -- X.

CHAPTER VI

APPLICATION OF RESULTS TO CONTROLLED FUSION

There are currently two types of negative ion sources for neutral beams which would use surface production: (1) The converting surface (where H^+ and H^0 are converted to H^-) is within the discharge and (2) the converting surface is expernal to the discharge. The first type includes the Magnetron[7,8] and the Self Extraction Source.[48] In these sources a sheath potential exists between the discharge (the source of the particles to be converted to H^- and the converter surface. Positive ions are accelerated through the sheath, and because the potential drop across the sheath is large compared to the ion energy, the ions are incident normal to the surface. In this case, the results of the present experiment have a direct bearing. Because less than 10 percent of the incident particles are converted to H^-, a large flux to the conversion surface is required to achieve sizeable H^- currents from the source. The required flux will be even larger when we take into consideration that once the H^- is produced it must still traverse the plasma before it can be extracted, so only a fraction of the H^- ions will make it out of the source.

Computer calculations[21,31] of reflection of particles with energies greater than 100 eV, normally incident on surfaces show that less than 50 percent of the incident particles are reflected and even less of the incident energy is reflected (see Figure 41). Therefore, as a result of the large incident flux, the converter is heated by the deposited energy, and this energy must be removed to preserve the surface—this is the reason the Magnetron is operated in a pulsed mode:

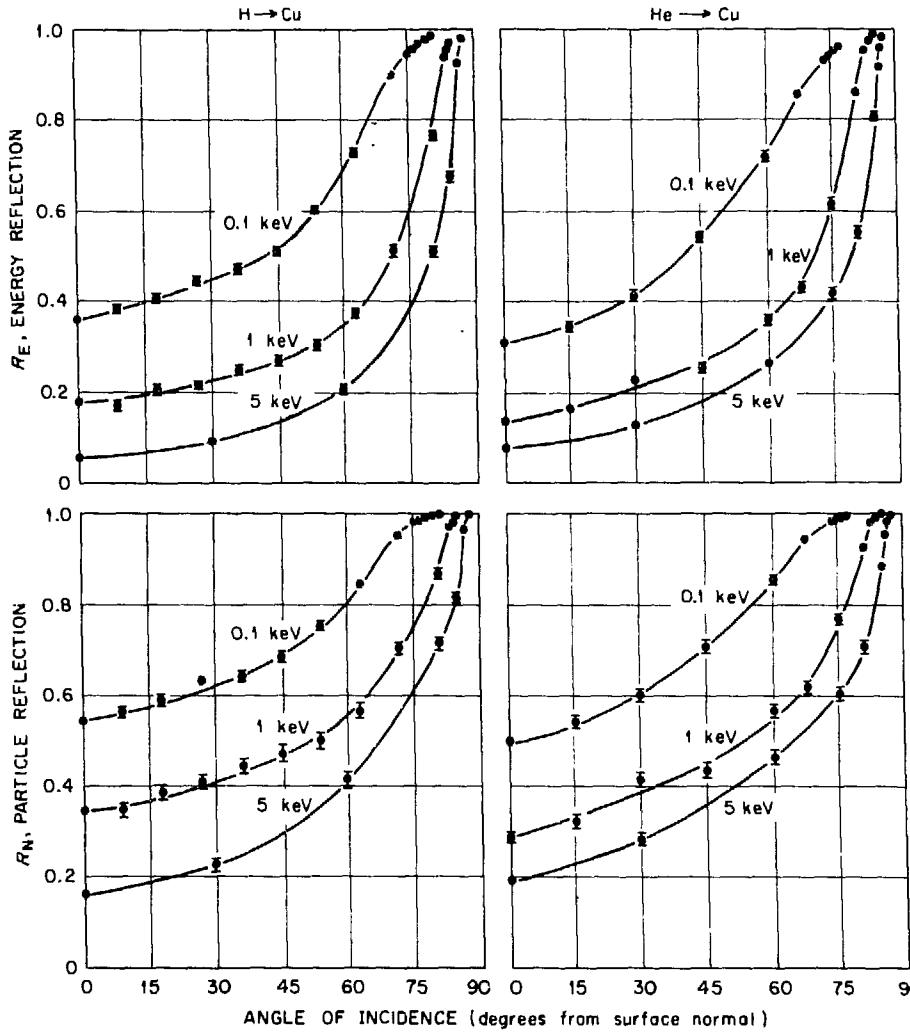

Reflection Coefficients vs Beam Angle.

XBL 803-8732

Figure 41. Particle and energy-reflected fractions for hydrogen and helium incident on a Cu target, as a function of the angle of incidence, as calculated by the Marlowe Code.[31]

to allow cathode cooling between pulses. Converter heating will always be a problem, even if all the emerging particles were H^-, at least half of the incident energy is still deposited in the converter and must be removed.

Another problem arising from a high flux to the converter is the sputtering away of the converter surface. The low work function surfaces used to enhance the H^- yield from the converter are made up of a thin coating of Cs on W or Mo, so that a means for replacing the Cs coating is necessary to maintain the H^- production. The presence of Cs in the discharge allows the establishment of an equilibrium between sputtering and condensation of Cs at the converter surface. But if some of the more exotic surfaces with lower work functions (i.e., BaO--ϕ_w = 1.4 eV, Cs_2O_2—ϕ_w = 1.1 eV)[44,49] are used to enhance the conversion efficiency, they will be sputtered, and it may not be possible to replenish the surface by condensation of constituent species from the discharge because of the complex nature of the surface.

Finally, the converter produces not only H^-, but also electrons which also get accelerated across the sheath and may be extracted along with the H^-. These electrons are usually suppressed with a magnetic field, but this field must affect the H^- beam optics to some extent.

In the second type of H^- source, the converting surface is external to the discharge. A system using this concept has been presented by Anderson[50]. In Anderson's scheme, a low energy (about 20 eV) beam is produced in a separate source and transported to the "Venetian blind" converter. The beam is incident on the converter at a grazing angle, and a fraction of the reflected particles emerge as

H^-. Before looking at the relative merits of this concept, we can look at the required incident energy of the incident particles, in light of the results of the present experiment.

The NISEC measurements for the alkali-metal surfaces show maxima at incident energies on the order of several hundred electron Volts (higher for D, which is the isotope to be used for fusion, than for H). The computer simulations[21,31] show that the energy distribution of the reflected particles is strongly peaked at an exit energy slightly lower than the incident energy, in which case, the optimum exit energy (corresponding to the optimum $v_\perp$ in equation (9) of Chapter II) would be approximately half of the incident energy for deuterium. Thus, the optimum value for the perpendicular component of the exit energy would be of order of 200 eV (for D). Now, going back to the incident energy of the particles to the converter, we see that 20 eV is much too low. In fact, if we take as an example, a perpendicular exit energy of 200 eV and an angle of incidence of 80° to the surface normal, the total beam energy would be 6.6 keV, and if the positive beam is made up of D_2^+ or D_3^+, this energy would be doubled or tripled.

With this higher energy in mind, we can now look at the merits of Anderson's approach:

(1) The grazing incidence onto the converter has several advantages:

(a) The NISEC should be as much as three times larger than measured in this work because of the increased reflected fraction alone (see Figure 41).

(b) The energy distribution of the emerging particles will be more shaprly peaked, so that a larger fraction of the reflected particles will be H^-.

(c) Because of the much larger fraction of the incident energy and the incident particles which are reflected, the heat deposited in the converter will be minimized.

(d) The sputtering rate will be much lower than for normal incidence because a much smaller fraction of the incident energy is deposited in the surface, so hybrid surfaces will last longer, and becasue the converter is outside of the discharge, the converter is more accessible.

(2) Although secondary electrons are produced at the converter, their energies are below a few hundred electron Volts, so they can be separated from the beam, either electrically or magnetically, using field strengths too low to affect the beam significantly.

(3) The "Venetian blind" structure serves as a gas flow impedance to separate the relatively high pressure D^+ source from the low pressure fusion reactor.

The above considerations make this approach look promising, but more information is needed about the energy distribution perpendicular to the beam direction, as well as measurements of negative ion yields for grazing incidence.

CHAPTER VIII

SUMMARY AND CONCLUSIONS

The negative ion secondary emission coefficients (NISEC) have been measured for H_2^+, H_3^+, D_2^+ and D_3^+ bombarding thick, clean targets of Cs, Rb, K, Na and Li, with incident energies from 150-to-4000 eV/nucleus. When normalized to the number of nuclei per incident molecular ion, the NISEC curves are identical (within experimental errors), for incident ions of the same isotope (i.e., H_2^+ and H_3^+), but there is an isotope effect between H and D ions incident. The isotope effect is weakest for a Cs target and becomes more pronounced in going from one target to another in the order: Cs, Rb, K, Na and Li.

All targets show a maximum value of the NISEC, for both H and D ions incident. The higher the maximum value of the NISEC, the lower the incident energy at which it occurs, with the highest NISEC (0.08) resulting from 300 eV/nucleus H ions on Cs. Also, the value of the NISEC decreases in the order: Cs, Rb, K, Na and Li, at any incident energy for either H or D ions incident. For all targets except Li, the NISEC curves for H and D ions incident cross over.

The NISEC has also been measured for 8.0 keV Ar^+ ions bombarding all of the alkali-metal targets, and based upon the results, arguments have been presented which indicate that for H and D ions incident, the collected negative ions are reflected incident particles rather than impurity negative ions spurrered from the target.

The NISEC and corresponding surface work function have also been measured as a function of thickness for Na, Li and Cs coverages of Cu, Ni, Mo and W. In all cases, the work function exhibited a minimum value and the NISEC exhibited a maximum value as the thickness of the alkali-metal coverage was increased, For Na on Cu, even when the Na coverage was thick enough to result in a work function equivalent to thick Na, the NISEC for the Na/Cu target was twice as large as for thick Na.

The NISEC measurements for thick alkali-metal targets, along with computer calculations of backscattered particle energy-and angle distributions, have been used in a least squares fitting program to determine two parameters in a semi empirical treatment of negative ion production from surfaces. The fits obtained agreed well with the NISEC measurements over the entire range of incident energies, as well as for all of the alkali-metal targets.

In conclusion, the following topics are suggested for further experimental investigation:

(1) Since the reflected fraction is important to the NISEC experiments using massive targets such as U^{238} as a substrate with a thin coverage of alkali-metal are necessary.

(2) NISEC measurements using glancing incidence rather than normal incidence of the bombarding ions may show increases by a factor of two or three.

(3) Surface analysis apparatus, e.g. Auger spectroscopy, LEED, should be added.

(4) Single crystal targets should be used so that the target conditions can be better defined.

(5) Targets consisting of metal solutions may enhance the reflected fraction.

APPENDICES

A. Impurity Analysis

A residual gas analyzer[37] was modified to enable identification of positive and negative ions sputtered from the target. The analyzer consisted of three parts: (1) The ionizer head (2) the mass filter and (3) the ion detector. Since the particles to be analyzed were already ions and operation of the ionizer would ionize background gas, the ionizer head was removed, leaving only the mass filter and the detector.

(1) The Mass Filter

The mass filter considered of four rods, mounted with their cylindrical axis on a circle, as shown in Figure 42. These rods were biased with a combination of RF and DC electric field, also shown in Figure 42. The frequency of the RF was 1.8 MHz and its amplitude could be varied from 0 to 2400 Volts RMS to sweep through masses up to 300 a.m.u. The amplitude of the RF voltage determined which mass would have a stable trajectory through the filter and emerge at the exit aperture. All other masses would be ejected from the central region of the filter and would not pass through to the ion detector. The DC/RF ratio is kept constant as the RF voltage is swept, and determines the resolution of one mass peak from another. A complete discussion of ion trajectories through a quadrupole mass filter is available in the literature.[51,52]

(2) The Ion Detector

The ions which passed through the exit aperture of the mass filter entered the ion detector, which consisted of a Channeltron (see Figure 42). The Channeltron multiplied the incident charge by a factor of

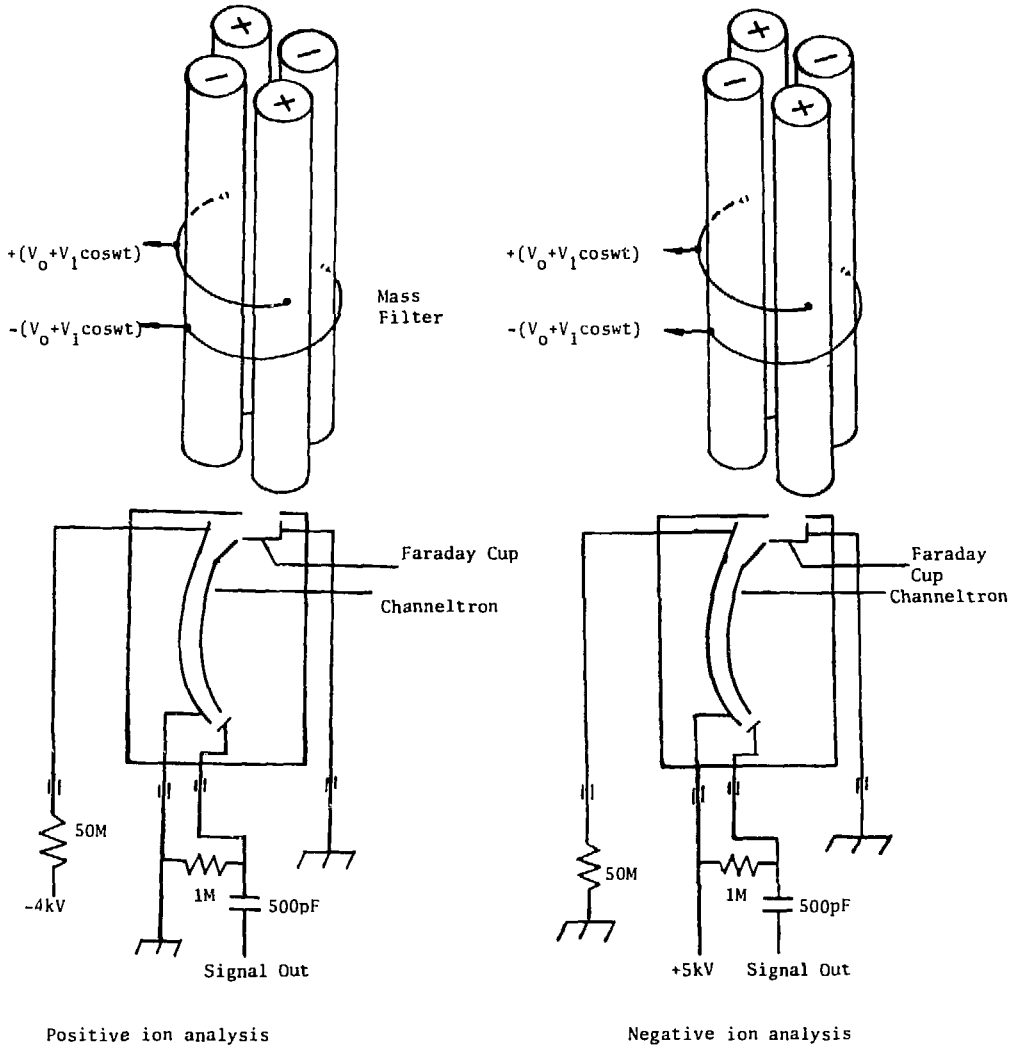

Figure 42. Illustration of the components of the quadrupole mass analyzer, showing the connections to the channeltron for both positive and negative ion detection.

10^5, and the emerging charge pulses were counted using the electronics shown in Figure 15. The voltages applied to the Channeltron had to be rearranged when converting from positive to negative ion detection, and the appropriate circuits are shown in Figure 42.

(3) Mass Spectra

Positive and negative ions were sputtered from the target using 8.0 keV Ar^+ ions, and only those ions leaving the target at an angle of 45° entered the mass analyzer. Because of the limited acceptance angle of the mass filter and because the efficiency of the detector varied for different ion species, the mass scan results were only a qualitative measure of the impurity ions from the target. In other words, a given mass peak indicated the presence of that mass on the target, but gave no indication of the concentration.

A copper target, which was cleaned by abrasion before entering the vacuum changer, was used as a reference surface for the mass analysis. Both the positive and negative ion mass scans for this target are shown in Figures 43 and 44. The positive ion scan shows the presence of all of the alkali metals, as well as, both isotopes of copper and an Ar^+ peak due to reflected incident ions. The broad plateau at the low mass end of the spectrum is due to the inability of the mass filter to separate out higher mass ions with high energy (> 150 eV), because the RF and DC fields are almost zero at this end of the sweep. The negative ion scan also shows several peaks, mostly carbon compounds with O^- and H^- also present.

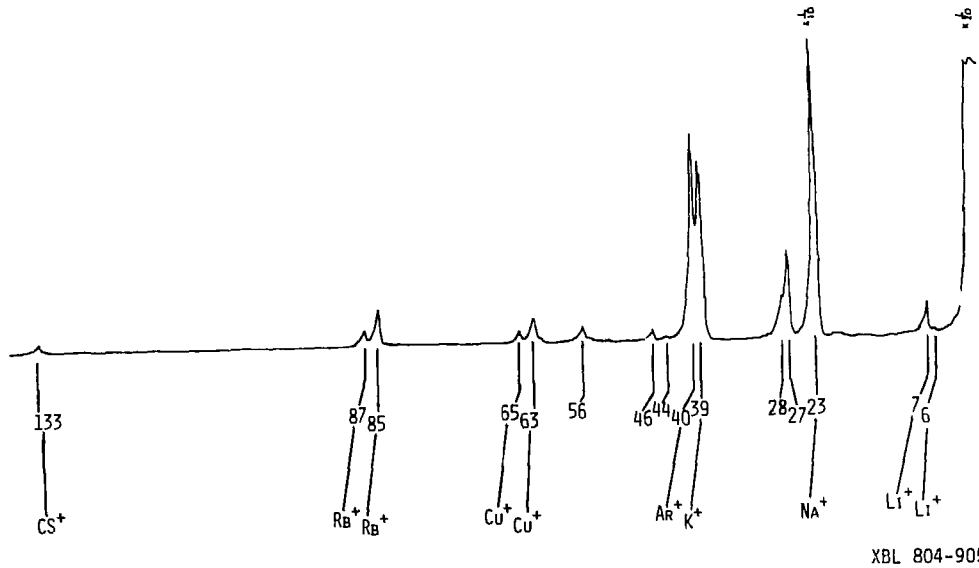

Figure 43. Mass scan of positive ions sputtered by 8.0 keV Ar^+ ions bombarding a Cu target.

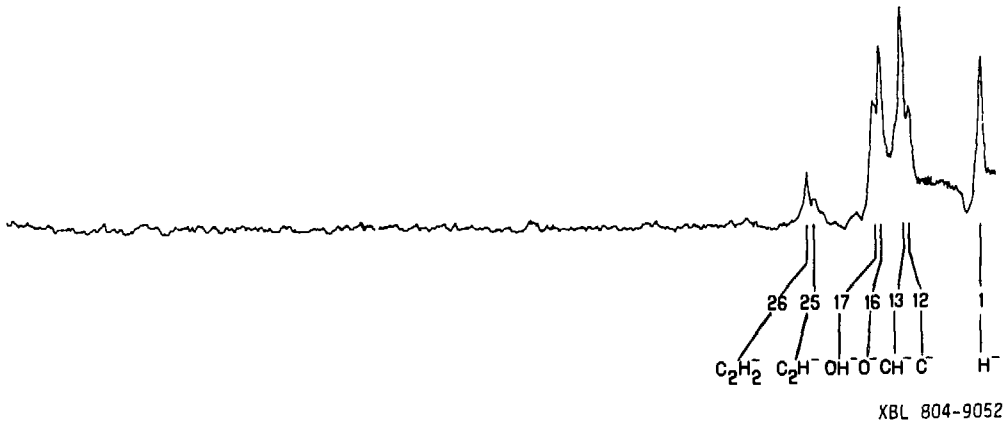

Figure 44. Mass scan of negative ions sputtered by 8.0 keV Ar^+ ions bombarding a Cu target.

Figures 45 and 46 show positive and negative ion scans of the same copper target with a fresh layer of Na deposited on it. The only peak present on the positive ion scan is that of Na^+ which shows that Na was indeed evaporated and that the other impurities have been buried beneath the Na layer. The negative ion scan still shows some impurity peaks, although the relative heights of the peaks have changed and some have disappeared altogether. The presence of these sputtered negative ions from the target make it necessary to determine the magnitude of their contributions to the NISEC (see Appendix E).

Positive and negative ion mass scans were recorded for all the alkali-metal targets and the results were similar to those of Na: The positive ion scans showed only one peak, corresponding to the alkali-metal present and the negative ion scans showed a few low mass peaks.

B. Work Function Measurements

Work function measurements were made using the electron beam version[36] of the retarding potential method.[34,35] A diode is made with a tungsten filament (the emitter) and the target surface (the collector). The difference in the work functions of the emitter (ϕ_e) and the collector (ϕ_c) is known as the contact potential, $V = \frac{1}{e}(\phi_c - \phi_e)$. When the emitter is heated, the electrons which are emitted have a Maxwell-Boltzmann energy distribution, so if $V_0 > 0$, all the emitted electrons reach the collecter. If $V_0 < 0$, then only that portion of the Maxwell-Boltzmann distribution with energies greater than eV_0 will reach the collector. A voltage applied at the emitter (V_a), subtracts

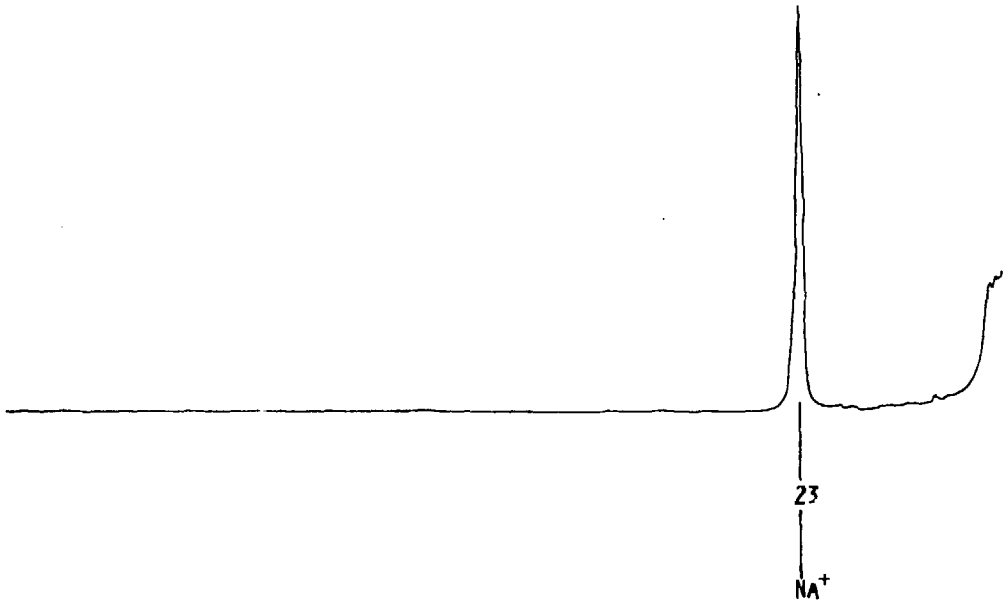

XBL 804-9053

Figure 45. Mass scan of positive ions sputtered by 8.0 keV Ar^+ ions bombarding the same Cu target as above, with Na coverage.

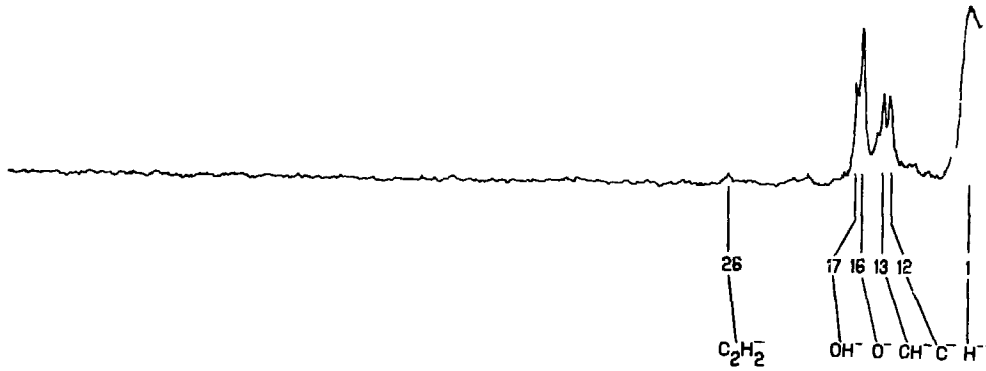

XBL 804-9051

Figure 46. Mass scan of negative ions sputtered by 8.0 keV Ar^+ ions bombarding the same Cu target as above with Na coverage.

from V_o to give a total voltage, $V = V_o - V_a$, between the emitter and the and the collector. If the collector current is monitored as V_a is varied, an I-V curve similar to the one shown in Figure 1B will be generated (see Figure 14 for a diagram of the electronics used to obtain the I-V curve).

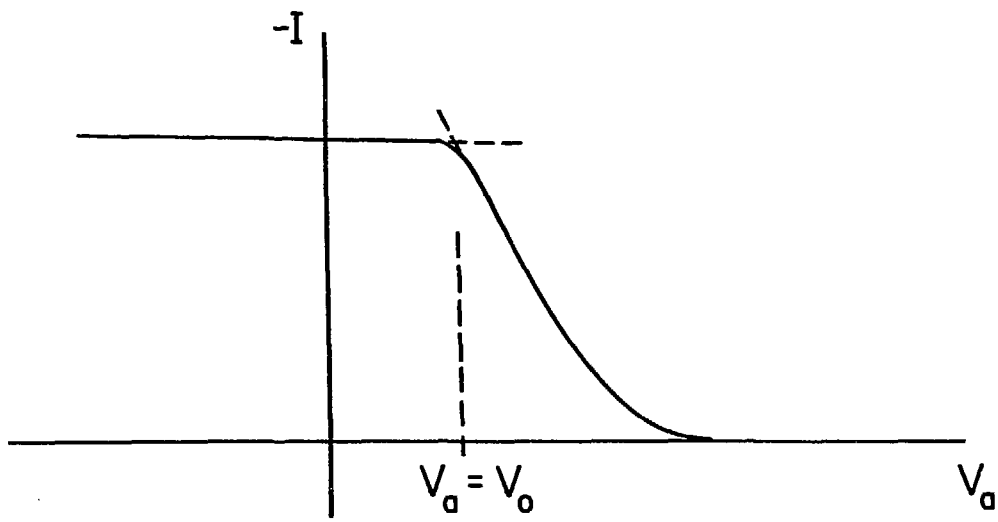

Figure 1B. I-V curve for the work function diode, $\phi_e > \phi_c$.

If the work function of the collector decreases by an amount, $-\Delta\phi$, then $V = -V_a + V'_o = \frac{1}{e}(\phi_c - \Delta\phi - \phi_e) - V_a = -V_a + V_o - \frac{1}{e}(\Delta\phi)$, where $-\frac{1}{e}(\Delta\phi)$ is a positive quantity because $\frac{1}{e}$ is negative for electrons. Therefore, the point where the knee in the I-V curve occurs,

$V_a = V_o$, has been shifted to the right, as shown in Figure 2B, by an amount equal to the change in the work function of the collector.

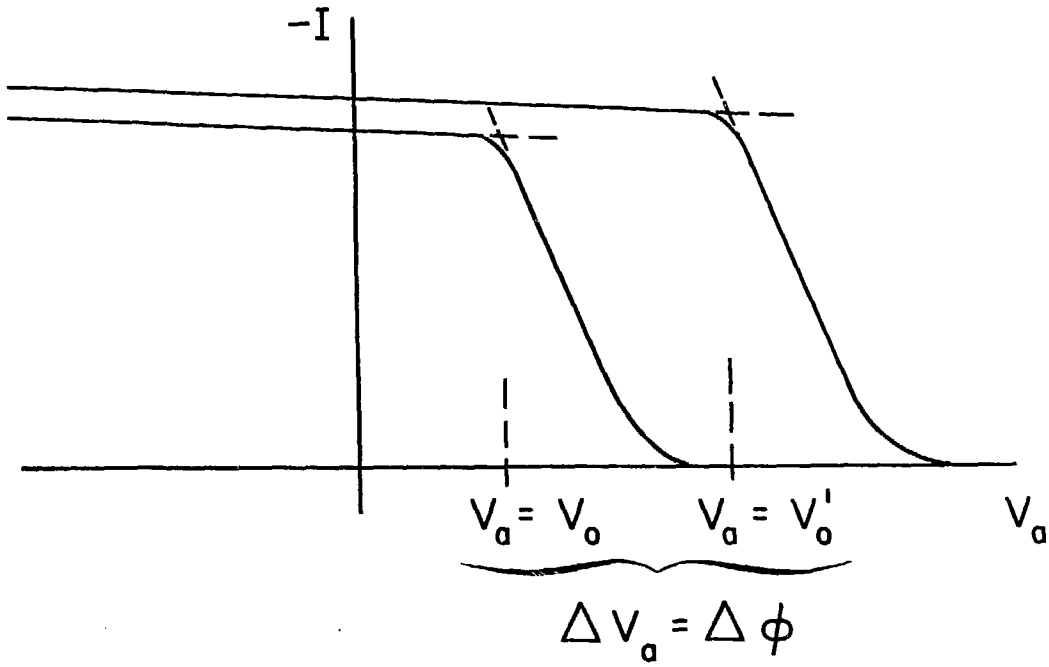

Figure 2B. The shift in the I-V curve due to a work function change.

This procedure gives only changes in the collector work function. To obtain absolute values of the work functions, and I-V curve must be generated for a surface of known work function. In general, when the alkali metal coverage exceeds one monolayer, the work function of the surface becomes that of the alkali metal,[42,46] so the alkali metal work function was used as a reference value.

C. Particle Orbit Calculations

The region between the target and the collector plates is permeated by perpendicular electric (E) and Magnetic (B) fields. To calculate the effects of these fields on a particle at the target surface, we start with the non-relativistic equation of motion of the particle:

$$m \frac{d\bar{v}}{dt} = q[E + \frac{1}{c} (\bar{v} \times B) \qquad (1)$$

if we transfer to a reference frame moving perpendicular to both E and B, with velocity, v_D, where,

$$\bar{v} = \bar{v}' + \bar{v}_D , \qquad \bar{v}_D = \frac{E \times B}{B} , \quad \bar{v}_D = \frac{E}{B} \; c \; \hat{z} \qquad (2)$$

equation (1) becomes

$$m \frac{d\bar{v}'}{dt} = \frac{q}{c} \bar{v}' \times B \qquad (3)$$

which is simply the equation of motion of a charged particle in a constant magnetic field, with no electric field present. This motion is a circular orbit, with orbital frequency, $\omega = \frac{qB}{mc}$, and radius $r_L = \frac{|\bar{v}'|}{\omega}$.

To determine if the ions produced at the target reach the collecter, we can apply equations (2) and (3) to two example cases: (a) the ion is at the target surface with no initial energy and (b) the ion leaves the target surface with the maximum possible energy, parallel to the drift velocity, v_D.

Case (a):

For $\bar{v} = 0$, $\bar{v}' = -\frac{Ec}{B}\hat{z} = -\bar{v}_D$.

As a worst case example, let $E = 100$ Volts/cm and $B = 350$ gauss.

$v' = 2.86 \times 10^7$ cm/sec.

$\omega = 3.4 \times 10^6$ radians/sec for hydrogen;

therefore, $r_L = 8.5$ cm.

This value of the particle orbit radius, $r_L = 8.5$ cm, is large compared to the gap between the target and collector plates, but in the laboratory reference frame, the particle has a velocity component in the $\hat{z}$ direction, and depending upon the time required for the particle to get across to the collector, it may have drifted up so far as to be above the collector plate, and miss it completely. To examine this possibility, we need to know the angle, θ, (see Figure 1C below):

$$\theta = \cos^{-1}\left(\frac{8.5 \text{ cm} - 1.5 \text{ cm}}{8.5 \text{ cm}}\right) = 0.6 \text{ radians}$$

therefore, the time required for the particle to get across is

$$\frac{\theta}{\omega} = 1.8 \times 10^{-7} \text{ sec}$$

In this time, the particle has moved in the $-\hat{z}$ direction in the drifting reference frame by

$$\Delta z = r_L \sin \theta = 4.8 \text{ cm}$$

and in the laboratory reference frame, the gryo-center (the point about which the particle orbits) has moved in the $+\hat{z}$ direction by

$$V_D \times \text{time} = 5.15 \text{ cm}$$

so the net motion of the particle in the z direction is 0.35 cm, which is small compared to the height of the collector plate (3.65 cm), and the ion will be collected.

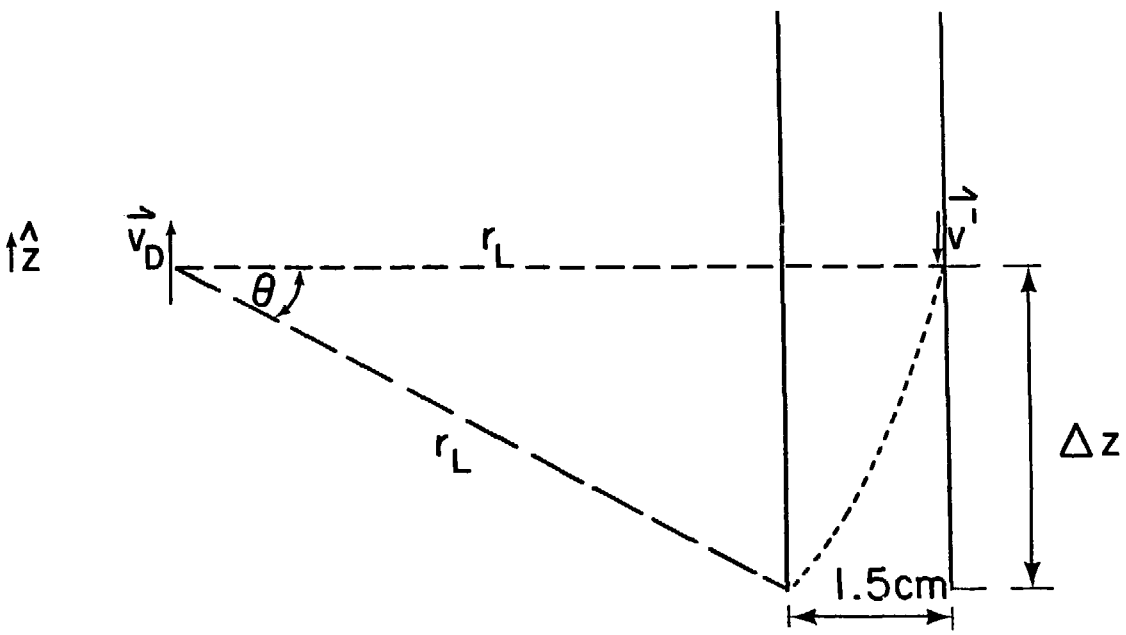

Figure 1C

Case (b):

The conditions are the same as case (a), except this time the particle has an energy of 100 eV, which corresponds to a speed of 1.37×10^7 cm/sec, and is directed along $+\hat{z}$.

$$v' = v_D - v = 1.5 \times 10^7 \text{ cm/sec}$$

$$\omega = 3.4 \times 10^6 \text{ radiams/sec}$$

therefore $r_L = 4.4$ cm

We repeat the same steps as above to determine whether the particle passes over the top of the collector, or is actually collected. Referring again to Figure 1C:

$$\theta = \cos^{-1}\left(\frac{4.4 - 1.5}{4.4}\right) = 0.85 \text{ radians}$$

the time required to get across to the collector is

$$t = \frac{\theta}{\omega} = 2.5 \times 10^{-7} \text{ sec}$$

in this time the particle has moved in the $-\hat{z}$ direction in the drifting reference frame by

$$\Delta z = r_L \sin \theta = 3.3 \text{ cm}$$

and in the laboratory reference frame, the gyro-center has moved in the $+\hat{z}$ direction by

$$v_D \times t = 7.15 \text{ cm}$$

so the net motion is 3.85 cm in the $+\hat{z}$ direction, which is slightly higher than the top of the collector plate, so the particle will not be collected. Since this is an extreme case, we can be sure the particles coming off the target with less energy or moving with a small component of velocity directed toward the collector will be collected. Furthermore, the experimental measurements indicate that those particles leaving the target and satisfying the extreme conditions used above are too few to affect the results.

D. Error Analysis

A summary of the possible sources of error in this experiment is presented below:

(1) Incident Particle Energy

The accelerator voltage was periodically calibrated with an electrostatic voltmeter, over the entire range of operation, but the digital voltmeter display of the voltage could only be read to an accuracy of ±2 percent. The energy spread of the ions leaving the source was less the 2 eV and did not contribute measurably to the uncertainty. However, the total incident energy was the sum of the accelerator energy and the target bias. The bias supply was also calibrated with an electrostatic voltmeter and found to be accurate to ±5 percent. Finally, there was the possibility that accelerated ions could be neutralized before striking the target, and thus have a lower incident energy. Any such effect was cancelled out by taking readings of the collected negative ions with the charge component of the beam steered onto the target and with the beam steered into the collimator Faraday cup.

(2) Incident Ion Species

Since all of the ions from the accelerator have the same energy, and since the momentum analyzing magnet is sensitive to the ratio of charge to mass only, a beam of H_2^+ could be contaminated with D^+ and a beam of H_3^+ could be contaminated with HD^+. To minimize cross-contamination, the accelerator was run on Ar gas between switching from H_2 to D_2, then the relative magnitudes of the mass 1 through 6 peaks were compared. The results showed three dominant peaks (1,2, and 3 for H_2 and 2,4, and 6 for D_2) which were two to three orders of magnitude larger than the three remaining peaks.

(3) Uncollected Negative Ions

A discussion of the loss of negative ions due to the collector geometry is given in Chapter IV, and is summarized below:

From Figure 16 and Appendix C, it can be seen that less than 1 percent of the negative ions pass beyond the boundary of the collector plate. The loss of negative ions through the aperture in the collector plate is shown in Figure 17 to be less than 3 percent. Therefore the total uncollected negative ion signal is less than 4 percent.

(4) H^+ leaving the collector

Neutral and negative ions striking the collector can be reflected as positive ions, which are accelerated back to the target. The net effect would be the same as if an extra negative ion reached the collector for every positive ion which left. This effect was investigated by measuring the NISEC from a Na target with a stainless steel collector and with a Na covered collector. Although the work function of the collector was varied from 4 eV (stainless steel) to 2.3 eV (Na),

and the charge distribution of the particles leaving the collector was correspondingly altered, no change in the measured NISEC was observed. Since no change was observed, the effect of H^+ leaving the collector must be less than the uncertainty of the measurement (± 5 percent).

(5) Electronics

The signals from the collector and the collimator-Faraday cup were read by picoammeters, whose output was displayed on digital volt meters. The Picoammeter-DVM units were calibrated with a standard source within one percent, but fluctuations in the beam resulted in an uncertainty of ± 5 percent in the DVM readings.

(6) Work Function Measurements

The change in the target work function was obtained from an I-V curve (see Appendix C), by extrapolating two lines to their intersection. The uncertainty resulting from errors in the estimated slopes of these lines was ± 5 percent.

(7) Impurities

The impurity contribution to the NISEC was less than 5 percent of the signal, as explained in Appendix E.

E. Sputtered Negative Ions in the NISEC

To determine what fraction of the NISEC was due to negative ions sputtered from the target, 8.0 keV Ar^+ ions were used to measure the NISEC[53] from each alkali-metal target. The results of the Ar^+ NISEC measurements, as well as the hydrogen NISEC measurements for each alkali-metal target are summarized in Table 1E.

The Ar^+ NISEC is fairly constant for all of the alkali-metal targets. Since Ar^- is not known to exist,[54] the NISEC must be due to negative ions sputtered from the target. Since Ar^+ sputtering rate is fairly constant from one target to another, we would expect similar results for the hydrogen sputtering rate. However, the NISEC measurements for hydrogen vary by two orders of magnitude from Li to Cs. To estimate the fraction of the hydrogen NISEC which is due to sputtered negative ions, assume that for deuterium on Li, all of the collected negative ions are sputtered and that there are no reflected D^-. The ratio of the D-NISEC to the Ar-NISEC can be used as a scaling factor for the other alkali-metal targets, for example.

$$\text{Sputtered D-NISEC for Na} = \frac{\text{D-NISEC for Li}}{\text{Ar-NISEC for Li}} \times \text{Ar-NISEC for Na}$$

The sputtered negative ion contributions to the NISEC's, as calculated above are also shown in Table 1E. It can be seen that they are less than 10 percent of the total NISEC. Furthermore, if the NISEC for D on Li is compared to that of H on Li, it can be seen that the H-NISEC is about three times larger than the D-NISEC. If it were true, as assumed above, that the NISEC for D on Li were due to sputtered ions only, then it would be larger than the H-NISEC on Li because at the same incident energy, D sputters more efficiently than H.[55,56] Since the reverse is true, at least some of the H-NISEC on Li must be due to reflected negative ions, so some of the D-NISEC must also be due to reflected particles. Thus the procedure used above gives an upper limit of the sputtered ion contribution to the NISEC.

TABLE 1E. NISEC measurements for D and Ar beams bombarding the same targets. These measurements were used to determine an upper bound for the sputtered-impurity-negative-ion contribution to the NISEC.

Target	1 keV D-NISEC	8 keV Ar-NISEC	$\frac{\text{D-NISEC for Li}}{\text{Ar-NISEC -or Li}} \times \text{Ar-NISEC}$	Maximum impurity fraction
Li	0.0012	0.0130	0.0012	1.0
Na	0.019	0.0089	0.00082	0.043
K	0.034	0.0087	0.00080	0.024
Rb	0.055	0.0183	0.00163	0.031
Cs	0.076	0.0217	0.00200	0.026

F. Derivation of the NISEC Fitting Function

We start with Equation (9) of Chapter II:

$$\text{NISEC} = \frac{1}{N_i} \int_{\bar{v}} n(\bar{v})(1-e^{-\alpha/v})\, e^{-\beta/v}\, d\bar{v} \qquad (1F)$$

where

$$\alpha = \int_0^{x_0} P(x)dx$$

$$\beta = \int_{x_0}^{\infty} Q(x)dx$$

For a cosine distribution of backscattered particles, we can write:

$$n(\bar{v}) = n(v)A\cos(\theta)d(\cos(\theta))d\phi$$

where A is a normalization constant given by:

$$\int_0^{2\pi}\int_0^1 A\cos(\theta)d(\cos(\theta))d\phi = 1 = 2\pi A \left.\frac{(\cos\theta)^2}{2}\right|_0^1 = \frac{2\pi A}{2}$$

Also, n(v) is isotropic in ϕ, so that the integral over $d\phi$ gives 2π, which is cancelled by the $\frac{1}{(2\pi)}$ factor resulting from normalization. Equation (1F) becomes:

$$\text{NISEC} = \frac{2}{N_i} \int_v \int_0^1 n(v)\cos(\theta)[1-e^{-\alpha/v\cos(\theta)}]e^{-\beta/v\cos(\theta)}\, d(\cos(\theta))dv$$

If we look only at the integration over θ, and let $\alpha/v = a$ and $\beta/v = b$, we get:

$$I(\theta) = 2\int_0^1 (\cos(\theta)e^{-b/\cos(\theta)} - \cos(\theta)e^{-(a+b)/\cos(\theta)})d(\cos(\theta)) \qquad (3F)$$

Let

$$\frac{1}{\cos(\theta)} = u,$$

then

$$d(\cos(\theta)) = \frac{du}{u^2},$$

so Eq. (3F) gives:

$$I(\theta) = 2\left[\int_1^\infty \frac{e^{-bu}}{u^3}\,du - \int_1^\infty \frac{e^{-(a+b)u}}{u^3}\,du\right]$$

Both integrals are of the same form, with different constants in the exponents. The integrals can be found in the Handbook Mathematical Functions[57] as number 5.1.4 and are given by

$$\int_1^\infty \frac{e^{-bu}}{u^3}\,du = -\left.\frac{e^{-bu}}{2u^2}\right|_1^\infty + \frac{b}{2}\left.\frac{e^{-bu}}{u}\right|_1^\infty - \frac{b^2}{2}\left[\gamma + \ln b + \sum_{n=1}^\infty \frac{(-1)^n b^n}{nn!}\right]$$

where γ = Euler's constant = 0.57722...

$$\int_1^\infty \frac{e^{-bu}}{u^3}\,du = \frac{e^{-b}}{2} - \frac{be^{-b}}{2} - \frac{b^2}{2}\left[\gamma + \ln b + \sum_{n=1}^\infty \frac{(-1)^n b^n}{nn!}\right]$$

Therefore,

$$I(\theta) = 2\,[\frac{e^{-b}}{2}(1-b) - \frac{b^2}{2}[\gamma + \ln + \sum_{n=1}^{\infty}\frac{(-1)^n b^n}{nn!}] - \frac{e^{-(a+b)}}{2}(1-(a+b))$$

$$+ \frac{(a+b)^2}{2}[\gamma + \ln\,(a+b) + \sum_{n=1}^{\infty}\frac{(-1)^n (a+b)^n}{nn!}]]$$

substituting β/v for b and α/v for a, and re-arranging the terms we get

$$I(\theta) = e^{-\beta/v}[1-\beta/v - e^{\alpha/v}(1-\frac{\alpha+\beta}{v})]$$

$$- (\frac{\beta}{v})^2[\gamma + \ln(\beta/v) + \sum_{n=1}^{\infty}\frac{(-1)^n(\beta/v)^n}{nn!}]$$

$$+ (\frac{\alpha+\beta}{v})^2\,[\gamma + \ln\frac{\alpha+\beta}{v}\sum_{n=1}^{\infty}\frac{(-1)^n[(\alpha+\beta)/v]^n}{nn!}]$$

The NISEC is given by

$$\text{NISEC} = \frac{1}{N_i}\int_v I(\theta)\; n(v)dv$$

which is Eq. (2) of Chapter V.

REFERENCES

1 "TRTR Neutral Beam Injector system Conceptual Design," LBL-3296 (August 1975).

2. T. K. Fowler and B. K. Logan, Comments on Plasma Phys. and Cont. Fusion Res., 2 167 (1977).

3. D. R. Sweetman, A. C. Riviere, H. C. Cole, E. Thompson, D. P. Hammond, J. Hugill and G. M. McCracken in Plasma Physics and Controlled Nuclear Fusion Research 1971, (Proc. Conf. Madison, 1971) 3, IAEA, Vienna (1971), pp. 393.

4. K. H. Berkner, R. V. Pyle and J. W. Stearns, Nucl. Fusion, 15, 249 (1975).

5. A. S. Schlachter, K. R. Stalder and J. W. Stearns, Abstracts of the 10th International Conference on the Physics of Electronics and Atomic collisions, 2, (Paris 1977), pp. 870-871.

6. K. W. Ehlers, Nucl. Instrum. Methods, 32, 309 (1965).

7. Yu. I. Belchenko, G. I. Dimov and V. G. Dudnikov, Zh. Tekh. Fiz., 43, 1720-25 (1973) [Sov. Phys. Tech. Phys., 18, 1083 (1974)].

8. Yu. I. Belchenko, G. I. Dimov and V. G. Dudnikov, Zh. Tekh. fiz., 45, 68 (1975) [Sov. Phys. Tech. Phys., 20, 40 (1975)].

9. Yu. I. Belchenko, Ph.D. Thesis, Novosibirsk.

10. G. I. Dimov, G. Ye. Dereviankin and V. G. Dudnikov, IEEE Trans. Nucl. Sci. NS-24, 1545 (1977).

11. K. Prelec, Proc of the First Symposium on the Production and Neutralization of Negative Hydrogen Ions and Beams (Brookhaven, N.Y. 1977), pp. 111-117.

12. J. R. Hiskes, M. Bacal and G. Hamilton, "Atomic Reaction Rates in H^- and D^- Plasmas," Lawrence Livermore Laboratory Report UCID 18031 (1979).

13. M. Bacal, E. Niclopoula and H. J. Doucet, Proc. of the First Symposium on the Production and Neutralization of Negative Hydrogen Ions and Beams (Brookhaven, N.Y. (1977), pp. 26-35.

14. Yu. I. Belchenko, G. I. Dimov and V. G. Dudnikov, Izv. Akad. Nauk. SSSR Ser. Fiz. 37, 2573 (1973).

15. V. G. Dudnikov, Ye. G. Obrazovsky and G. I. Fiksel', Preprint IYAF 77 (1977).

16. W. Eckstein, H. Verbeek and S. Datz, Appl. Phys. Lett., 22, 10 pp. 527-528 (1975).

17. W. Heiland, U. Beitat and E. Taglauer, Phys. Rev. B, 19, 4, pp. 1677-81 (1979).

18. P. Massman, H. J. Hopman and J. Los, XVIth International Conference on Phenomena in Ionized Gases, Grenoble France (1979).

19. M. C. Yu, Proc. of the First Symposium on the Production and Neutralization of Negative Hydrogen Ions and Beams (Brookhaven, N.Y. 1977), pp. 48-52.

20. M. C. Yu, Phys. Rev. Lett., 40, 9, pp. 574-577 (1978).

21. J. R. Hiskes, XIVth International Conference on Phenomena in Ionized Gases, Grenoble, France, 1979.

22. G. I. Dimov, presented at the Second Symposium on Ion Sources and Formation of Ion Beams, Berkeley, Ca., 1974.

23. J. R. Hiskes and A. Karo, Proceedings of the Symposium on the Production and Neutralization of Negative Hydrogen Ions and Beams, Brookhaven, N.Y. (1977), pp. 42-47.

24. J. R. Hiskes, A. Karo and M. Gardner, J. Appl. Phys., 45, 9, pp. 3888 (1976).

25. M. Ye. Kishinevskiy, Zh. Tekh. Fiz., 45, 1281 (1975)[Sov. Phys. Tech. Phys., 20, 799 (1975)].

26. M. Ye. Kishinevskiy, Institute of Nuclear Physics (Novosibirsk) Report IYAF 76-18 (1976).

27. L. M. Kishinevskiy, Izvestiya AN SSSR, 38, 392 (1974).

28. L. M. Kishinevskiy and Ya. A. Vinokurov, Ion Emission--A Method of Studying Surface Properties, Tashkent FAI, 1975, pp. 89-96.

29. R. K. Janev, Surf. Sci., 45, 609 (1974).

30. R. K. Janev, Surf. Sci., 47, 583 (1975).

31. O. S. Oen and M. T. Robinson, Proc. Sec. Conf. on Surface Effects in Controlled Fusion Devices, San Francisco, Ca., 1976, (North Holland Publishing Company, Amsterdam, 1976), pp. 210.

32. Liquid helium cryopump manufactured by Andonian Associates, Inc., Waltham, Massachusetts.

33. Alkali-metal dispensors manufactured by S.A.E.S., Colorado Springs, Colorado.

34. C. Herring and M. H. Nichols, Rev. Mod. Phys., 21, 185 (1949).

35. J. Millman and S. Seely, Electronics (McGraw-Hill, New York, 1955), pp. 107.

36. P. A. Anderson, Phys. Rev., 47, 958 (1935).

37. Quadrupole mass spectrometer, model 100C, manufactured by Uthe Technology, Inc., Sunnyvale, California.

38. P. Meischner and H. Verbeek, Max-Planck-Institute for Plasma Physics (Garching, Germany), Report IPP 9/18, (1975).

39. W. Eckstein, P. Matschake and H. Verbeek, Proc. Sec. Conf. on Surface Effects in Controlled Fusion Devices, San Francisco, Ca. (1976) (North Holland Publishing Company, Amsterdam, 1976).

40. Handbook of Chemistry and Physics 57th ed., R. C. Weast, editor, pp. E 81-82, 1976.

41. J. B. Taylor and I. Langmuir, Physical Review, 44, no. 6, pp. 423-458, (1933).

42. C. A. Papageorgopolous and J. M. Chen, Surf. Sci. 21, pp 377-389, (1970).

43. C. A. Papageorgopolous and J. M. Chen, Surf. Sci. 52, pp. 40-52 (1975).

44. A. H. Sommer, to be published in J. Appl. Phys.

45. L. W. Swanson and R. W. Strayor, J. Chem, Phys., 48, pp. 2421, (1968).

46. C. A. Papageorgopolous and J. M. Chen, Surf. Sci. 39, pp. 283-312, (1973).

47. J. R. Hiskes and P. J. Schneider, Bull. Am. Phys. Soc. 24, pp. 999 (1979).

48. K. N. Leung and K. W. Ehlers, Abstracts of the IEEE International Conference in Plasma Science, (Montreal, 1979), pp. 32.

49. R. E. Thomas, T. Pankey, J. W. Gibson and G. A. Haas, Appl. Surf. Sci. 2, pp. 187 (1979).

50. O. A. Anderson, "Efficient Energetic Neutral Beam Source Using Jet Surface Conversion," Lawrence Livermore Laboratory report UCID-19659 (1977).

51. P. H. Dawson (Editor), Quadrupole Mass Spectrometery and its Applications, Elsevier Scientific Publishing Company, Amsterdam, 1976.

52. H. M. Powell, Ion Trajectory Studies and Experiments for a Quadrupole Mass Spectrometer (University Microfilms, Inc., Ann Arbor Mich. (1966)), Ph.D. Thesis, Vanderbilt University.

53. The 8.0 keV Ar^+ ions were produced with a 4.0 keV beam plus -4 kV bias on the target. Therefore, it is possible for incident ions to be reflected as positive ions and to reach the collector, cancelling out the signal due to some of the sputtered negative ions. Although mass analysis of the positive ions from a Cu target showed the presence of a reflected Ar^+ ions, analysis of the ions from any of the alkali-metal targets showed no Ar^+. Based upon this result, it was assumed that the collector signal due to reflected Ar^+ ions was negligible compared to the sputtered negative ion signal from the clean alkali-metal target.

54. H. Hotop and W. C. Lineberger, Journal of Physical and Chemical Reference Data, 4, 539-576 (1975).

55. E. W. McDaniel, Collision Phenomena in Ionized Gases (J. Wiley and Sons, Inc., 1964), pp 653.

56. C. F. Barnett, J. A. Ray, E. Ricci, M. I. Wilker, E. W. McDaniel, E. W. Thomas and H. B. Gilbody, Atomic Data for Controlled Fusion Research (Oak Ridge National Laboratory, 1977), 2, section D.

57. M. Abramowitz and I. A. Stegun, Handbook of Mathematical Functions, U. S. Government Printing Office, Washington, D. C. 1965, pp. 228-29.